Waste heat recovery and coupling of a hydrogen internal combustion engine and liquid organic hydrogen carrier dehydrogenation reactor

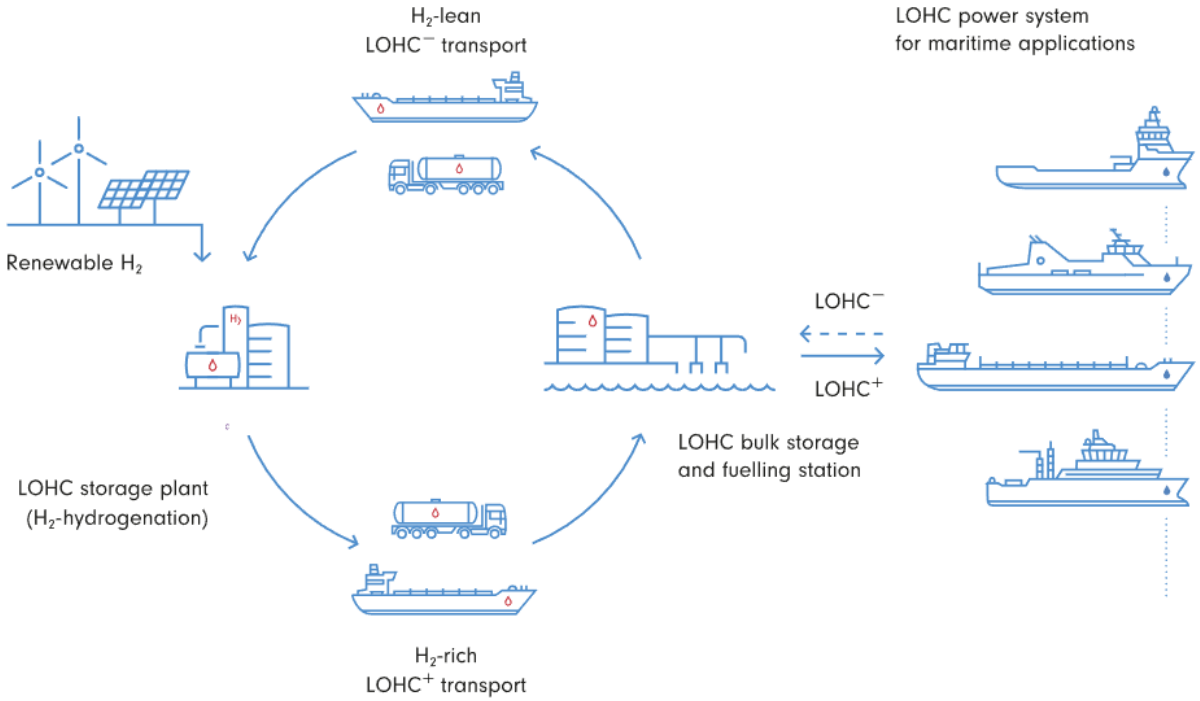

(source: https://hydrogenious-maritime.net/)

Author: Laurence Sliepenbeek

Date: September, 2024

Master Thesis, Marine Engineering, at Technical University Delft

Graduation committee: Dr. Ir, P.de Vos (chair), Pr. Ir. K. Visser,

Ir. E.S. van Rheenen (supervisor) and Ir. J.R.T.. Postma.

A word of gratitude

I would briefly like to state my gratitude to those involved in this project. It has been an interesting journey of scientific exploration and at the same time frustrating one of many hours spent on MATLAB scripts, equations, and texts, but to no avail as I am proud of the result. The patient but passionate guidance or Erin has been of great value, at moments when other factors of life (a family-business and my wonderful kids) would hinder progress our regular contact moments would bring back the focus. I got a nudge when I deserved one and assurance and guidance when i needed it in the process. But most of all I enjoyed the moments we would discuss the theory and direction of the research. It has always been a motivation to support your future studies on energy carriers and I wish you all the best with your academic career.

I also want to extend a special thanks to Ir. K. Visser for staying involved in the research, despite your retirement at the TU Delft.

And finally, to my partner Sophie I want to thank you for taking up the slack when I was in “thesis focus mode” and for your support for me and our family in the years it has take me to finish my masters degree.

Abstract

The study seeks to reduce emissions in the shipping industry by exploring a propulsion system based on hydrogen internal combustion engines (H2ICEs) and liquid organic hydrogen carrier (LOHC) technology. While both technologies are strong contenders for future propulsion systems, their combined use has not yet been extensively researched. However, this combination could be both feasible and advantageous, and similar integrations have been studied for other hydrogen power systems.

A literature review is conducted on the integration of LOHC reactors with proton exchange membrane fuel cells (PEMFCs), solid oxide fuel cells (SOFCs), and H2ICE, specifically focusing on the hydrogen carrier H18-DBT. H18-DBT can store 6–8 wt.% hydrogen and comes close to meeting energy density requirements, although dehydrogenation losses are significant. Decreasing dehydrogenation losses is possible through waste heat recovery (WHR). DBT is favored for its low flammability and toxicity and high commercial availability, but environmental and viscosity issues remain.

The study identifies gaps in the literature by examining hydrogen carrier-based power systems, focusing on heat utilization methods for dehydrogenation, and quantifying the potential of WHR to improve system efficiency and exercise. This is especially relevant for H18-DBT due to its high dehydrogenation enthalpy.

For SOFC systems, the literature review concludes that direct heat transfer from high-temperature exhaust gases significantly enhances system efficiency and energy. Given an optimized design, WHR from SOFCs can fully support the dehydrogenation energy requirement under dynamic loads, which benefits overall system performance. In contrast, for PEMFC systems, WHR poses challenges due to the low-grade heat available, but preheating DBT before reactor entry improves efficiency. However, existing integration studies for PEMFCs may be overly optimistic, as they do not account for energy destruction at higher current densities. Nonetheless, coupling PEMFCs with LOHC reactors remains feasible and beneficial for system efficiency.

The integration of H2ICE with LOHC reactors and WHR appears promising based on the availability of high-temperature exhaust gases, similar to SOFC systems. The literature on port fuel injection (PFI) and direct injection (DI) H2ICE technologies shows potential for efficiency gains through WHR from exhaust gases and coolant.

To assess the efficiency improvements from WHR in H2ICE and their overall feasibility, this study proposes a system design and develops a model that simulates mass and energy balances for all operating points of an H2ICE. This model allows for comparison with other potential propulsion systems. A conceptual system-level model is created using MATLAB to analyze the WHR and coupling potential of H2ICE with LOHC reactors. The model uses two empirical engine models (for DI and PFI, respectively) and two reactor modeling approaches: a basic thermodynamic model and a kinetic model.

The model iterates until the reactor and H2ICE operating points are feasible with respect to the mass balances and determines the optimal reactor setting requiring minimum heat for dehydrogenation. It also calculates the mass flow for a hydrogen burner to estimate the additional hydrogen needed for complete dehydrogenation if WHR is insufficient. Available exergy and heat fluxes are calculated to provide a comprehensive review of the energy balance and WHR effectiveness.

Understanding the mass and energy balance is crucial for assessing the operational capabilities of these systems. The model reveals that while WHR integration in H2ICE is beneficial, it is not sufficient to sustain dehydrogenation at all operating points for H18-DBT.

The results indicate that coupling the dehydrogenation reactor with H2ICE is feasible and yields efficiency gains through WHR from exhaust gases and coolant flow. WHR integration with the thermodynamic reactor model reduces hydrogen combustion in the burner by 40% to 60%, increasing overall efficiency by 18.75%. In a 1D heterogenous model, the results were more promising: above 2,500 RPM, enough heat was available to sustain the dehydrogenation reaction. Nevertheless, concerns remain about the 1D model's analytical derivation equation, as it may underestimate the dehydrogenation heat requirements.

Keywords: Hydrogen internal combustion engine, liquid organic hydrogen carrier, H18-dibenzyl toluene, waste heat recovery, exergy and energy analysis, future propulsion system.

Table of Contents

A word of gratitude 2

Abstract 3

List of Figures 8

Acronyms 10

Abbreviations 12

1 Introduction/Background of the Problem 13

2 Determining a novel research angle 15

2.1 Research questions 15

2.1.1 Sub-questions 15

3 Literature retrieval and Synthesis 17

3.1 Overview 17

3.2 DBT as a marine fuel: Defining the potential 17

3.3 WHR strategies for dehydrogenation 19

3.4 State-of-the-art in coupling with reactors and WHR integrations for PEMFC, SOFC, and H2ICE 20

3.5 Review of system components and system design of the power converters 23

3.5.1 System-level comparison 23

3.5.2 SOFCs 25

3.5.3 PEMFCs 26

3.5.4 H2ICE's 29

3.6 Emissions & Hydrogen internal combustion engine management 34

3.6.1 NOx formation mechanisms 34

3.6.2 Engine management 34

3.6.2.1 Slightly Lean Mixtures 35

3.6.2.2 Advanced Injection Timing: 35

3.6.3 Summary of engine management requirements 36

3.6.4 Hydrogen burner and electric heating 36

3.6.5 Contamination/purification/hydrogen requirements for different power sources 36

3.7 Review of the dehydrogenation reactor's system components and design 37

3.7.1 Determining the energy balance of dehydrogenation 37

3.7.2 Kinetic hydrogen release description 38

3.7.3 Packed bed reactor performance modelling 39
3.7.4 Alternative reactor descriptions from the literature 41
3.7.5 Reactor control 44
3.7.6 Heat exchangers 45
3.7.7 Design restrictions for reactors at sea 47
3.8 Catalyst 47
3.9 Detailed gap analysis 48
3.9.1 Coupling and system-level performance 48
3.9.2 WHR and the system-level performance 48
3.9.3 Comparing system-level performance 49
3.9.4 Overview 50
3.9.5 Filling the gap – defining modelling objectives 51
4 Developed system model 52
4.1 Sizing of components – scaling reactor to fit H2ICE model 53
4.2 H2ICE - Power and fuel flow calculations 53
4.3 Reactor conditions - LOHC mass flow rates and dehydrogenation grade data processing 53
4.4 Heat Flux Calculations and Optimal Scenario Identification 53
4.5 Exergy values calculation and visualization 53
4.6 Heat Requirement Calculation with and without WHR 54
4.7 Simplified thermodynamical approach (Li 2023) 54
4.8 Reiterated Heat Flux and mass flow Calculations 54
4.9 Post processing 54
4.10 Graphical representation of the developed model 55
4.11 Modelling assumptions 55
5 Modelling inputs 56
5.1 Engine characteristics 56
5.2 Heat exchangers 57
5.3 Reactor 57
6 Results 58
6.1 H2ICE: Fuel flow and available heat fluxes 58
6.2 Results from the kinetic model 59
6.3 Coupling 64

6.4 Heat fluxes 65
6.5 WHR: Hydrogen burner mass flows 66
6.6 Efficiencies 68
7 Conclusion 69
8 Suggestions for future research 72
8.1 Combined configurations 72
8.2 More detailed combined reactor HEX and ICE modeling with a control strategy 72
8.3 Comparing engine experiments to models 72
8.4 Completeness of the system design 72
9 Appendices 73
9.1 Block scheme of model 73
9.2 Fuel flows detailed 74
9.3 Results Wang PFI model 75
9.3.1 Reactor conditions 75
9.3.2 Hydrogen burner mass flows 75
9.3.3 H2 and LOHC mass flows 76
9.4 Validation script Preuster 77
9.5 Appendix A 78
9.6 Appendix B - reactors 79
10 Bibliography 80
11 MATLAB Script 85
11.1 Opening statements 85
11.2 Defining reactor, H2ICE and modelling requirements 85
11.3 Loop over the operating points of the H2ICE 86
11.4 H2ICE calculation of mass flows 87
11.5 Peters 2019, 1D heterogenous reactor model 88
11.6 Available exergy at operating point of H2ICE 93
11.7 Heat balances of WHR strategies 94
11.8 Reiteration of mass flows and heat fluxes 96
11.9 Li 2023, simplified thermodynamical reactor model 98
11.10 End loop over H2ICE operating conditions and final results table 100
11.11 Post processing for figures and plots 100

List of Figures

Figure 1 – Graphical representation of the research topic 15

Figure 2 – Gravimetric and volumetric energy density requirements (Van Rheenen et al., 2022) 17

Figure 3 – DBT storage strategy (Hoecke et al., 2021) 19

Figure 4 - PI-control algorithm setup (Geiling et al., 2021) 21

Figure 5 – Comparison of the different configurations evaluated in Müller et al.(2019) 23

Figure 6 – Definition of efficiency and exergy in Li et al. (2023) 24

Figure 7 – Exergy flow diagram of the DBT-based SOFC chain with WHR strategies (Li et al, 2023).... 24

Figure 8 – SOFC heat as a function of fuel utilization and electrical efficiency (Peters et al., 2019).... 25

Figure 9 – SOFC system layout, an optimized design for WHR (Peters et al., 2019)..... 26

Figure 10 – Power and conventional exergy information of different components in the system under real conditions (Li et al., 2021) 27

Figure 11 – Variation of the fuel cell engine system performance in efficiency and power output with current density at various operating temperatures (Mert et al., 2012) 28

Figure 12 – Heat balance of a PFI H2ICE (Wang et al., 2019) 30

Figure 13- Exhaust gas temperatures [K] (Wang et al, 2019)..... 31

Figure 14 – Variation of total exergy as a function of speed and load (Wang et al., 2019)..... 31

Figure 15 – Variation of total exergy as a function of speed and load (Zhang et al., 2023) 32

Figure 16 - DI H2ICE exhaust gas temperatures (Zhang et al., 2023)..... 33

Figure 17 – Variation of total available exergy as a function of speed and load (Zhang et al., 2023) .. 33

Figure 18 – Summary of engine management requirements (Stępień Z, 2024) 36

Figure 19 – Overview of simplified DBT cycle (Preuster et al., 2016) 37

Figure 20 – Detailed energy balance of DBT dehydrogenation unit (Preuster et al., 2018) 37

Figure 21 – Heat fluxes in the dehydrogenation unit (Preuster et al., 2018)..... 38

Figure 22 – Kinetic hydrogen formation relation (Peters et al., 2019) 38

Figure 23 – Experimental data vs. model-based description during H18-DBT dehydrogenation in the temperature range between 260 °C and 310 °C; the vertical axis represents the dimensionless concentration (Peters et al., 2019)..... 39

Figure 24 – Mass flow relation for PBR as a function of LHSV and temperature (Preuster et al., 2018) 39

Figure 25 – Power output and dehydrogenation grade as a function of temp and LHSV for DBT and 99% conversion; results are specific to the system design (Peters et al., 2019) 41

Figure 26 – Change in reactor mass flow in tube bundle reactor as a function of temperature, pressure, and feed flow (Geiling et al., 2021) 44

Figure 27 – Design of reactor heater from SOFC exhaust gases and model validation (Preuster et al., 2018) 45
Figure 28 – Overview of heat exchanger types (Kadar, J. 2024) 46
Figure 29 – Decision block model H2ICE 52
Figure 30 - H2ICE coupled with dehydrogenation reactor system design 55
Figure 31. Fuel flows as a function of BMEP and RPM 58
Figure 32. Exhaust exergy, DFI, and PFI for H2ICEs 58
Figure 33. Heat fluxes as a function of the RPM and the required reactor temperature 59
Figure 34. Mass flows analytical solution 1D heterogeneous model by Peters et al. (2019) 59
Figure 36. Experimental results compared to the model of Peters (Peters, 2019) 60
Figure 37. LOHC mass flow as a function of RPM and power 62
Figure 38. H2 mass flow as a function of RPM and power 63
Figure 39. Reactor conditions in the DFI model 64
Figure 40. Heat fluxes required for dehydrogenation for both reactor models 65
Figure 41. Hydrogen burner mass flows for Li (2023) and Peters (2019) reactor models 66
Figure 42. Comparison of the efficiency of propulsion systems (left image includes H2ICE). The image on the right is from (Kadar J. et al., 2024) 68

Acronyms

BTE	Brake Thermal Efficiency
CFD	Computational Fluid Dynamics
CHP	Combined heat and power systems
CSTR	Continuously Stirred Tank Reactor
DBT	Dibenzyl toluene
DFI	Direct Fuell Injection
DI	Direct Injection
FC	Fuel Cell
GH2	Gaseous hydrogen
GHG	Greenhouse Gasses
GrH2	Green Hydrogen
H0-DBT	Dibenzyl toluene
H18-DBT	perhydro dibenzyl toluene
H2ICE	Hydrogen Combustion engine
HHV	Higher Heating Value
HHVH2	Higher heating value of hydrogen, 142351 J/g
HT	High Temperature
ICE	Internal combustion engine
IEA	International Energy Agency
IMO	International Maritime Organization
IRENA	International Renewable Energy Agency
Ktpa	Kilo tons per annum
LH2	Liquid Hydrogen
LHSV	Liquid Hourly Space Velocity, a method for relating the reactant liquid flow rate to the reactor volume at a standard temperature.
LHV	Lower Heating Value
LOHC	Liquid Organic Hydrogen Carrier
MBEP	Mean brake effective pressure
NH3	Ammonia
ORC	Organic Rankine Cycle

PEMFC	Proton Exchange Membrane Fuel Cell
PFI	Port fuel injection
PFI	Port Fuel Injection
PFR	Plug Flow Reactor

Abbreviations

T	Temperature in Kelvin
h	Enthalpy
n	Molar flow s^{-1}
LHSV	Liquid Hourly Space Velocity h^{-1}
Q	Heat flux J s^{-1}
r_i	Rate of hydrogen formation mol m^{-3} s^{-1}
R	Gas constant 8.314 J mol^{-1} K^{-1}
E_A	Activation energy 119.8 kJ mol^{-1}
k_0	Preexponential factor 125.24 s^{-1}
τ	Residence time s
c/c_0	Dimensionless concentration
Cp	Heat capacity
ð	Stoichiometric ratio of H2 to LOHC
M	Molar mass (kg/mol)
dm/dt	Mass flow rate (kg/s)

1 Introduction/Background of the Problem

Developing zero-emissions hydrogen-based ship propulsion systems is challenging but essential to avert the climate crisis, which will have devastating consequences if we do not slow global emissions. According to the United Nations, consequences of the climate crisis will include major threats to international peace, food and water insecurity, more frequent disasters linked to climate and weather extremes, rising sea levels, which will threaten 40% of the world population and the destruction of two-thirds of cities and ecosystems (Hoesung Lee, 2023).

International shipping is responsible for more than 80% of global trade and, despite technical advancements, remains a contributor to greenhouse gases (GHG; Shakeri et al., 2020). Shipping produces approximately 600 metric tons of CO_2, equivalent to 2% of overall CO_2 emissions annually (International Energy Agency [IEA], 2022). For perspective, if it were a country, the shipping industry would be the sixth-highest emitter of CO_2 globally (Hoecke et al., 2021). The shipping industry is not on track to reach the specified International Maritime Organization's (IMO) commitment of a 50% reduction in total annual GHG emissions and a 70% reduction in CO_2 emissions compared to 2008. Indeed, the emissions of GHGs from ships could rise by as much as 250% by 2050 compared to 2012 levels due to growth in global freight volumes. Binding international legal agreements to control GHGs are not yet in place, as technical solutions continue to be costly and industry backing is insufficient (Wan et al., 2018; Wang & Wright, 2021).

Research and development are crucial in pursuing efforts to decrease GHG emissions and keep global warming below 2 °C. The goals outlined in the IMO's initial strategy cannot be achieved with fossil fuels (International Maritime Organization [IMO], 2019). While various technical and operational energy efficiency measures on ships can help reduce GHG emissions, adopting and implementing alternative energy solutions, such as hydrogen carriers, is necessary for the shipping industry to meet its emission reduction targets (Bach et al., 2020), especially since the lifetime of vessels is long. For instance, vessels built now will still be operational in 2050.

According to the International Energy Agency (IEA), heavy industry, heavy-duty road transport, and shipping offer the greatest opportunities to deliver fossil fuel and emissions savings (IEA, 2022). Hydrogen has been recognized as one of the most promising future alternative energy sources for transportation decarbonization. When using hydrogen as fuel, the only by-products are water and a minimal amount of hydrocarbons and NO_x, depending on the energy converter. Green hydrogen can be produced from various renewable sources, including biomass, nuclear power, and non-bio renewable energy, such as wind and solar photovoltaics. However, numerous challenges must be overcome to realize a hydrogen-based energy infrastructure, including technical aspects, incomplete regulations and specifications, economic aspects, and high costs and investments (Wang & Wright, 2021).

The most significant constraint for designing ships with hydrogen as a maritime fuel is probably not production or endpoint use but the storage method (Hoecke et al., 2021; Wang & Wright, 2021; Zhu & Xu, 2015). Hydrogen has a high gravimetric energy density but a low volumetric energy density compared to traditional maritime fuels. At standard atmospheric conditions, hydrogen is a very low-density gas.

Another issue with hydrogen is its extremely flammable scent and colourless gas. Dibenzyl toluene (H18-DBT) is among the storage options that solve the flammability and density issue. H18-DBT is the focus of this study because it seems to be an attractive alternative fuel for the shipping sector as it is available with a high technology readiness level (TRL), is safe, is easy to handle, and can meet energy density requirements with the right system design. The endpoint users for powering ships are advancing, with maritime TRLs for low-temperature proton exchange membrane (PEM) systems at 6–7, high-temperature proton exchange fuel cells (PEMFC) systems at 5–6, and solid oxide fuel cell

(SOFC) systems at 4–5 (Mestemaker et al., 2019). For liquid hydrogen (LH2), several types of internal combustion engines (e.g., dual fuel, spark-ignited, and compression-ignited) have reached a TRL of 9. However, uncertainty exists in how these endpoint users can be integrated into a working propulsion system with the hydrogen storage options available, as many of these options require a processing step to obtain the hydrogen. These systems and their capabilities can determine the characteristics of the propulsion systems.

The constraints in hydrogen storage methods are defined by the storage medium's specifications and the entire system's requirements. Dehydrogenation requires heat and an endothermic catalytic reaction within a reactor to extract H2 from H18-DBT. A significant drawback of LOHC systems is the need to supply heat at the necessary temperature level to meet energy demand, as this approach reduces system efficiency. However, smart system integrations, such as implementing WHR, can enhance efficiency. While some system integrations have been explored, the energy efficiency of DBT as an energy storage solution for maritime propulsion systems warrants more detailed study for

2 Determining a novel research angle

Previous studies on LOHC have primarily concentrated on the chemical, physical, and material aspects of LOHC hydrogenation and dehydrogenation, the calculation of thermochemical and thermophysical properties, and the advancement of new LOHC pairs (Carvalho, 2018; Li et al., 2023; Wang & Wright, 2021). In contrast, the research angle of this study is a system-level review of the integration of the dehydrogenation reactor, a power converter, a balance of plant (BOP), and WHR for maritime propulsions. A graphical representation of the research topic shown in Figure 1 – Graphical representation of the research topic. The results of this study should allow comparison between the system's efficiency and exergy for PEMFC, SOFC, and hydrogen internal combustion engines (H2ICE) power converters.

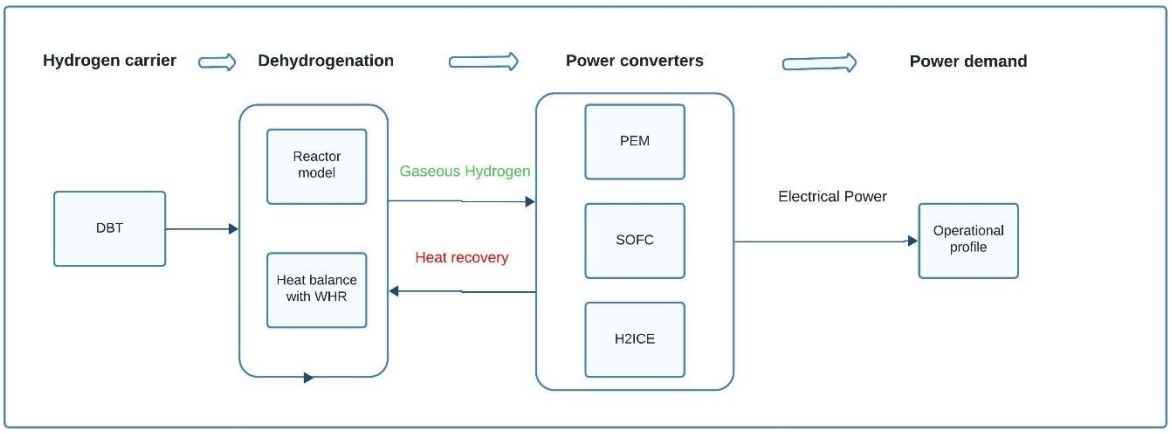

Figure 1 – Graphical representation of the research topic

2.1 Research questions

The obtain insight in the energy distribution characteristics of the system, the research question and sub questions were formulated.

What are the system-level efficiency and exergy of PEMFC-, SOFC-, and H2ICE-propulsion systems with coupled dehydrogenation of H18-DBT and waste heat integration for different propulsion load factors?

2.1.1 Sub-questions

1. **What propulsion systems are suitable for coupling with H18-DBT dehydrogenation, and how can system components be modelled?**

   The goal was to understand the system properties, requirements, and suitability for combining the power converters with the reactor for LOHC dehydrogenation.

2. **What research gaps should be addressed using H18-DBT as a marine fuel in proposed propulsion systems?**

   The goal was to find the literature gap to determine this study's system-level comparison. The literature on the entire system was analysed, from the properties of H18-DBT to its suitability as a marine fuel to the system components (e.g., the reactor, power converter, and BOP).

3. **Is there sufficient quality heat from the power converter at fixed power to support dehydrogenation?**

Can the dehydrogenation be performed with the heat supplied by the power converter of the propulsion systems at multiple load factors?

4. **What is the effect of varying the propulsion power demand of the propulsion system on the capability to support dehydrogenation, considering the mass and energy balance?**

   Ships must perform many tasks, from steaming to manoeuvring/limited station-keeping. These tasks have varying power demands, and the effect of varying propulsion power on the mass and energy balances can give insight into operational profiles.

5. **What are the energy and exergy efficiencies of the propulsion systems with WHR?**

   Understanding the efficiencies and exergy is crucial to determine if these systems can compete with alternative technologies available.

3 Literature retrieval and Synthesis

3.1 Overview

This chapter offers a comprehensive review of the scientifically relevant, state-of-the-art literature to address the research questions and support the development of the system model in the subsequent phase of this master's thesis. The following methodology was defined to find the gap in literature:

- A study on DBT as a marine fuel.
- Quantifying the available and extractable heat with the general properties of various power converters (PEMFC, SOC, and H2ICE) and suitable WHR strategies, determining heat fluxes, mass, energy balance, and exergy at different operating points.
- Finding an appropriate modelling method for the dehydrogenation reactor to describe the energy (heat) requirement of the dehydrogenation reaction consisting of the chemical reaction and the reactor design.
- Determining limiting factors on operational conditions for the reactor, providing insights into mass flows, heat fluxes, and influential reactor parameters.

3.2 DBT as a marine fuel: Defining the potential

This section explicates the arguments in favour of and against adopting DBT as a marine fuel, discussing the properties of this hydrogen carrier. DBT can generally store 6–8 weight percentage (wt.%) hydrogen at ambient temperature and pressure for extended periods (Kwak et al., 2021). This property is among the factors determining a hydrogen carrier's suitability for maritime fuel applications. The U.S. Department of Energy has set a minimum required density, as shown in the red lines in Figure 2, requiring at least 7.5 wt.% of hydrogen per kg of the carrier and 2.3 kWh/L (Van Rheenen et al., 2022).

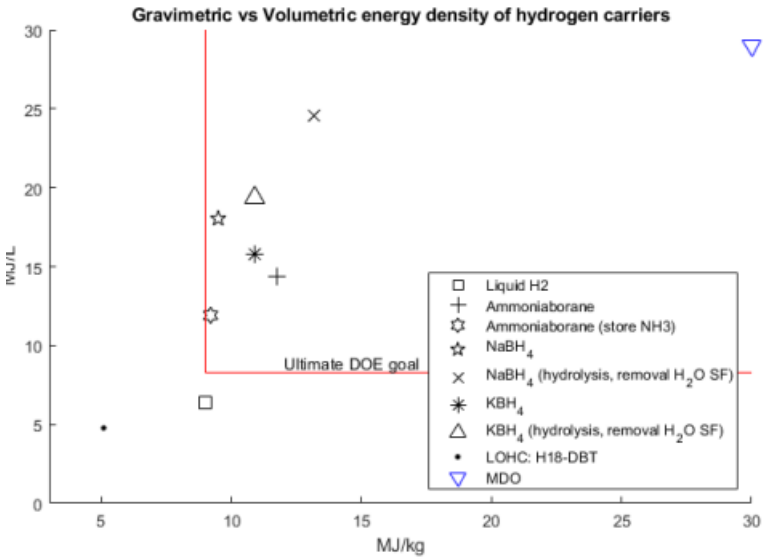

Figure 2 – Gravimetric and volumetric energy density requirements (Van Rheenen et al., 2022)

Nevertheless, these theoretical values represent a narrow approach when selecting hydrogen carriers for maritime purposes. A comparative study by Van Rheenen et al. (2022) on non-CO_2-emitting hydrogen carriers used effective instead of theoretical densities. These effective densities included packing, the spent fuel weight, dehydrogenation energy losses, and other influencing factors. When considering these, DBT should be included as a candidate for future maritime fuels (Van Rheenen et al., 2022). Dehydrogenation losses are approximately 28% to 35% of the lower heating value (LHV) of stored hydrogen (Hoecke et al., 2021; Lee et al., 2021; Niermann, Beckendorff,

et al., 2019; Niermann et al., 2021; Van Rheenen et al., 2022). Minimizing or eliminating these losses with WHR increases storage densit. Some studies have gone as far as stating that WHR is indispensable for DBT as integrating this technology in the dehydrogenation cycle raises storage density, system efficiency, and exergy to levels that allow it to compete with other hydrogen carriers such as LH2 and green hydrogen (GH2; Hoecke et al., 2021; Li et al., 2023; Niermann, Drünert, et al., 2019).

An analysis of the energy and exergy efficiencies of 24 LOHC chains of DBT proved to be the most favourable LOHC for implementing WHR strategies (Li et al., 2023). This result was primarily due to its low preheating heat demand (8.9% of the stored hydrogen energy) and high dehydrogenation rate, as emphasized by Peters et al. (2019). The high dehydrogenation rate was convenient for maritime applications as the gas flow indicated the time interval between system start-up and hydrogen delivery, a factor in determining the dynamic behaviour of mobile systems.

The positive selection criteria for DBT are a high TRL (9), low flammability, low toxicity, ease of handling, and excellent commercial availability. DBT is a liquid at room temperature, with a boiling point for H0-DBT at 390 °C. The flash point is 200 °C, albeit with high viscosity in loaded form (Bollmann, Mitländer, et al., 2023). Kinematic viscosities above 100 mm^2s^{-1}, as found for H18-DBT at temperatures below 34° C, can cause problems with pumping. A possible solution to this problem is using the H0-BT/H12-BT instead of the H0-DBT/H18-DBT cycle with lower viscosity. This H0-BT/H12-BT cycle also reported that a higher level of dehydrogenation could be reached at an identical temperature and absolute pressure and was thus more productive (Rüde et al., 2022). To date, most studies have focused on the H0-DBT-H18DBT cycle for dehydrogenation. Therefore, the focus of this study remained on this cycle to safeguard the comparative value. Another option would be implementing the BOP for the H18-DBT similarly to HFO systems currently on ships with a comparable kinematic viscosity of approximately 105 mm^2s^{-1} at 40 C°.

Environmental hazards characterize DBT handling. DBT is a category-4 chemical, representing the relatively lowest danger for chronic aquatic toxicity. Nonetheless, according to the safety data sheets, this classification still causes long-lasting harmful effects on aquatic life. Storage at ambient temperatures and pressure for extended periods means that DBT can use the existing fossil fuel infrastructure. Dehydrogenation and hydrogenation are robust, and if the maximum temperature (340 °C) is not exceeded (Kwak et al., 2021), the carrier has a long lifetime.

DBT has no drawbacks concerning packing. It is like diesel and does not require additional space. However, when using DBT as fuel on ships, an extra buffer tank is necessary because the loaded and unloaded forms of LOHC cannot be stored together. This buffer tank would remain empty during the voyage and be filled with unloaded LOHC to prevent mixing with charged DBT, as shown in Figure 3 (Hoecke et al., 2021).

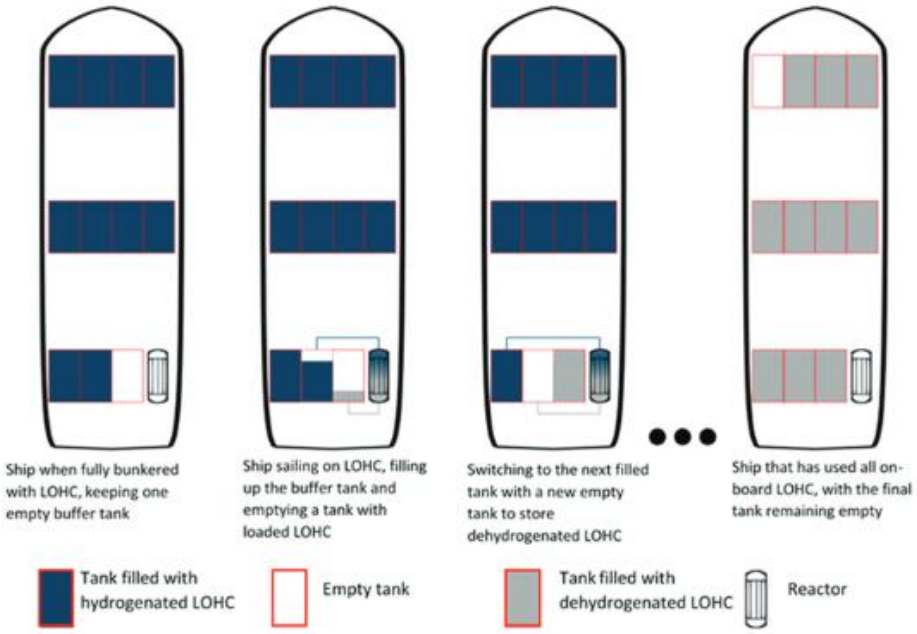

Figure 3 – DBT storage strategy (Hoecke et al., 2021)

3.3 WHR strategies for dehydrogenation

This section delves into diverse WHR methods, elucidating their suitability for different power sources and their implications for modelling. The literature introduces a range of these strategies, systematically depicted in Figure 4. The formulas for the heat fluxes are derived in a later chapter of the study when the reactor is examined in more detail.

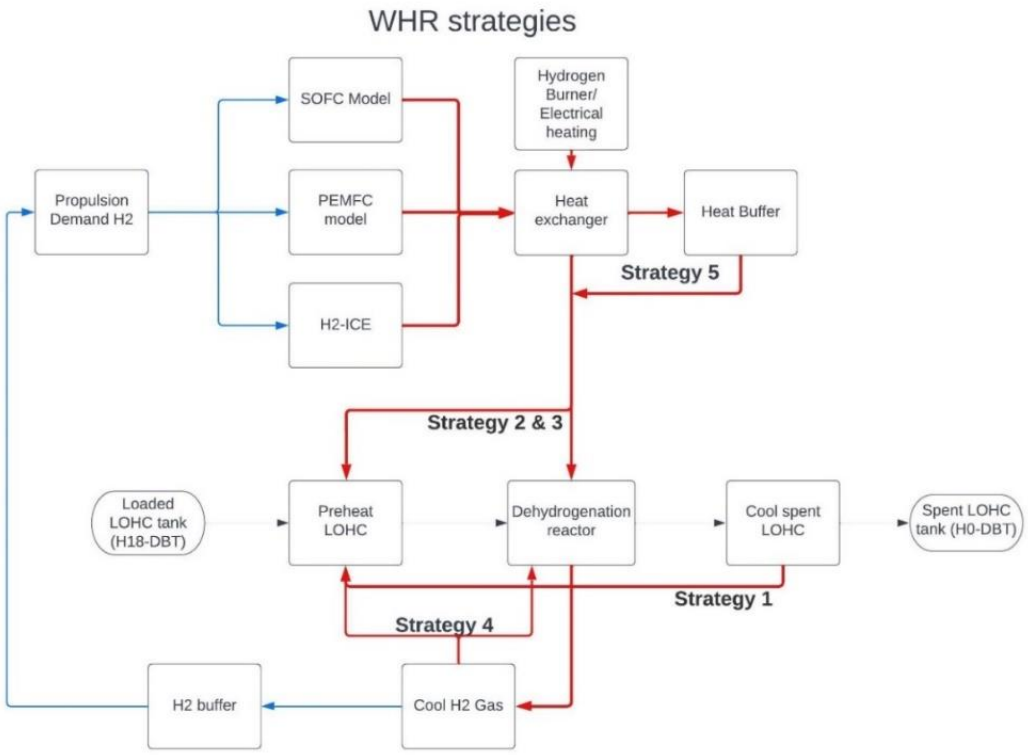

Figure 4 – Overview of WHR strategies

Description of WHR strategies

1. Using the unloaded LOHC (H0-DBT) exiting the dehydrogenation reactor to preheat the entering loaded LOHC (Asif et al., 2021; Geiling et al., 2021; Li et al., 2023);
2. Recovering the heat generated by the hydrogen consumer to provide the dehydrogenation heat (Ye et al., 2022);
3. Recovering the heat generated by the hydrogen consumer to preheat the loaded LOHC entering the dehydrogenation unit (Li et al., 2023; Peters et al., 2019);
4. Gaseous H2 from the reactor was at reactor temperature and could be cooled down before entering the power converter. The idea is that PEMFCs and ICE require H2 at lower temperatures than the reactor temperatures, and this heat can be recycled (Baroutaji et al., 2021; He et al., 2016; Kandlikar & Lu, 2009);
5. Investigating the benefits of employing a heat buffer if the supply and demand of heat might not be synchronous.

3.4 State-of-the-art in coupling with reactors and WHR integrations for PEMFC, SOFC, and H2ICE

This section describes the state of the art in dehydrogenating DBT, coupling, and integrating WHR strategies.

Li et al. (2023) conducted a literature study assessing the WHR potential of liquid organic hydrogen carrier chains. The performed modelling of these storage chains gave a state-of-the-art overview demonstrating the efficiency gains of several WHR strategies (using several heat sources). Li et al. found that the modelled efficiencies of DBT-based hydrogen storage chains were higher than those of conventional GH2 and LH2 for SOFC. The combination of and PEMFC of all 24 LOHC chains studied, benefited most from WHR. The study provided insight into the energy and exergy of the energy storage chains by defining the mass and energy balances and solving them using engineering equation-solver software. The mathematical descriptions of components mass and energy balances can describe system components for their application in maritime propulsion systems.

Li et al. (2023) concluded that a comprehensive heat integration between the SOFC and PEMFC and the dehydrogenation unit for a combined hydrogenation and dehydrogenation cycle. The SOFC combination resulted in the highest exergy efficiency, due to the high temperature of SOFC exhaust gases. The PEMFC and DBT combination with WHR resulting efficiencies for DBT combined with WHR were an energy efficiency of 68.6% and an exergy efficiency of 61.1% for SOFC, with an energy efficiency of 70.4% and an exergy efficiency of 43.7% for PEMFC. An important but perhaps unrealistic assumption in this study was that all heat generated by PEMFC and SOFC was recovered since the temperature used for the calculations was the operating temperature, which is especially optimistic for mobile applications assuming different system load factors (a more detailed analysis is provided in the section on power converters).

For PEMFC, high-temperature waste heat was unavailable, while external electric heaters satisfied the heat demand by the preheater and the dehydrogenation unit. With these assumptions, the energy efficiency increase due to WHR for PEMFC was approximately 38 percentage points. WHR for the SOFC was performed with direct heat transfer, and the exergy increase was approximately 27 percentage points.

This study demonstrated the benefit of WHR but only regarding steady-state non-mobile applications. Dynamic behaviour was reviewed to understand the capabilities of these systems. The state-of-the-art SOFC was described by Preuster et al. (2018), who offered comprehensive insight into integrating an SOFC as a power converter with the dehydrogenation of DBT, showcasing the

system's combined operational efficiency. Emphasis was placed on maximizing the heat integration potential, detailing the quantities of extractable exhaust gas heat, required heat demand, and fuel utilization in their optimized design to ensure sufficient heat availability for all fuel utilization scenarios. Preuster et al. developed an optimized system design that used exhaust heat from the catalyst bed to preheat the incoming air before it entered the SOFC stack, improving system efficiency and fully support dehydrogenation with WHR.

Peters et al. (2019) further investigated this coupled and optimized SOFC system for dynamic operational characteristics. They developed and validated a new kinetic model for dynamic behaviour. Peters et al. found a stable performance and full system coupling, even with a 50% load change, while preventing critical conditions that could impact the reactor and stack. In the SOFC case, it was possible to have full coupling, with the transient behaviour of the reactor and the SOCF being complementary. PEMFCs differ from SOFCs because they have flexible operation, excellent transient performance, load-following capabilities, and a brief warm-up time (van Biert et al., 2016a). These properties make it interesting to see if reactors can react quickly enough to supply the demanded mass flow for the PEMFC.

Lee et al. (2020) delved into the feasibility of connected operations between a dehydrogenation reactor and a PEMFC without WHR. They conducted tests with PEMFCs in a constant current mode, varying reactor temperatures between 240 °C to 300 °C to assess the impact of the dehydrogenation temperature on the PEMFC stack performance but did not cover transient behaviour and varying loads. Lee et al. found that despite carbon purification, which is a must in coupling with PEMFC, methane broke through the filtration and lowered the power output. However, the damage was not irreversible.

Geiling et al. (2021) investigated the operation of a PEMFC under dynamic load changes when coupled to a dehydrogenation reactor combined with a control strategy and a buffer volume. They developed a robust and easily manageable PI-control algorithm, as shown in Figure 4. This control system allowed for load-following of the reactor while halving the buffer size. The reactor temperature and pressure induced faster changes in hydrogen release compared to alterations in LOHC feed mass flow, and the pressure was the easiest to control with a regulator valve at the end of the reactor. Thermal regulation was more difficult due to thermal lag, which is further elaborated on in the section on reactor control.

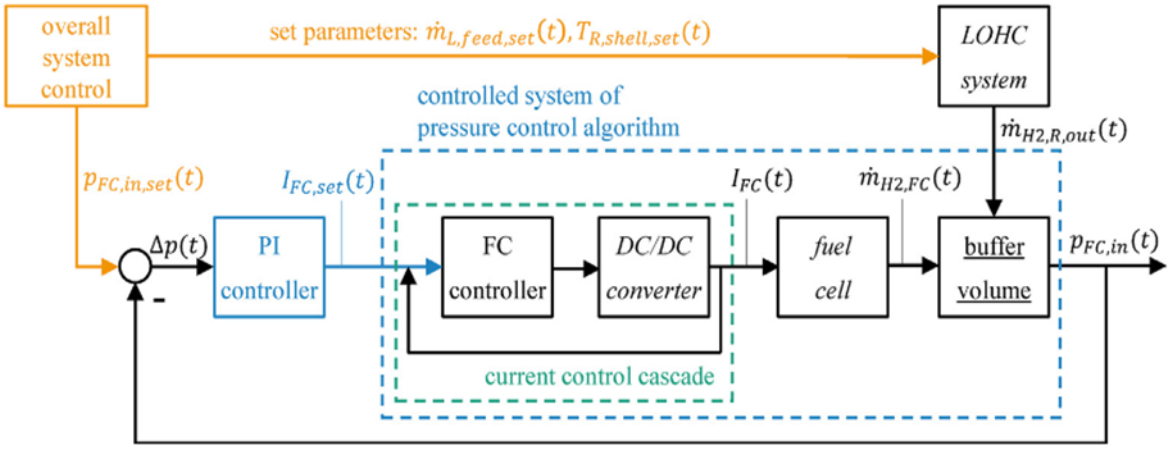

Figure 4 - PI-control algorithm setup (Geiling et al., 2021)

Despite not quantifying WHR's contribution, Geiling et al.'s (2021) design included a heat exchanger utilizing WHR from the reactor to preheat the H18-DBT and recommended installing a condenser between the reactor and buffer storage tank for scale-up purposes to remove evaporated H0-DBT, a common heat strategy described in this study.

Bollmann, Mitländer, et al. (2023) presented a novel approach to harnessing exhaust gas enthalpy from a porous media burner to directly provide the heat required for a kilowatt-scale dehydrogenation process of H18-DBT. The setup successfully demonstrated the dynamic behaviour of the dehydrogenation unit. This system was designed for applications with fluctuating hydrogen demand, such as hydrogen refuelling stations. Methane, sourced from biogas plants, was used as a fuel for the burner. The dehydrogenation process started within 30 minutes of system initiation, and the dehydrogenation unit exhibited a power density relative to its reactor volume of approximately 0.5 kW thermal per litre. Indeed, a similar system burning hydrogen could be an interesting addition to the literature.

On the reactor side, several studies have focused on optimizing reactor conditions. For example, Asif et al. (2021) identified the optimum operating conditions as 320 °C and two-bar pressure, with 2 wt.% pts./Al2O3 as the suitable catalyst. The configuration was subjected to exergy analysis, including the percentage of exergy efficiency and the exergy destruction rate. The optimization strategies were developed based on principles of process integration and WHR. WHR used heat to preheat the feed and minimize consumption. Rao et al. (2022) optimized for cost with a 1D model ensuring reactor conditions for a 99% conversion at different feed temperatures, wall temperatures, and hydrogen burner efficiencies to study the energy required by the dehydrogenation reactor. Heat exchanger areas were calculated for cost calculation purposes.

No DI and PFI H2ICE combinations with coupled dehydrogenation have been found in the literature, a clear GAP. Overall, PFI and DI H2ICE systems have shown significant potential for increased efficiency through optimizing energy and exergy recovery with WHR (Wang et al., 2019; Zhang et al., 2023). As exhaust temperatures are above reactor operating temperatures, direct heat exchange is expected to be possible. However, due to the lower delta T compared to the SOFC case, further research and study are necessary to determine the coupling performance.

The efficiency of exhaust and coolant exergy in H2ICE systems can be optimized by maintaining lower exhaust pressure and using the ORC system for exhaust recovery while enhancing coolant recovery, which involves reducing heat-transfer losses and increasing coolant temperature. The available exergy in H2ICE is between 10% and 30% depending on the engine type and operating point (Wang et al., 2019; Wu et al., 2018), but the exergy, including the DBT dehydrogenation, is unknown. Coupling for H2ICE has not been studied, but the purity requirements for H2ICE are notably lower than for dehydrogenation-supplied hydrogen (Gurbuz, 2020). While reduced purity influences emissions, a detailed analysis of this aspect is given in paragraph 3.6.2.3.

3.5 Review of system components and system design of the power converters

This section investigates the characteristics and available heat of the heat sources proposed in this study to determine the quantity of available heat and its dependency on component load. The system designs to extract the heat are studied, facilitating integration in system modelling. The efficiency of fuel cell systems is highly dependent on the performance of their auxiliaries and their design, according to Xing et al. (2021). For a system-level comparison, knowing how much heat is available is imperative and not all waste heat is equally useful.

Distinguishing between possible dehydrogenation processes requires investigating possible heat supply methods. The comparative efficiency of these systems is shown in Figure 5. The worst case is only electric heating to provide the LOHC dehydrogenation heat, while the most favourable is full heat integration between a high-temperature fuel cell and the dehydrogenation unit. Partial combustion of hydrogen for heat provision is an attractive choice (Müller et al., 2019).

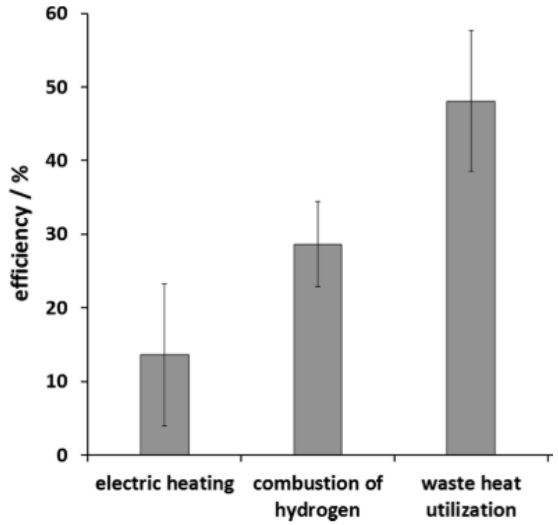

Figure 5 – Comparison of the different configurations evaluated in Müller et al.(2019)

3.5.1 System-level comparison

Li et al. (2023) described the dehydrogenation process mathematically, as discussed below.

Electricity generated by fuel cells was described as:

$$PFC = massflow\ H2\ out * HHVH2 * \eta FC.$$

The waste heat generated by the fuel cell system was calculated as:

$$QFC = massflow\ H2\ out * HHVH2 * \eta FCh,$$

where ηFC was the ratio of fuel cell electricity output to the total higher heating value of the supplied hydrogen, and ηFCh was the ratio of fuel cell heat output to the total higher heating value of the supplied hydrogen. The temperature of the heat equalled the fuel cell operating temperature.

Energy and exergy efficiencies are shown in Figure 6. The heat fluxes described were for preheating step Q_4 and the heat flux to drive the endothermic reaction Q_{de}. Notably, this study's heat fluxes from hydrogenation were 0, which only considered the dehydrogenation cycle.

Chain	Exergy efficiency	Energy efficiency
S_{EL}-C_{SOFC}	$\frac{Ex_{SOFC,r} + Ex_{hy,r} + P_{SOFC}}{Ex_{H2,in}}$	$\frac{Q_{SOFC,r} + Q_{hy,r} + P_{SOFC}}{En_{H2,in}}$
S_{EL}-C_{PEMFC}	$\frac{Ex_{PEMFC,h} + P_{PEMFC} + Ex_{hy,r}}{Ex_{H2,in} + Q_{de} + Q_4}$	$\frac{Q_{PEMFC} + P_{PEMFC} + Q_{hy,r}}{En_{H2,in} + Q_{de} + Q_4}$

Notes:

$$Ex_{SOFC,r} = Q_{SOFC,r}\left(1 - \frac{T_0}{T_{SOFC}}\right), Ex_{hy,r} = Q_{hy,r}(1 - \frac{T_0}{T_{H2,h}}), En_{H2,in} = m_{H2,in}HHV_{H2},$$

$$En_{H2,out} = m_{H2,de}HHV_{H2}, Ex_{q,de} = Q_{de}(1 - \frac{T_0}{T_{de}}), Ex_{Q4} = Q_4(1 - \frac{T_0}{T_{de}}).$$

Figure 6 – Definition of efficiency and exergy in Li et al. (2023)

The mass flow rate of hydrogen exiting the dehydrogenation unit is shown below. The stichometry rate was assumed to be 70%, with mechanical efficiency at 99.99% (Li et al., 2023):

$$\dot{m}_{H2,out} = \frac{\dot{m}_{L+}}{M_{L+}} \bullet M_{H2} \bullet \partial \bullet \eta_{de}$$

The heat required by the dehydrogenation reactor was:

$$Q_{de} = \frac{\dot{m}_{H2,out}}{M_{H2}} \bullet q_{de}$$

These calculations resulted in exergy flow diagrams, as depicted in Figure 7, which overview the exergy losses in the system for the SOFC.

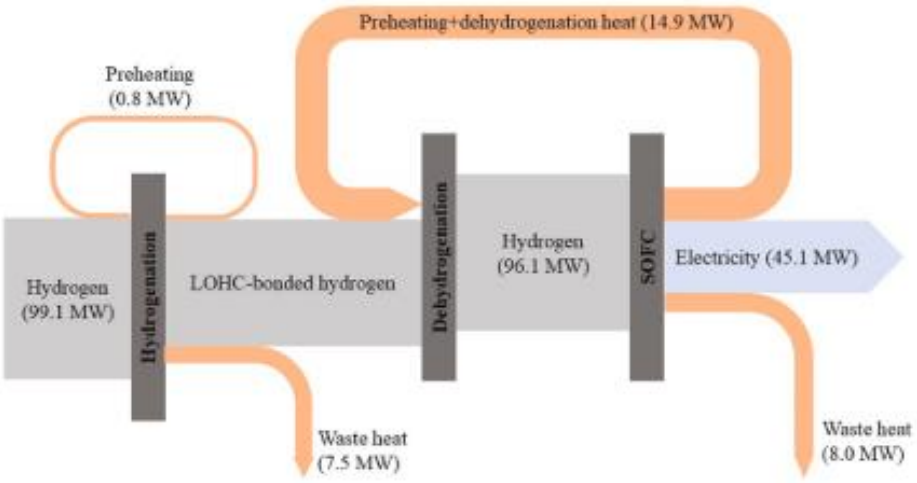

Figure 7 – Exergy flow diagram of the DBT-based SOFC chain with WHR strategies (Li et al, 2023)

3.5.2 SOFCs

SOFCs are a versatile (regarding fuel choice) energy conversion technology that uses ceramic membranes to enable the diffusion of oxide ions at high temperatures (500–1,000 °C). These temperatures allow for the use of non-noble catalysts, such as nickel, and increased tolerance to fuel impurities (Preuster et al., 2018). When coupled with heat cycles, net electrical efficiencies may surpass 70% without WHR; 50–65% electrical efficiencies derived from LHV can be expected (Mestemaker et al., 2019). Despite their advantages, SOFCs often require many auxiliary components, insulation materials, and thermal management systems, resulting in lower power densities and slower response times than low-temperature PEMFC systems. SOFCs are designed for stationary applications (e.g., ships) and offer relatively long lifetimes, with current products ranging from 20,000 to 40,000 hours. Future generations are expected to reach up to 90,000 hours. Although current manufacturing costs are high, large-scale production can significantly reduce these costs, making SOFCs a more attractive option for marine applications (Haseltalab et al., 2021; van Biert et al., 2016a, 2016b, 2021).

3.5.2.1 Quantifying available heat from SOFCs

Depending on the cell type, SOFCs have an operating temperature range between 700 °C and 1,000 °C. Nonetheless, the operating temperature does not significantly impact the exhaust gas temperature leaving the system, as a large portion of the energy in the gas is required to preheat the incoming air to the necessary stack inlet temperature. Depending on the system configuration, exhaust gas temperatures can range from 300 °C to 900 °C. The exhaust gas quality at the stack outlet of the SOFC system varies depending on the operating point (Peters et al., 2019), which is primarily influenced by the amount of air and the degree of fuel utilization. If the fuel cell operation is rich, more heat is generated in the exhaust gas. Conversely, running lean has produced cooler exhaust gas (Preuster et al., 2018). This extractable heat as a function of fuel utilization is illustrated in Figure 8, which is useful in determining available heat for dehydrogenation.

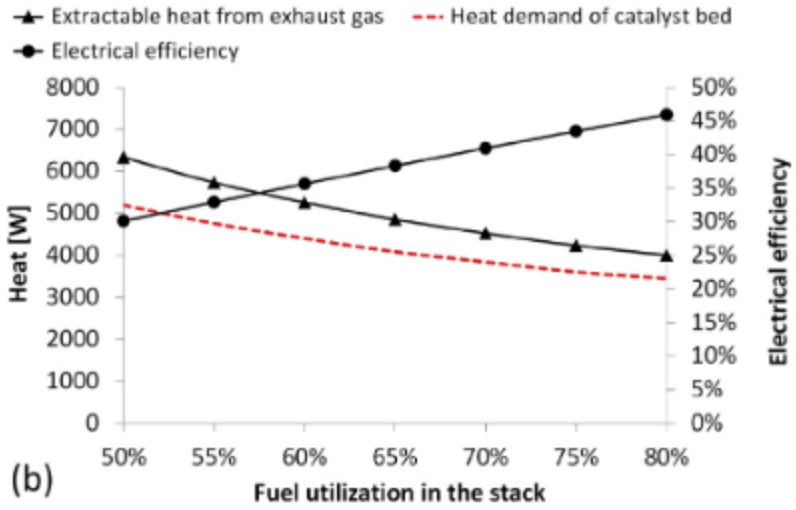

Figure 8 – SOFC heat as a function of fuel utilization and electrical efficiency (Peters et al., 2019)

Peters et al. (2019) provided a system design for dehydrogenation with an SOFC as a power source, as illustrated in Figure 9 below. In the case of heat integration between the SOFC unit and the LOHC dehydrogenation unit, the heat generated in the SOFC unit's catalytic burner is crucial for driving the endothermic dehydrogenation reaction at the appropriate temperature level. After leaving the dehydrogenation unit, the residual heat in the exhaust gas is utilized to preheat the incoming air in a

secondary air heater before it enters the primary air heater. This process allows for recirculating and reusing a portion of the exhaust gas to preheat for the stack. To regulate the exhaust gas temperature at 550 °C, an additional air controller supplies extra air to the catalytic burner's inlet. Minor adjustments to the system configuration enable highly flexible operation while maintaining a reasonably high system efficiency of 45%, defined as the ratio of the SOFC's electrical output to the LHV of the hydrogen bound within the LOHC (Preuster et al., 2018).

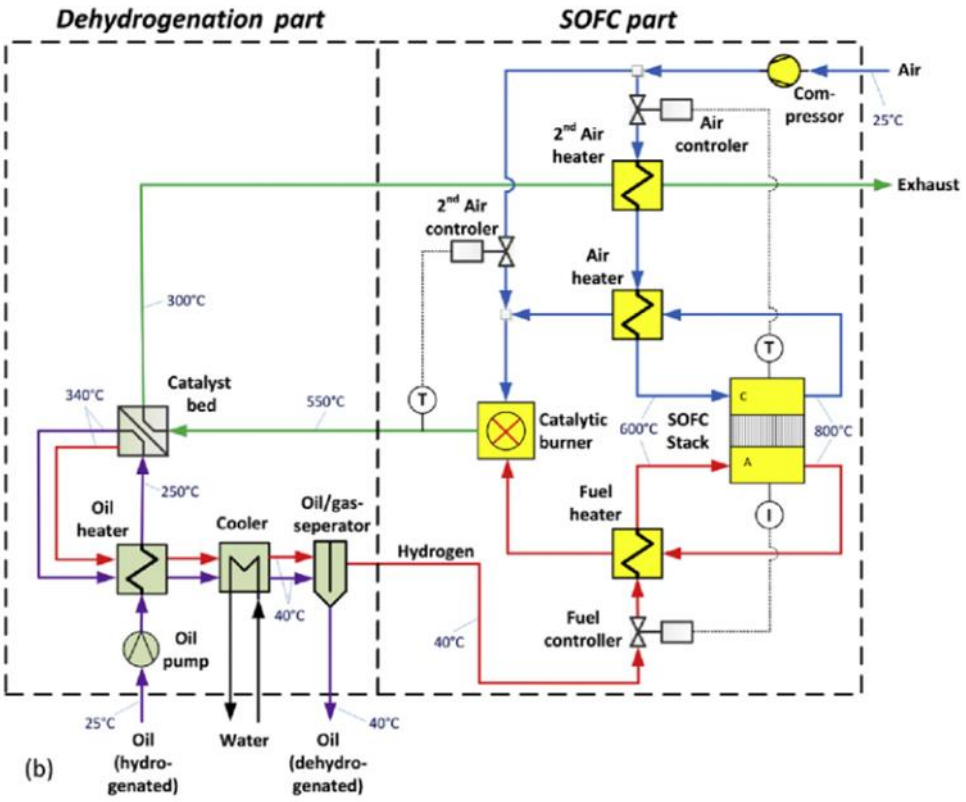

Figure 9 – SOFC system layout, an optimized design for WHR (Peters et al., 2019)

3.5.3 PEMFCs

LT-PEMFCs have solid polymer-acid membranes, such as electrolyte and carbon electrodes, with a platinum-based catalyst and are widely used in various heavy-duty applications. LT-PEMFCs operate at temperatures below 100 °C, and the redox reaction within PEMFCs transforms the energy stored in hydrogen into electricity, heat, and water using an oxidizing agent (van Biert et al., 2021). The advantages of LT-PEMFCs include less stringent material requirements, flexible operations, good transient performance, load-following capabilities, short warm-up times, and longer operational lifetimes. The disadvantages of LT-PEMFCs include the need for noble metal catalysts, platinum catalyst sensitivity to fuel impurities, water management complexity, and slow chemical reaction rates. HT-PEMFCs operate at elevated temperatures and have advantages such as higher performance, lower diffusion losses, and increased tolerance to impurities. However, HT-PEMFCs have higher system complexity, limited commercial success due to shorter lifetimes, and a cost level approximately three times that of LT-PEMFCs running on pure hydrogen. Performance refers to the fact that HT-PEMFCs can achieve higher-power outputs than LT-PEMFCs due to increased reaction kinetics and lower diffusion losses because HT-PEMFCs operate at elevated temperatures, which allows for improved catalyst utilization (van Biert et al., 2016a, 2016b, 2021).

3.5.3.1 Quantifying available heat from PEMFCs

From a WHR perspective, the by-products of operating PEMFCs are water and low-quality heat, deemed unfeasible for heat recovery (Niermann, Beckendorff, et al., 2019). However, this view could be overly pessimistic. Recovering low-grade waste heat poses challenges, including the need for large heat exchangers to optimize heat transfer due to low heat-transfer rates (Baroutaji et al., 2021). Furthermore, the low temperature (60–80 °C) of the coolant water in PEMFCs hinders direct heat transfer to a dehydrogenation reactor, which requires temperatures above 230 °C for endothermic reactions in DBT dehydrogenation. Nonetheless, other WHR strategies, such as preheating (strategy 3), could potentially utilize this lower-quality heat.

For PEMCs, approximately half the energy generated from the electrochemical reaction is dissipated as heat (Soupremanien et al., 2012). Ramousse et al. (2009) explained that most studies have simplified internal heat exchange models, resulting in the global heat source being well-identified but relatively poorly apportioned. Kandlikar and Lu (2009) and Soupremanien et al. (2012) found that heat generation in PEMFCs can be attributed to entropic heat, irreversible reaction heat, and Ohmic heating, which account for approximately 55%, 35%, and 10% of the total heat release, respectively. Nevertheless, uncertainty remains about the contribution of the processes in the PEMFC, while there is consensus on the amount of available heat.

3.5.3.2 Exergy and efficiency of PEMFC

The results of conventional exergy analysis indicate that PEMFC stacks dominate in power, fuel exergy, product exergy, and exergy destruction, exhibiting the highest values among all components. The impact of current density on these conventional exergy analysis results was examined, revealing that the order of components contributing to the total exergy destruction remained consistent regardless of variations in system output power (Li et al., 2021). Figure 10 illustrates the exergy destruction and efficiency for various system components.

Li et al. (2021) conducted a comprehensive review of exergy destruction for the system across multiple current densities, summarized in Table 6 of their research. By summing the exergy destruction of individual components and comparing the relationship between total exergy destruction and current density, a linear relation was found for the system within the current density range of 0.6 to 1. Specifically, at a current density of 0.6, the exergy destruction was 60% of that at a current density of 1 when considering all system components combined. The largest exergy destruction was in the PEMFC cell, which was further studied.

Components	Power (W)	E_F (W)	E_P (W)	E_d (W)	ε_k	ε_d
PEMFC stack	*19879*	*35632*	*19879*	*15753*	*0.56*	*0.44*
AH	*0*	*299.4*	*100.5*	*198.9*	*0.34*	*0.66*
CH	*0*	*1417*	*519.1*	*898.1*	*0.37*	*0.63*
AHE	*61.17*	*76.04*	*13.43*	*62.61*	*0.18*	*0.82*
CHE	*289.7*	*326.6*	*7.067*	*319.5*	*0.02*	*0.98*
AC	*627*	*627*	*417.1*	*209.9*	*0.66*	*0.34*
HC	*7.315*	*7.315*	*4.028*	*3.287*	*0.55*	*0.45*
R	*0*	*1649*	*1554*	*95.2*	*0.94*	*0.06*
WP	*526.2*	*526.2*	*220.2*	*306*	*0.42*	*0.58*

Figure 10 – Power and conventional exergy information of different components in the system under real conditions (Li et al., 2021)

Mert et al. (2012) reviewed a performance analysis of a PEM fuel cell engine system used for transportation applications and a comprehensive parametric study to investigate how the system performance was affected by the system and operating parameters. Figure 11 shows the system's

energy and exergy efficiency as a function of operating temperature. For higher current density, the operating temperature greatly affects the efficiency and exergy of the PEMFC.

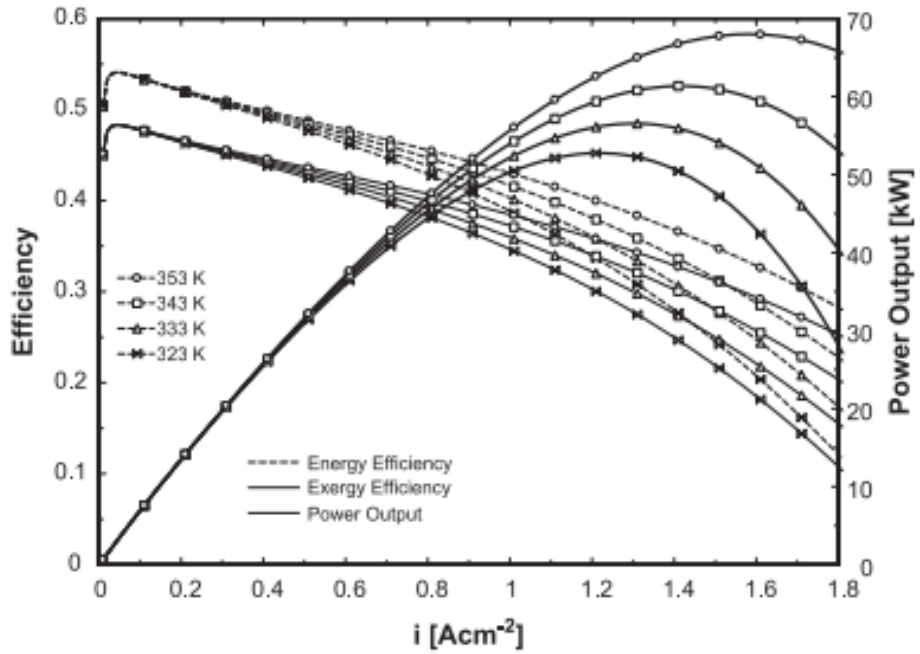

Figure 11 – Variation of the fuel cell engine system performance in efficiency and power output with current density at various operating temperatures (Mert et al., 2012)

Both studies used experiments to validate the models and provided good insights into the available energy and exergy at different operating points, allowing the heat fluxes to be determined. They showed that the current density combined with the operating temperature mattered for the exergy and efficiencies. The fixed values (Li et al., 2023) is a less accurate description of the system under variable load.

3.5.4 H2ICE's

H2ICEs represent a transitional technology that leverages the existing internal combustion engine infrastructure while offering significant environmental benefits. Unlike conventional engines that rely on fossil fuels, H2ICEs use hydrogen as a fuel, producing water vapor as the primary emission. This makes H2ICEs a promising solution for reducing greenhouse gas. H2ICEs are particularly attractive because they can be quickly adapted from existing engine designs, utilizing well-understood technology while significantly reducing carbon dioxide (CO2) emissions. This makes them an appealing option for industries seeking to decarbonize without abandoning the internal combustion engine framework that has been refined over more than a century. The reliability of H2ICEs is significantly bolstered by the extensive history and technological maturity of internal combustion engines. Many components and systems used in H2ICEs are adapted from existing engines, ensuring robustness and durability. Furthermore, the infrastructure for internal combustion engines, including manufacturing and service networks, is already in place, which supports the rapid deployment and scalability of H2ICEs. The ongoing advancements in hydrogen-specific engine components, such as optimized combustion chambers and fuel injection systems, continue to enhance the performance and reliability of H2ICEs, making them a dependable choice for industries aiming to transition towards more sustainable energy solutions. (A Onorati, et al. (2022), Yew Heng Teoh et al. (2023))

(Verhelst et Al. 2009) suggests that while current modeling techniques offer valuable insights, they also have limitations that may reduce their predictive accuracy, particularly in hydrogen's unique combustion characteristics. Thermodynamic models are useful for estimating power, efficiency, and emissions, but often too simplified to capture the complexity of hydrogen combustion under various conditions. CFD Models are highly accurate and detailed in simulating fluid dynamics and combustion but computationally expensive and dependent on detailed input data. Heat transfer models struggle to accurately predict heat losses in hydrogen engines due to hydrogen's higher flame speed and thermal conductivity.

To eliminate most of the modeling uncertainties two studies (Zhang et Al. 2023, Wang et Al, 2019) describing H2ICE properties by experiment with a mapping characteristics experiment were used in this research. Mapping characteristics research is a systematic study of engine performance and emissions over a range of operating conditions. The goal of such an experiment is to create a "map" that represents how various engine parameters (such as fuel consumption, power output, torque, and emissions) change across different load and speed conditions.

3.5.4.1 Dehydrogenation from HICE

When comparing available heat in H2ICE technologies, exergy destruction serves as a crucial parameter indicating the irreversibility of combustion in hydrogen engines. In this case, it indicates less extractable heat for dehydrogenation. This study compared the results from two different engine technologies studies to determine the heat available in these systems. In this study, linear scaling effects were considered, and the energy and exergy losses found for smaller engines were extrapolated to draw conclusions for application in higher-power applications used in ships.

(Nieminen et Al., 2009) utilize a combustion chamber model to determine the exergy balance and conclude that hydrogen-fueled internal combustion engines (ICEs) are more efficient than gasoline engines, converting 41.37% of intake charge exergy into useful work compared to 35.74% for gasoline. Hydrogen's higher compressibility and more efficient combustion contribute to this, though it generates less power due to lower cycle pressures. Hydrogen engines have higher thermal availability (27.3% vs. 19.3% for gasoline) because hydrogen combustion produces more heat, but much of this energy is lost to the cooling system, reducing overall work output. While hydrogen

combustion is less irreversible (11.72% vs. 29.09% for gasoline), these gains are partially offset by other inefficiencies. Overall, hydrogen engines offer greater efficiency but lower power output.

Hydrogen combustion results in higher combustion chamber temperatures compared to traditional hydrocarbon fuels. This is due to hydrogen's faster flame speeds and higher adiabatic flame temperatures, leading to increased heat flux in the combustion chamber. The high temperatures can exacerbate issues like pre-ignition and knocking, requiring advanced cooling techniques to manage thermal loads in engine components like exhaust valves. Specifically, hydrogen's autoignition temperatures range between 773 K and 858 K, depending on the experimental setup. This will limit the maximum temperature in the cylinder and exhaust and the expected delta T for dehydrogenation (Verhelst et Al. 2009).

3.5.4.2 HICE with PFI – results from a mapping characteristics experiment

This paper has analysed the energy and exergy distribution of a 2.3 L turbocharged hydrogen engine by mapping characteristics experiment. The research shows that HICE has achieved a BTE of 45%, expected to reach 51% through combustion chamber optimization and other measures (Wang et al., 2019). This potential increase in BTE suggests that HICE may outperform fuel cell technology. Currently, a significant amount of fuel energy is wasted in the exhaust gas and cooling system, leaving only a fraction utilized in the form of output work. Figure 12 shows the heat balance of the engine. The energy and exergy loss during fuel energy conversion was determined for the 2.3 L turbocharged hydrogen engine by Wang et al. (2019).

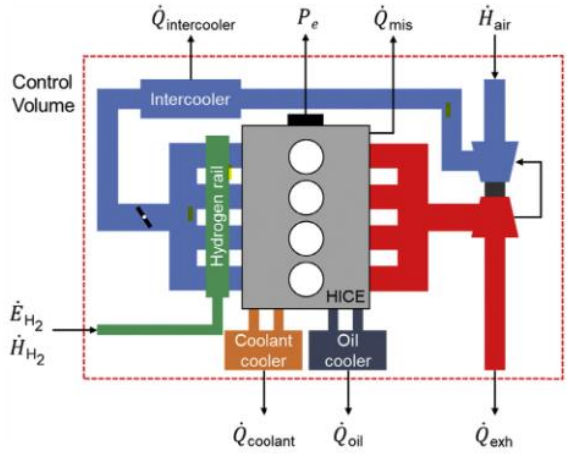

Figure 12 – Heat balance of a PFI H2ICE (Wang et al., 2019)

Energy losses

1. Exhaust energy: Accounts for 23.5% to 34.7% of the energy loss during fuel energy conversion
2. Cooling medium (coolant and oil) energy: Contributes to 21.3% to 34.8% of the energy loss
3. Intercooler energy: Represents 0.5% to 3.6% of the energy loss
4. Uncounted energy: Contributes to 5.8% to 14.1% of the energy loss
5. Effective work: Ranges from 25.7% to 35.1% of the fuel energy

Exhaust gas temperatures

Exhaust temperatures and its dependencies is necessary heat flux determination for the PFI H2ICE are shown in Figure 13

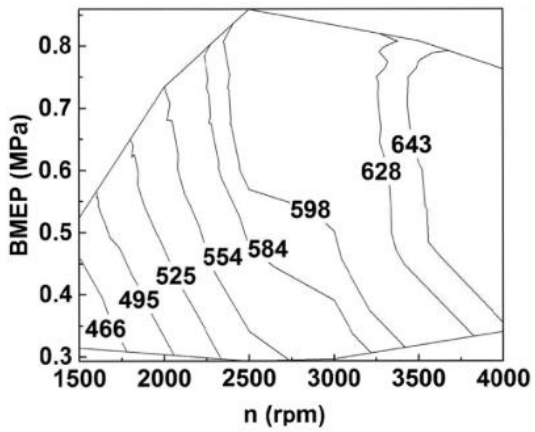

Figure 13- Exhaust gas temperatures [K] (Wang et al, 2019)

Exergy losses

1. Exergy efficiency of coolant energy: does not exceed 5%.
2. Exergy efficiency of exhaust energy reaches up to 23%.

Total exergy efficiency in percentages as a function of brake mean effective pressure (BMEP) and rotations per minute (rpm) is shown in Figure 14. We can determine the power by knowing the rpm, the BMEP, and the displacement.

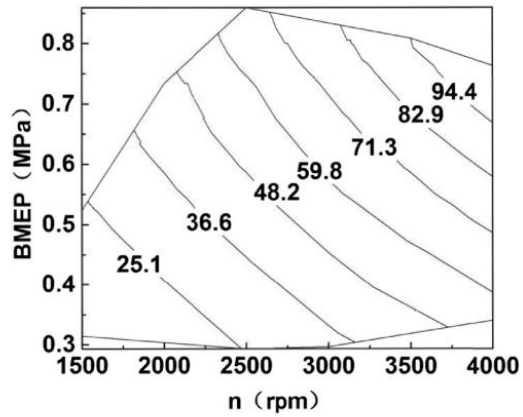

Fig. 25 – Total exergy changes with the engine speeds and loads (kW).

Figure 14 – Variation of total exergy as a function of speed and load (Wang et al., 2019)

Other findings

1. All energy losses increase with engine speeds but are not sensitive to the loads.
2. The turbocharger improves the brake thermal efficiency by up to 4.8%.
3. The total hydrogen fuel thermal efficiency limit is theoretically above 59%.

This description of a PFI-HICE gives a straightforward quantification of the WHR possibilities, which is valuable for determining if sufficient energy is available for dehydrogenation.

3.5.4.3 H2ICE with DI - results from a mapping characteristics experiment

A 2.0L 4-cylinder DI, turbocharged HICE was used in this study. Based on the study performed by (Zhang et al., 2023). In the Zhang study the HICE system was a modified gasoline engine, as the direct injectors of hydrogen were displaced on the centre of each cylinder head. To study the energy and exergy analysis, the DI hydrogen engine map characteristics experiments are conducted.

The DI engine offers favourable break thermal efficiency and reduced dependence on hydrogen purity, albeit at a higher production cost in contrast to the PFI H2ICE, which experiences power loss due to hydrogen's low density occupying 30% of the cylinder volume. The DI HICE overcomes this issue by injecting hydrogen into the cylinder after the intake valves close, thereby enhancing power density. The power density of DI H2ICEs is twice that of PFI H2ICEs. For example, at maximum BTE conditions, the DI H2ICE achieves a BMEP of 1.41 MPa with a power density of 35.1 kW/L, whereas the PFI H2ICE only reaches a BMEP of 0.73 MPa with a power density of 17.3 kW/L. Energy distribution characteristics also differ between DI and PFI systems due to the DI system's higher injection pressure (above 10 MPa; Zhang et al., 2023).

The DI HICE converts a portion of fuel exergy into effective power, but the remaining exergy is lost or destroyed through various processes. Zhang et al. (2023) investigated the available energy through waste heat, specifically exhaust and coolant exergy. Exergy distribution analysis was conducted for various engine speeds and loads. The total available exergy was quantified and is shown in Figure 15:

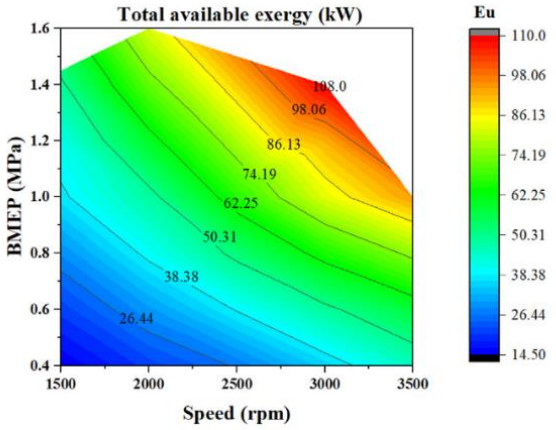

Figure 15 – Variation of total exergy as a function of speed and load (Zhang et al., 2023)

Figure 15 quantifies the total available exergy. However, the study also provides a detailed analysis of the two exergy losses, examining the possibility of converting them back to useful work and quantifying the quantity of exergy in the two main heat losses.

Exhaust exergy

Lower exhaust pressure and a closed turbine bypass valve at low load improve the exhaust exergy efficiency. This study utilized an ORC to recover available energy in the exhaust, enhancing the exhaust exergy efficiency. The maximum efficiency of the ORC system was approximately 10% with steady-state operation, while the average efficiency was 5%. Fully recovering exhaust energy could improve the efficiency of DI-HICE when it operates on the external characteristic curve. (Zhang et al., 2023). Exhaust temperatures and its dependencies is necessary heat flux determination for the DFI H2ICE are shown in Figure 16.

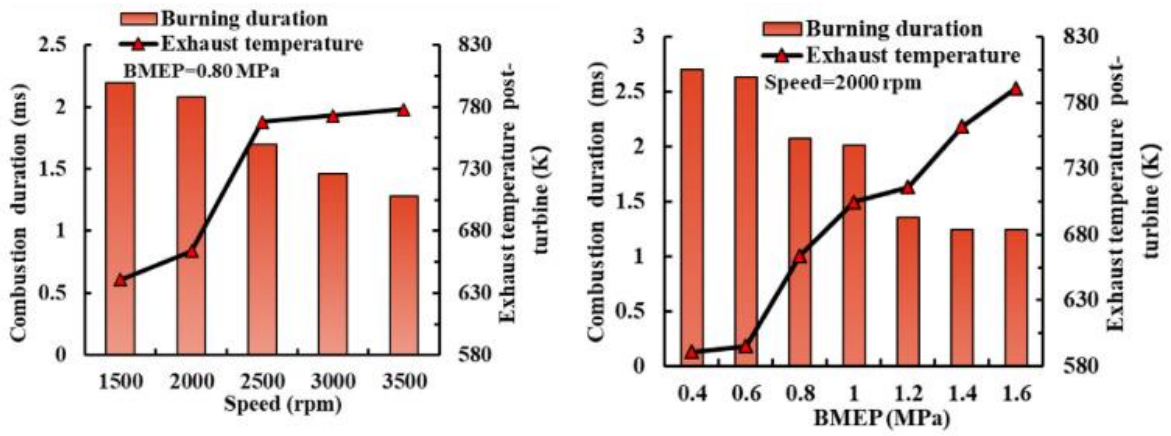

Figure 16 - DI H2ICE exhaust gas temperatures (Zhang et al., 2023)

Coolant exergy

The coolant exergy efficiency varied with engine speed and load. The maximum coolant exergy efficiency was 3.47% at 3,500 rpm (BMEP = 0.4 MPa). The coolant exergy efficiency was highest at each engine speed with a BMEP of 0.4 MPa, as the coolant energy proportion was high at a low load operation. The coolant exergy contained energy less than 5 kW, and the ORC system could recycle a maximum efficiency of less than 3% from the coolant. The average efficiency of the ORC system for coolant energy was only approximately 1%.

Recovering low-quality energy from the coolant was challenging, but reducing heat transferred losses during coolant circulation. Improving coolant exergy efficiency could enhance engine efficiency while increasing coolant temperature could moderately improve the BTE. Using thermal insulation methods could reduce heat loss during coolant circulation and enhance coolant exergy efficiency (Zhang et al., 2023).

Figure 17 below details the exergy distribution at different powers and rpms.

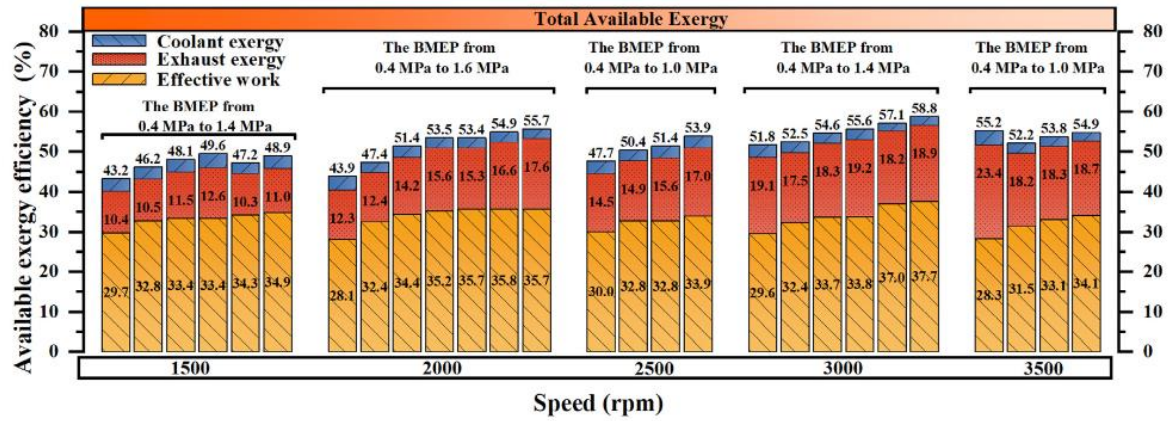

Figure 17 – Variation of total available exergy as a function of speed and load (Zhang et al., 2023)

3.6 Emissions & Hydrogen internal combustion engine management

H2ICEs have potential to drastically reduce CO2 emissions. Since hydrogen contains no carbon, its combustion produces no direct CO2 emissions. However, trace amounts of CO2 can still be generated from the combustion of lubricating oil that enters the combustion chamber during engine operation. Unlike fossil fuels, hydrogen combustion does not produce sulphur oxides (SOx) or particulate matter like soot, which are major pollutants in conventional internal combustion engines. However, nitrogen oxides (NOx), which are formed due to the high combustion temperatures in the engine, remain a concern. Current research focuses on optimizing the combustion process and developing advanced aftertreatment systems to minimize NOx emissions, making H2ICEs a near-zero-emission technology.

3.6.1 NOx formation mechanisms

NOx emissions are a significant concern in hydrogen combustion due to the high temperatures that facilitate the reaction between nitrogen and oxygen in the air. The formation of NOx, particularly thermal NOx, is closely tied to the combustion temperature and is governed by the Zeldovich mechanism, which is highly sensitive to these high temperatures. The formation of thermal NOx is highly temperature-dependent, increasing exponentially with higher temperatures. But also depends on the oxygen concentration and the residence time of the gases at these high temperatures. Residence time refers to the duration that the fuel-air mixture remains at high temperatures in the combustion chamber, which is critical for NOx formation. In two-stroke engines, the power cycle completes in one crankshaft revolution, resulting in shorter residence times and generally lower NOx emissions, despite higher RPMs. However, high RPMs can reduce the efficiency of exhaust scavenging, potentially increasing NOx under heavy loads.

In four-stroke engines, which complete a power cycle in two crankshaft revolutions, residence times are longer, increasing the potential for NOx formation due to prolonged exposure of nitrogen and oxygen to high temperatures. These engines usually operate at lower RPMs, which further extends residence time and can lead to higher NOx emissions unless mitigated by strategies like exhaust gas recirculation (EGR) or precise combustion timing adjustments. Thus, understanding and controlling residence time is crucial for managing NOx emissions in both engine types

While other pathways like prompt NOx, N2O, and NNH play a role, they are less significant compared to thermal NOx.

Prompt NOx: This pathway occurs in the initial stages of combustion, particularly in fuel-rich regions where there is an abundance of hydrocarbon fragments (like CH radicals). These radicals react quickly with nitrogen (N2) in the air to form nitrogen-containing species, which then react with oxygen to form NO. Prompt NOx is typically more significant in fuel-rich, low-temperature environments but generally contributes less to overall NOx emissions compared to thermal NOx.

N2O Intermediate NOx: In certain combustion conditions, especially at lower temperatures, nitrogen dioxide (NO2) can form through intermediate reactions involving nitrous oxide (N2O). This pathway is less common in typical engine conditions but can become relevant in engines using specific fuel types or combustion strategies aimed at reducing thermal NOx.

NNH Mechanism: The NNH pathway involves the formation of NNH radicals (formed from N2 and H radicals). These radicals can then react with oxygen to form NO directly. This mechanism is more prominent in high-temperature, lean combustion environments, where there is an abundance of hydrogen atoms.

3.6.2 Engine management

To reduce emissions in hydrogen combustion engines, current research emphasizes optimizing key engine parameters like stoichiometric ratios and injection timing. Operating the engine slightly leaner

than the stoichiometric ratio and using retarded injection timing are effective strategies to minimize NOx emissions. These adjustments help lower combustion temperatures, thus reducing the formation of thermal NOx. Implementing such strategies requires advanced engine management systems capable of precisely balancing performance, efficiency, and emissions. (Stępień Z, 2024). Hydrogen combustion engines can achieve near-zero NOx emissions through precise control of stoichiometric ratios and injection timing. Operating slightly leaner than stoichiometric and employing retarded injection timings are effective strategies to minimize NOx emissions. Advanced engine management systems are essential to implement these strategies effectively, balancing the trade-offs between performance, efficiency, and emissions (Luo & Sun, 2018).

3.6.2.1 Slightly Lean Mixtures:

Operating with an equivalence ratio slightly leaner than stoichiometric (lean mixtures) can significantly reduce NOx emissions by lowering peak combustion temperatures. This approach helps maintain efficiency and power while controlling NOx formation. Maintaining precise control over the equivalence ratio is crucial, as NOx emissions tend to increase sharply beyond certain ratios (e.g., 0.7 to 0.9) (Rüde et al., 2022).

3.6.2.2 Advanced Injection Timing:

Early injection timings (e.g., before -80°CA BTDC) tend to increase NOx emissions due to higher localized temperatures and turbulence. Delaying the injection timing (around -80°CA BTDC) allows for better fuel-air mixing and lower combustion temperatures, which significantly reduces NOx emissions. Optimal injection timing improves brake thermal efficiency and power output while maintaining near-zero NOx levels (Zhao et al., 2024).

3.6.2.3 Hydrogen Purity:

Hydrogen purity significantly influences NOx formation during combustion. High purity hydrogen (99.998%) enhances engine performance parameters, such as indicated power and thermal efficiency, by increasing the in-cylinder pressure and temperature. This, in turn, accelerates the combustion process and reduces combustion duration. However, the higher combustion temperatures associated with high purity hydrogen led to increased NOx emissions. (Gurbuz, 2020).

3.6.2.4 Supercharging and EGR and Turbocharger Matching:

Supercharging and maintaining appropriate air-fuel ratios are crucial. To prevent backfire and pre-ignition, the air-to-fuel ratio is often limited, which can lead to higher NOx emissions. However, introducing exhaust gas recirculation (EGR) allows for stoichiometric supercharged operation, enhancing power output to levels comparable to gasoline engines while enabling efficient after-treatment (Stępień Z, 2024).

Proper turbocharger matching is essential to control NOx emissions. A decrease in the lambda value, especially in the full load range or at rated power, results in a rapid increase in NOx emissions, underscoring the importance of turbocharger performance in managing NOx levels during hydrogen combustion (Stępień Z, 2024).

3.6.2.5 Combustion Strategy:

Hydrogen engines running with lean combustion (high lambda values) show a significant reduction in NOx emissions. Lean operation helps reduce combustion temperature and thermal stress, which are primary factors influencing NOx formation. Direct injection strategies further aid in controlling NOx emissions by optimizing fuel-air mixing and combustion timing (Stępień Z, 2024).

3.6.3 Summary of engine management requirements

In summary, managing NOx emissions remains a crucial challenge. Strategies such as EGR, proper turbocharger matching, lean combustion, and advanced fuel injection techniques are essential to achieving low NOx emissions. Further research and optimization are needed to balance these factors effectively for sustainable hydrogen-powered transportation. Figure 18 below give a good overview of the interrelations of MEP, AFR and NOx and thermal efficiency as discussed in this paragraph.

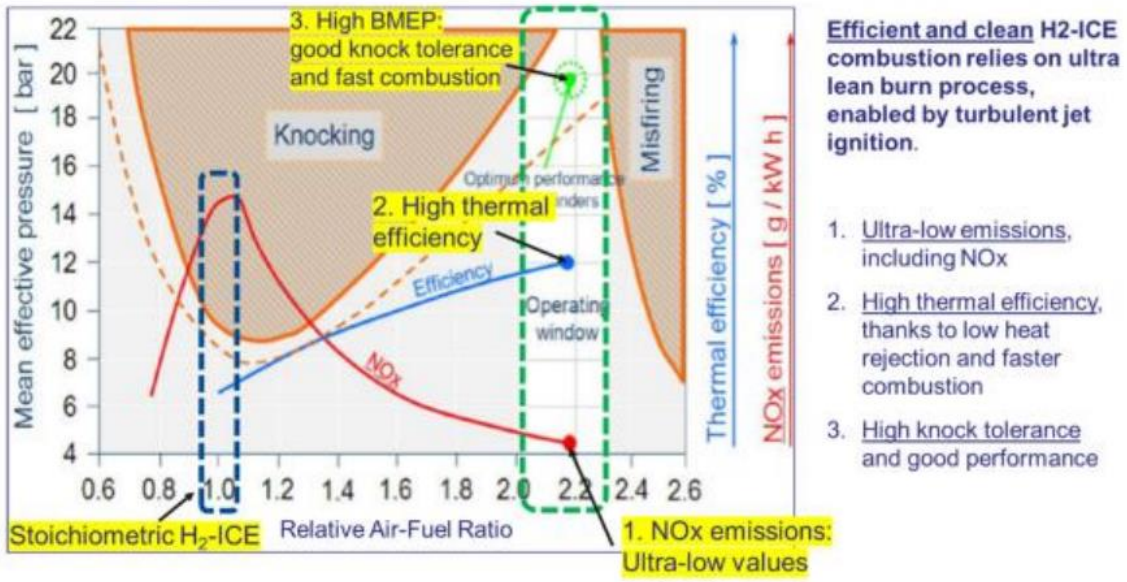

Figure 18 – Summary of engine management requirements (Stępień Z, 2024)

3.6.4 Hydrogen burner and electric heating

In this study, a hydrogen burner was considered to deliver additional heat when WHR was insufficient. According to Rao et al. (2022), burner efficiencies of up to 90% were achievable. Thus, despite the lower system efficiency, electric heating remains an option. Electrical heating is highly efficient on a component level, as most electrical heaters convert nearly 100% of the input electrical energy into heat.

3.6.5 Contamination/purification/hydrogen requirements for different power sources

Evaluating the purity of hydrogen released and required filtration is crucial to assessing the BOP for ship-installed reactors. According to Niermann, Beckendorff, et al. (2019), no additional hydrogen purification is needed post-dehydrogenation of DBT for ICEs and SOFCs. For PEMFCs, some H18-DBT thermally decomposes into smaller molecules like methane, benzene, and toluene. Activated carbon adsorbents used for purification prevent all but methane from reaching the stack, which, as per Lee et al. (2020), temporarily lowers stack output without damaging it. For PEMFCs, Geiling et al. (2021) used two activated carbon filters in series, achieving single-digit ppm levels for all hydrocarbons except methane. Methane, while permeable through these filters, did not damage the PEMFCs.

3.7 Review of the dehydrogenation reactor's system components and design

This section focuses on determining the heat required for the dehydrogenation unit by introducing a methodology to calculate the four primary heat fluxes critical to the energy balance of the dehydrogenation process. Maintaining the reactor at an appropriate temperature and pressure, as shown in Figure 19, is essential to facilitate the dehydrogenation reaction. Detailed insights into the reactor conditions and their impact on the dehydrogenation process are elaborated in a subsequent section.

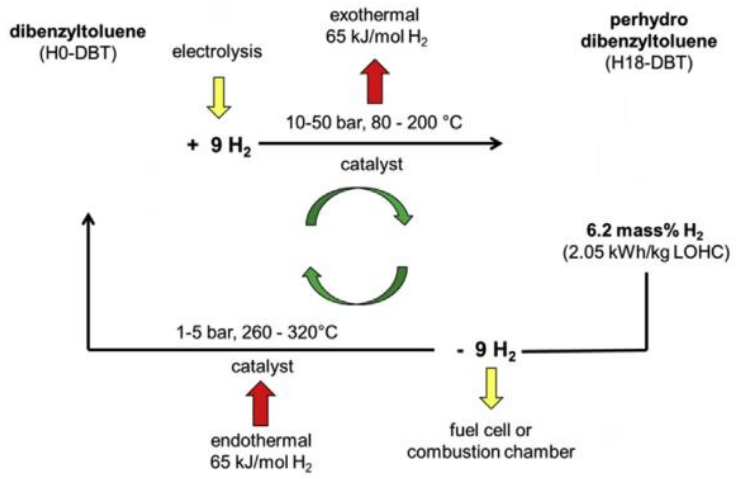

Figure 19 – Overview of simplified DBT cycle (Preuster et al., 2016)

3.7.1 Determining the energy balance of dehydrogenation

In 2018, Preuster et al. segmented the LOHC dehydrogenation unit into four thermodynamically significant sections: a heater, the dehydrogenation unit itself, and two sections for cooling and heat reclamation, as depicted in Figure 20.

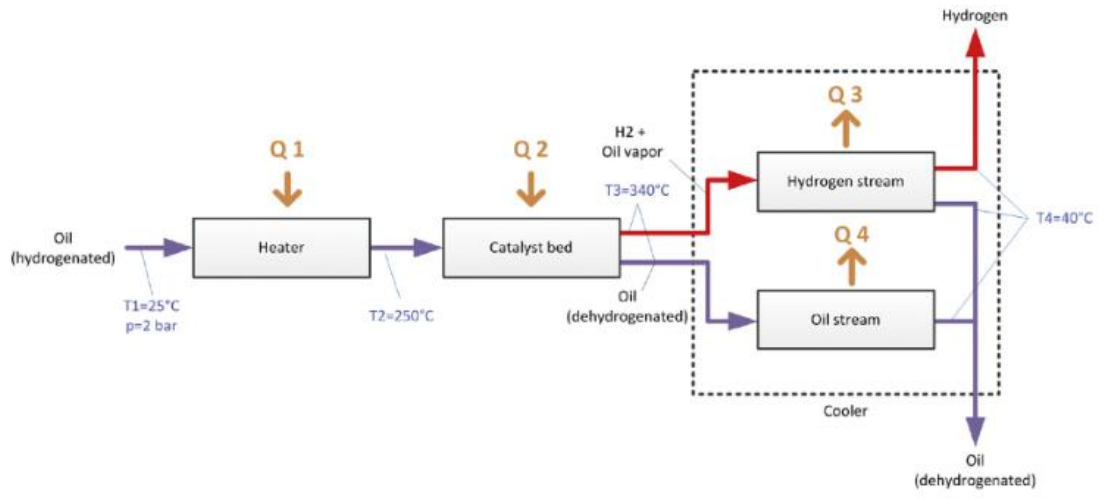

Figure 20 – Detailed energy balance of DBT dehydrogenation unit (Preuster et al., 2018)

Figure 21 presents the characteristic equations for calculating the heat fluxes. Q1, the preheating stage, involves heating H18DBT through direct heat exchange before it enters the reactor. Q2 quantifies the heat necessary for the endothermic dehydrogenation reaction within the reactor. Q3

and Q4 describe the processes in the cooler, aiming to reclaim as much heat as possible (Preuster et al., 2018):

$$Q1 = (\dot{n} \cdot c_p \cdot \Delta T_{2-1})_{Oil}$$

$$Q2 = (\dot{n} \cdot c_p \cdot \Delta T_{3-2})_{Oil} + (\dot{n} \cdot \Delta h_{Evaporation})_{Oil\ evaporated} + (\dot{n} \cdot \Delta h_{Dehydrogenation})_{Hydrogen\ produced}$$

$$Q3 = (\dot{n} \cdot c_p \cdot \Delta T_{4-3})_{Hydrogen} + (\dot{n} \cdot \Delta h_{Evaporation})_{Oil\ condesed} + (\dot{n} \cdot c_p \cdot \Delta T_{4-3})_{Oil\ condensed}$$

$$Q4 = (\dot{n} \cdot c_p \cdot \Delta T_{4-3})_{Oil}$$

Figure 21 – Heat fluxes in the dehydrogenation unit (Preuster et al., 2018)

3.7.2 Kinetic hydrogen release description

In their 2018 study, Preuster et al. derived heat fluxes to optimize the system layout, demonstrating its general feasibility and efficiency. Building on this, Peters et al. (2019) adopted this system layout to develop a kinetic model. A kinetic model mathematically represents the rate of a chemical reaction, providing a quantitative analysis of reaction kinetics and the factors influencing the reaction rate. Peters et al. found that a simplified kinetic model could accurately describe the dehydrogenation reaction far from equilibrium. The model's assumptions were as follows: only one reaction step from H18-DBT to H0-DBT was considered, the LOHC mixture was always saturated with hydrogen, and the back reaction from H0-DBT to H18-DBT was neglected. Based on a close match with their experimental data, Peters et al. (2019) described the H18-DBT dehydrogenation using a Pt on alumina catalyst according to Figure 22:

$$r = k_0 \cdot \exp\left(-\frac{Ea}{R\,T}\right) \cdot c_{H18-DBT}^{1.98} = 125.24\ s^{-1} \cdot \exp\left(-\frac{119.8\ kJ\ mol^{-1}}{R\,T}\right) \cdot c_{H18-DBT}^{1.98}$$

Figure 22 – Kinetic hydrogen formation relation (Peters et al., 2019)

This model provides a time- and temperature-dependent description of hydrogen formation rate. Despite its simplifications, the model developed by Peters et al. (2019) showed a very good fit with experimental data, as illustrated in Figure 23, and served as a foundation for modelling reactor performance.

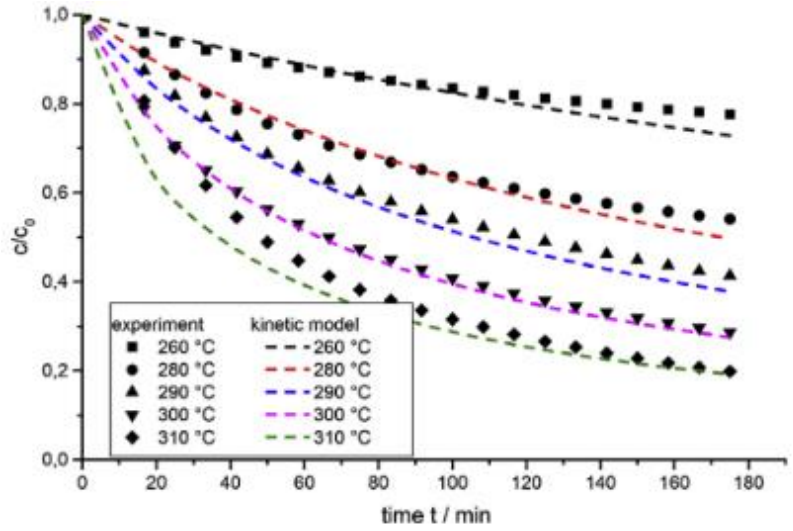

Figure 23 – Experimental data vs. model-based description during H18-DBT dehydrogenation in the temperature range between 260 °C and 310 °C; the vertical axis represents the dimensionless concentration (Peters et al., 2019)

3.7.3 Packed bed reactor performance modelling

In describing the dehydrogenation reaction, noting that the flow fields and heat transfer are intimately connected and significantly influenced by the hydrogen generation rate is imperative. In the reactor, higher hydrogen release at any point leads to increased flow velocities due to the substantial volume expansion of the gas. Consequently, as Peters et al. (2019) noted, a higher hydrogen release rate enhanced the heat transfer from the reactor's hot wall into its interior. Several simplifications were made in a model-based approach to model this intricate relationship. A 1D pseudo-heterogeneous model was employed to describe the dehydrogenation reaction in a horizontal tubular reactor, incorporating the following simplifications:

- The heat transfer from the wall to the liquid relied solely on the temperature at a specific position, represented through simple heat-transfer coefficients.
- These coefficients, measured in a system without chemical reaction, were a simplification.
- Axial dispersion in the reactor was not considered.
- A high degree of radial dispersion was assumed.

This model also offered a simplified and analytical solution for the hydrogen flow from the reactor. It enabled calculating the molar flow of hydrogen in a hydrogen release unit, with a Pt on alumina catalyst under steady-state conditions. The expression for hydrogen mass flow is shown Figure 24.

$$\dot{n}_{H_2} = 9 \cdot \eta_{LOHC} \cdot \dot{n}_{LOHC} \cdot \rho_{Kat} \cdot \tau \cdot k_0 \cdot \exp\left(-\frac{E_A}{R \cdot T_s}\right) \cdot (3120 \cdot \eta_{LOHC})^{1.98}$$

Herein:

$$\tau = \frac{3600}{LHSV \cdot 500}$$

$$LHSV = \frac{\dot{V}_{LOHC}}{V_{reactor} \cdot \varepsilon \cdot F_{RV}}$$

Figure 24 – Mass flow relation for PBR as a function of LHSV and temperature (Preuster et al., 2018)

Per Peters et al. (2019), the kinetic model equation can be applied to dynamic calculations with certain limitations, such as avoiding abrupt changes in LOHC molar flow and reaction temperature. This application enables the computation of a power output and dehydrogenation grade map as a function of temperature and LHSV for a specific reactor configuration in H18-DBT dehydrogenation based on a 99% hydrogenation grade.

3.7.3.1 Temperature dependency

Temperature significantly influences the hydrogen production rate in the dehydrogenation process of H18-DBT. According to the Arrhenius equation, the reaction rate constant k increases exponentially with temperature. This occurs because higher temperatures provide more energy to overcome the activation energy barrier EA, thus accelerating the reaction rate. Mathematically, the reaction rate constant K, is expressed as: $k(T) = A * e^{-\frac{Ea}{R*T}}$, where k_0 is the pre-exponential factor, R is the universal gas constant, and T is the absolute temperature in Kelvin. As the temperature increases, the exponential term becomes larger, leading to a higher reaction rate constant. Consequently, this results in an increased rate of dehydrogenation of H18-DBT, producing more hydrogen. Higher temperatures enhance the kinetics of the reaction, making the process more efficient. However, excessively high temperatures can lead to potential issues such as catalyst degradation or unwanted side reactions. Therefore, optimizing the temperature is crucial for maximizing hydrogen production while maintaining the integrity of the catalyst and the overall process efficiency.

3.7.3.2 LOHC flow rate dependency

LHSV is defined as the volumetric flow rate of the liquid feed divided by the volume of the catalyst, is crucial for determining the residence time of reactants over the catalyst. As LHSV increases, the residence time of the LOHC in the reactor decreases, as they are inversely related. This means the LOHC spends less time in the reactor, potentially reducing the efficiency of the dehydrogenation reaction if the residence time becomes too short. However, a moderate increase in LHSV can enhance throughput, improving overall hydrogen production. The optimal LHSV balances residence time and flow rate, maximizing hydrogen production without compromising the reaction efficiency. In practical terms, maintaining LHSV within a specific range (typically between 1 and 10 h^{-1}) ensures sufficient contact time for the reaction while enabling a higher processing rate of LOHC, optimizing the hydrogen production rate. Looking at the description in Figure 24 where τ is linearly related to produced hydrogen an effect of LHSV of about a factor 10 is expected for the effect of LHSV on hydrogen production of the reactor.

3.7.3.3 Practical use of the 1D heterogenous model for system modelling

The 1D heterogenous model developed by Peters et al. (2019) accounts for heat and mass transfer with all necessary chemical and electrochemical reactions. The result of this model is useful for determining the coupling with maritime propulsion systems as the power output as a function of dehydrogenation grade, temperature, and LHSV. The resultant map illustrating these dynamics is displayed in Figure 25.

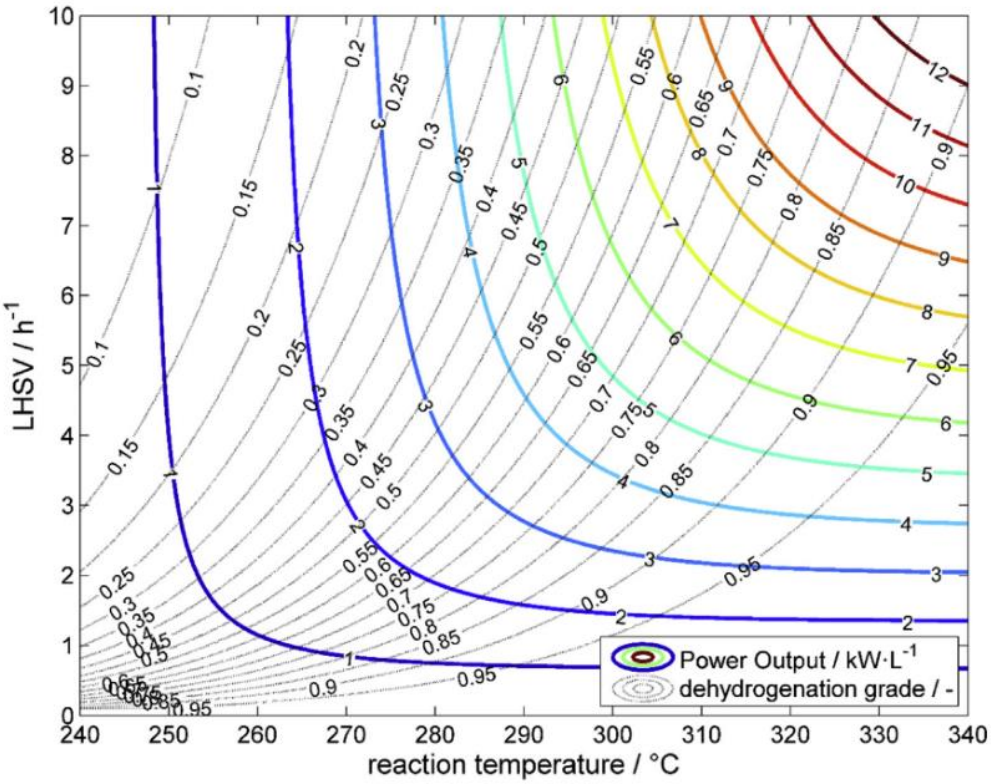

Figure 25 – Power output and dehydrogenation grade as a function of temp and LHSV for DBT and 99% conversion; results are specific to the system design (Peters et al., 2019)

3.7.4 Alternative reactor descriptions from the literature

The 1D heterogenous model is well suited for this research purpose, but there are (less or equally suitable) alternatives and these should be considered.

3.7.4.1 Ideal CSTR reactor modelling

Three ideal reactor types and models are described in literature: a continuously stirred tank reactor (CSTR), vertical tube bundle reactors, and packed bed reactors (in simplified form, they can be described by a PFR model). For an overview of the CSTR & PFR reactor models encountered in the literature study, please refer to the table in Appendix B.

A CSTR is designed to ensure perfect mixing so that the output concentration is the same as the concentration in the reactor itself. It often involves a chemical reaction, and the residence time can control the output product concentration. The operation of a CSTR is straightforward because it operates at a steady state. All parameters (e.g., temperature and concentration) remain constant, and there is no time dependency, simplifying the control and operation of the reactor.

Lee et al. (2020) used a standard CSTR reactor, realizing a fuel utilization of 85%. They observed that increased temperature initially led to increased hydrogen flow, which subsequently decreased as reactant levels decreased. This reactor model described a batch that tried to keep sufficient mass flow to the PEMFC operated at constant power by raising the temperature. Hence, this model was less suited to the application of this study.

3.7.4.2 Cascade CSTR model for fixed bed cuboid reactor

Geiselbrech M et al. models the continuous dehydrogenation of H18-DBT in a cuboid fixed bed reactor using reaction kinetics and a cascade of continuously stirred tank reactors (CSTRs). Initially, reaction kinetics are determined by measuring the reaction rate at various temperatures and pressures, establishing activation energy and pre-exponential factor using the Arrhenius equation. The reactor is then modelled as a series of CSTRs, each representing a small, uniform volume within the larger reactor. This sequential CSTR approach updates reactant concentrations and reaction rates as the flow progresses from one tank to the next, allowing for a detailed simulation of the reaction progress. In the simulation phase, the integrated reaction kinetics and reactor design predict hydrogen flow rates under different operating conditions. The model's accuracy is validated by comparing simulated hydrogen flow rates with experimental data. The cascade CSTR method divides the reactor into multiple smaller CSTRs arranged in series, where the output of one serves as the input for the next. This iterative process captures the dynamic behaviour of the dehydrogenation process, providing a more accurate representation of reactor performance compared to a single CSTR model. The approach effectively predicts the reactor's behaviour, ensuring the model aligns well with experimental observations (Geiselbrech M et al, 2024). Due to the complex modelling of the cascade setup and less direct correlations to the input parameters this approach is less suited for this study.

3.7.4.3 High power density crossflow inverted fixed bed reactor

A constraint on ships is the system footprint so design with high volumetric energy density like the (DehyMax) cross flow inverted reactor might be preferred over less energy dense PBR reactors. It is out of the scope of this study to review the system footprint, but within scope to determine possible suitable reactor configurations. Kadr J et al introduces an inverted fixed-bed reactor design named DehyMax. In this design, LOHC flows upstream while hydrogen is released in the reactor housing, and crossflow heating is achieved through perpendicular heating tubes. The inverted design increases the catalyst volume per reactor volume, leading to higher power densities. This arrangement offers a more efficient heat transfer and higher catalyst utilization compared to traditional fixed-bed reactors. The reactor achieved power densities of up to 0.76 kW H2/L reactor-outside and 2.34 kWH2/L reactor-inside, significantly improving hydrogen release rates. The study found that the inverted design enhances heat transfer and allows for more efficient catalyst utilization. It maintains a higher catalyst volume to reactor volume ratio, improving overall performance. Higher reaction temperatures led to higher DoDH. For example, at a heating rod (HR) set temperature of 320°C, the DoDH achieved was 0.65 compared to an equilibrium DoDH of 0.88. (Kadar J et al ,2024).

3.7.4.4 H12 DBT and the benefits on reactor design

H12-DBT offers several advantages over H18-DBT, including lower dehydrogenation temperatures, higher reaction rates, better catalyst stability, lower viscosity, and higher vapor pressure. These factors make H12-DBT a more efficient and practical choice for LOHC applications, particularly in environments where low-temperature performance and high-purity hydrogen production are critical.

H18-DBT has a higher energy density compared to H12-DBT due to its higher hydrogen content kilogram (H18-DBT: 3.85 kWh/kg vs H12-DBT: 2.72 kWh/kg). But H12-DBT requires a lower temperature and less enthalpy for hydrogen release compared to H18-DBT. Specifically, for 90% hydrogen release at 2 bars. (Rüde et al., 2022). H12-BT dehydrogenation was 30% more productive than H18-DBT dehydrogenation under identical conditions. (Jorschick et al., 2020)

3.7.4.5 Multiphase *CFD-model*

The dehydrogenation of H18-DBT in fixed-bed reactors is a complex process requiring a detailed understanding of reaction kinetics and precise control of pressure and temperature. Computational Fluid Dynamics (CFD) offers an advanced method for modelling and optimizing these aspects, providing several advantages over traditional experimental approaches.

CFD allows for the incorporation of detailed kinetic models derived from experimental data, predicting the concentration profiles of reactants and products over time. This helps in understanding the efficiency and progression of the dehydrogenation process. Additionally, CFD simulations can model thermal behaviour within the reactor, identifying hot spots and ensuring uniform temperature distribution to maintain optimal operating conditions.

Pressure control is crucial due to the significant volume of hydrogen gas produced during dehydrogenation. High hydrogen partial pressure can hinder the contact between liquid H18-DBT and the catalyst, reducing the reaction rate. CFD models can simulate multiphase flow dynamics, allowing for the analysis of gas-liquid interactions and the optimization of reactor pressure to facilitate efficient hydrogen removal and prevent gas pocket formation.

CFD offers specific advantages for modelling H18-DBT dehydrogenation. It provides detailed visualization of the flow, temperature, and concentration fields within the reactor, which are difficult to measure experimentally. CFD can perform sensitivity analyses on various parameters, such as catalyst size, reactor dimensions, and inlet flow rates, to understand their impact on reactor performance. This predictive capability helps in optimizing reactor design and operation before physical trials, saving time and resources.

In conclusion, CFD is a powerful tool for understanding and optimizing the dehydrogenation of H18-DBT in fixed-bed reactors. By accurately modelling reaction kinetics and providing detailed insights into pressure and temperature control, CFD enhances the efficiency and effectiveness of the dehydrogenation process, leading to better reactor designs and operational strategies. (Diaz D., 2024).

3.7.5 Reactor control

Primary functions of reactor control is to ensure it stays within operating temperatures and pressures and the secondary function is to ensure the required setpoints are met in an efficient manner.

Peters et al. (2019) and Preuster et al. (2018) assumed constant pressure in the reactor description and used the volumetric flow rate and temperature to determine the reactor's output. They found that the dehydrogenation grade was a function of the operating point, with successful coupling with an SOFC. Geiling et al. (2021) proved that reactor output control is best performed by controlling pressure instead of temperature and feed flow. Moreover, Fikrt et al. (2017) noted that due to the free volume in the reactor, the dynamics of power demand were best adapted by altering pressure since they reacted much faster than temperature.

In comparison, Geiling et al. developed a pressure-based control algorithm that enabled a stable operating behaviour within the permissible input pressure range of the reactor's fuel cell of 2.2–3 bars and successfully coupled the reactor and PEMFC for dynamic behaviour. The pressure-based control strategy was the only strategy that interrupted the hydrogen release. Moreover, it was the only control method that could react this quickly since temperatures required 20 minutes and feed flow for one hour to take full effect of the reactor mass flow, as shown in Figure 26.

SOFC has load transient times from 0% to 100% of more than 5 minutes, while PEMFC and H2ICE transient times require seconds or minutes (Mestemaker et al., 2019). The significant difference in transient capabilities allows reactor control with temperature and feed for SOFC but not PEMFC and H2ICE unless buffer size is no issue. However, ship designs are often size-constrained. Smaller buffers positively affect the system's footprint and safety since there is less gaseous H2. However, optimizing component size is out of the scope of the study. Figure 26 shows the difference in hydrogen mass flow depending on the control parameter.

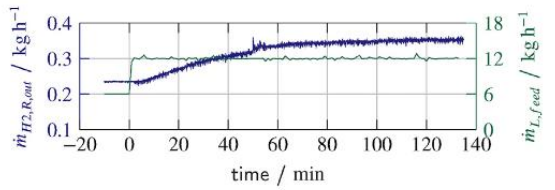

(a) Increase of the LOHC feed mass flow at a thermostat set temperature of 330 °C and a reactor pressure of 3 bar(a) (exp. 1)

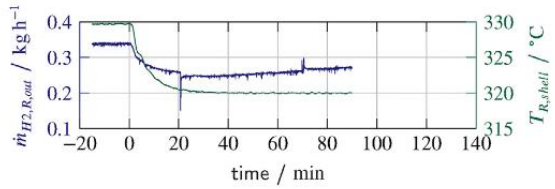

(b) Decrease of the temperature of the thermal oil in the reactor shell at a LOHC feed mass flow of 9 kg h^{-1} and a reactor pressure of 3 bar(a) (exp. 2)

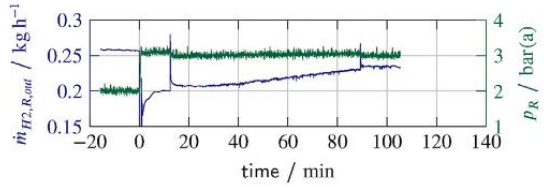

(c) Increase of the reactor pressure at a LOHC feed mass flow of 6 kg h^{-1} and a thermostat set temperature of 330 °C (exp. 3)

Figure 26 – Change in reactor mass flow in tube bundle reactor as a function of temperature, pressure, and feed flow (Geiling et al., 2021)

(Gambini et al., 2024) also develop a PI-controller to manage hydrogen release by independently controlling: discharge pressure, thermal fluid inlet temperature, and thermal fluid mass flow rate. Controlling the thermal fluid inlet temperature is identified as the most effective method, achieving efficiency levels above 90% across the entire load range. This strategy ensures a consistent hydrogen release, making it well-suited for various power demands. Pressure control, while effective at low loads, shows a decline in performance with increasing power demands. It maintains satisfactory performance only up to mid-range loads. Mass flow rate control is found to be the least effective, with efficiencies generally below 80%. The study also highlights the importance of maintaining an optimal balance between heat recovery and the energy required for the dehydrogenation process. This balance is crucial for minimizing costs and enhancing the overall efficiency of LOHC systems. A multiparameter approach, combining moderate regulation of mass flow rate with temperature and pressure controls, could further improve the controllability and efficiency of hydrogen release from DBT.

3.7.6 Heat exchangers

As input parameters, the efficiency of the heat exchangers is 85% and a minimum heat exchanger temperature difference of 10K (Li et al., 2021), while the minimum temperature difference is 10 K. Preuster et al. (2018) used an air-based heat exchanger for the hot exhaust gases from the SOFC to heat the reactor. This principle could also be used for H2ICE. The design of this heat exchanger is shown in Figure 27

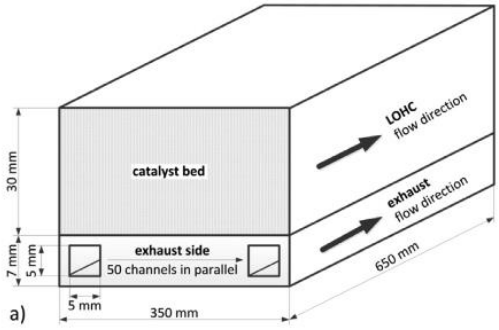

Figure 27 – Design of reactor heater from SOFC exhaust gases and model validation (Preuster et al., 2018)

This study does not design or specify the heat exchanger on the exhaust side of the H2ICE. Several suggestions for heat exchangers (finned, shell and tube, were found in literature (Jouhara, H., 2018) but an integration of the heat exchanger efficiency as function of the engine operating point or a determination of the efficiency for the modelled system is out of the scope of this study. This study quantifies the available exergy in the exhaust and assumes a heat exchanger efficiency to transfer the thermal energy to the reactor.

Geiling et al. (2021) used a vertically installed tube bundle reactor heated by a thermal oil circuit and four electric heaters. A tube bundle reactor is a heat exchanger widely used in process engineering where a gas or liquid flows inside tubes, and another gas or liquid flows outside the tubes within a shell. The design provides a large surface area for heat transfer, allowing higher heat exchange rates between the two fluids. The design of tube bundle reactors can lead to a pressure drop, especially if a highly viscous fluid (H18-DBT) is involved. Hence, additional energy is needed to pump the fluids through the system. The design and manufacturing processes of a tube bundle reactor can be

complex due to the need for many tubes and the requirements for precise alignment and secure sealing, which can add to the upfront cost of such a system. One advantage when modelling tube bundle reactors is that they can be scaled by addition to increased capacity.

Rao et al. (2022) developed a PBR model based on a 1D model at different feed temperatures, wall temperatures, and hydrogen burner efficiency to determine the energy required by the dehydrogenation reactor. Heat exchanger areas and quantity of catalyst required were specified so that the conversion reached 99%, producing 10 Nm3/hr of industrial-grade hydrogen. The reactor dimensions (length and heat exchanger areas) and conditions (feed temperature and catalyst weight) were cost-optimized in that study. However, in this study, cost optimization was not the goal. Nevertheless, the dependencies that Rao et al. found were interesting since they showed the dependency of heat exchanger areas on the feed and wall temperatures in the reactor. Useful for verification/estimate of the reactor and heat exchanger areas .

Kadar et al. (2024) look at the heat exchanger types for the exchange between hot gasses (in their case SOFC exhaust gasses) and their observation supports the fact that the most suitable heat exchanger for gas to liquid interface (as with H2ICE exhaust) is the plate heat exchanger, due to the fact it excels with high viscosity fluids (H18-DBT) and has high heat transfer capabilities.

Heat Exchangers Types	Description	Advantages	Disadvantages
Tubular heat exchanger	Favored for efficiency in high-pressure, high-temperature settings; finned variants improve surface area and efficiency.	Durable under high temperatures and pressures.	Lower heat transfer efficiency and cumbersome maintenance.
Plate heat exchanger	Excel with high-viscosity fluids in sludge treatment; plate-fin designs are space-saving but may have leakage issues.	High heat transfer efficiency in a compact form.	Potential leakage issues and struggles with high-temperature resistance.
Finned heat exchanger	Enhance surface area for better heat transfer; prone to fouling.	Enhanced heat transfer capabilities.	Requires careful handling due to fouling.
Counterflow and crossflow heat exchangers	Excel in applications with significant temperature differentials; highly efficient but complex and costly.	Excellent thermal efficiency and adaptability.	Increased complexity and cost considerations.
Compact heat exchanger	High surface-area-to-volume ratio; efficient and space-saving but higher fabrication costs and fouling issues.	Exceptional efficiency and space-saving advantages.	Higher fabrication costs and maintenance challenges due to fouling.

Figure 28 – Overview of heat exchanger types (Kadar, J. 2024)

3.7.7 Design restrictions for reactors at sea

Chemical reactors have been primarily designed for stationary applications, which may present a substantial obstacle in developing reactor systems. To operate effectively on a ship, a reactor must be designed or adapted to either be independent of the ship's movement or function with fluctuating flow patterns caused by the vessel's motion. The reactors studied for suitability by (Hoecke et al., 2021) are the tubular reactor, the CSTR, membrane reactors, and vortex field reactors. According to Hoecke et al., tubular reactors do not seem suitable for application onboard ships as the ship's movement would heavily interfere with the flow character of the reactor, and they are not space efficient. Membrane reactors are expensive and susceptible to damage to the membrane. Vortex field reactors can be operated in states with negligible gravity, but these systems are still in the conceptual phase. In discussions with Dr. IR. J.T. Padding from the department of complex fluid processing at the TU Delft, unsuitability of reactors as stated by Hoecke were doubted. For instance, tubular reactors in simulation models can be easily designed to cope with variations in gravity, while CSTRs are intuitively more open, so sloshing can occur in movement. A packed bed has hydrodynamic resistance that depends on the catalyst particles as ship movements are fast concerning changing fluid and gas in the reactor. However, further detailed reactor modelling is necessary to determine feasibility with certainty. Thermal energy storage – WHR strategy 5

A heat buffer offers several advantages. If the power source can adjust its output over a specific period, and the average heat during that time suffices for the dehydrogenation reaction, power fluctuations may not significantly affect thermal stability. The heat buffer is assumed to have a 95% efficiency, as noted by Li et al. (2023) and Obara (2019). Additionally, it enhances reactor controllability, particularly when the heat source experiences fluctuations, like in H2ICE applications. This improved control helps maintain the LOHC within its optimal temperature range, reducing degradation. Given that H0-DBT is often used as heating oil, the heat buffer can effectively utilize its properties.

Thermal Energy Storage (TES) is well-suited for recovering residual heat due to its high storage capacity and ability to maintain stable temperatures during charge and discharge (Douadi, O. 2022). Uniform heat distribution in the reactor is essential to prevent DBT degradation, but exhaust gases fluctuate in temperature based on load and RPM, making them ineffective for direct heating. This variability complicates reactor control, whereas TES can provide a more consistent temperature profile. Although a common challenge with TES is time mismatch (Douadi, O. 2022), this is not a concern in the integration of H2ICE and the reactor. While TES could benefit the system design, this research does not incorporate it, focusing instead on energy balance at specific operation points rather than an entire operational profile. Future research will explore the benefits of integrating TES, considering its size relative to H2ICE and the reactor, as well as the operational requirements.

3.8 Catalyst

Finding a catalyst that reduces temperature while recovering all the hydrogen stored is a challenging task and the subject of current research for many LOHCs (Van Rheenen et al., 2022). DBT has a dehydrogenation temperature of 583 K when using palladium on a carbon catalyst (Niermann et al., 2019). It can be reduced to 543 K, yet only 58% of the hydrogen is released (Sekine & Higo, 2021). Lang et al. (2020), Rao and Yoon (2020), and Sekine and Higo (2021) suggested that Platine could be an improved catalyst for DBT based on publications. However, Asif et al.'s (2021) catalyst performance optimization analysis showed that the most suitable catalyst for the DBT dehydrogenation was 2 wt.% Pt/Al2O3 with optimum temperature and pressure conditions at 593 K and 2 bars, respectively. It was beyond the scope of this research to define the optimum catalyst, in line with most of the literature (Geiling et al., 2021; Peters et al., 2019; Preuster et al., 2018; Zhang et al., 2023), so Pt/Al2O3 was used.

3.9 Detailed gap analysis

Three topics were identified for further gap analysis based on an overall understanding of the available literature to formulate the research questions, justify the research, and understand the state of the art:

1. The coupling between the power converter and the dehydrogenation reactor to examine the feasibility and the behaviour under load change;
2. WHR strategies employed and efficiency gains realized;
3. The quantification of system performance with energy and exergy analysis.

3.9.1 Coupling and system-level performance

Hydrogen-release dynamics are crucial for energy storage applications, especially for mobile applications (Fikrt et al., 2017; Hoecke et al., 2021). The connected operation of PEMFCs and SOFCs with dehydrogenation reactors was studied in detail by Geiling et al. (2021), Peters et al. (2019), and Preuster et al. (2018). These studies quantified system performance and behaviour, proving that both types of fuel cells could operate without damage on dehydrogenated hydrogen with operational stability. Moreover, the coupled systems could keep up with the load-following capabilities of the power converter.

Regarding PEMFC, Geiling et al. (2021) demonstrated a dynamic combined operation of a continuously operated LOHC reactor and introduced a simple, robust, and powerful PI control strategy. The dehydrogenation system used a tube bundle reactor heated with a heating fluid. The demonstration showed that coupling the PEMFC and reactors was feasible and that the dynamic operation of PEMFC with hydrogen fed from the reactor was possible. The control strategy halved the buffer size, but a buffer was still necessary. The PEMF system required activated carbon filtration, which limited its long-term operation. Another method of managing contaminants is the purge rate. Despite the necessary purge rate, a fuel utilization of 90% was reached. For the SOFC case, the higher resistance of impurities of the SOFC required no filtration. Dynamic coupling was possible without a buffer, likely due to the slower transient behaviour of SOFC, making demand following the reactor possible. Peters et al. (2019) devised a protocol for managing load variations and system shutdown procedures. This protocol demonstrated that the integrated system comprising LOHC dehydrogenation and SOFC exhibited moderate dynamics but was effectively operational.

Several other studies (Kwak et al., 2021; Lee et al., 2020; Niermann, Drünert, et al., 2019; Seidel, (Kwak et al., 2021; Lee et al., 2020; Niermann et al., 2019; Seidel, 2019) examined coupling for PEMFC and SOFC but underwrote the findings of Geiling et al. (2021), Peters et al. (2019), and Preuster et al. (2018) with some added detail on fuel cell degradation and purification needs. Therefore, no literature gap exists on coupling PEMFC and SOFC to dehydrogenation reactors on the system level of this study. However, previous studies have not examined the coupled operation of a hydrogen ICE using DBT as a hydrogen carrier (Boretti, 2020; Korn & Volpert, 2019; Onorati et al., 2022; Verhelst, 2014). All studies have discussed the merits of H2ICEs and the potential drawbacks. There appears to be a consensus that these ICEs will find their way into maritime propulsion systems. Given that H2ICEs have a transient behaviour (like the PEMFC) and the tolerance to impurities that H2ICE and possibilities for WHR, understanding the coupling between LOHC dehydrogenation and H2ICE is critically relevant for maritime propulsion systems.

3.9.2 WHR and the system-level performance

Li et al. (2023) showed that proper thermal management could improve the efficiency of hydrogen storage chains, with the largest efficiency gains for DBT. With a thermodynamic modelling study, the authors reviewed the integration with PEMFC, SOFC, and the reactor for the efficiency gains of various WHR strategies. They found higher system efficiencies than more conventional compressed

or liquified storage chains. The increase in efficiency was approximately 35% efficiency and 25% exergy increase for SOFC, with a 40% efficiency increase and a 10% exergy increase for PEMFC. However, these results were based on the full cycle of dehydrogenation and hydrogenation (for stationary energy storage).

For the SOFC case, Peters et al. (2019) and Preuster et al. (2018) studied the WHR potential in the system and found that the integration was a compelling method for efficiently transferring heat between the endothermic hydrogen release process and the exothermic operation of the fuel cell. Dehydrogenation was fully supported with WHR. The high-temperature SOFC exhaust gases proved valuable in increasing efficiencies and exergy due to the possibility of direct heat transfer. However, in the system design, attention was required to avoid critical conditions of the components. Peters et al. (2019) demonstrated that the maximum efficiency of DBT-bound hydrogen to electricity is 45% at full load with WHR.

WHR in PEMFC is a challenge because even though around 50% is heat loss, the temperature of the coolant (80 °C) is low relative to dehydrogenation temperatures (>250 °C), posing challenges in the heat transfer for the rector. Geiling et al. (2021) used electric heating and heating oil with a basic WHR strategy (preheating H18-DBT with H0-DBT) similar to Li et al. (2023), but gains were not quantified. He et al. (2016) discussed the thermal efficiency gain using an ORC on the cooling system and found standalone PEMFC system efficiency, with increased electrical power of 4.7%. Baroutaji et al. (2021) suggested that WHR opportunities for the scale of maritime powerplants are thermodynamical power cycles like the ORC. An additional challenge is that the stack must be kept at a uniform, optimum temperature to ensure its durability.

Baldi et al. (2014) and Baldi and Gabrielii (2015) calculated the amount of energy and exergy available for the WHR in the maritime application of conventional ICE. They compared it with the propulsion and auxiliary power needs based on a ship's operational profile. The expected exergy efficiency of the WHR system was used as an independent variable, thus allowing estimating the expected fuel savings when a detailed design of the WHR system was not yet available. The results suggested that fuel savings of 5% to 15% could realistically be expected, depending on the waste heat sources used and the expected efficiency of the WHR system. Both power fuel injection (PFI) and direct injection (DI) H2ICE systems show significant potential for increased efficiency through optimizing energy and exergy recovery with WHR (Wang et al., 2019; Zhang et al., 2023). In PFI, significant energy is lost in exhaust gas and cooling systems, suggesting opportunities for improvement in overall thermal efficiency through waste energy recovery. The concept of coupling an H2ICE and reactor with WHR from H2ICEs for dehydrogenation has not been previously proposed in the literature and is novel.

3.9.3 Comparing system-level performance

Apart for the developed model by Li et al., 2023 a comparative study has not been performed and was challenging since large variations existed in the system and research setups when comparing the current literature, for instance:

- Different modelling approaches, as partially shown in Appendix A.
- Various reactor kinetic descriptions of the reactors used in modelling, each with its own assumptions and somewhat different reactor conditions as shown in Appendix B.
- Variations in the BOP influencing efficiency while complicating comparisons between systems.
- WHR strategies used vary among studies, complicating comparisons.
- Early study's focus on the steady-state feasibility of coupling at the lab scale since studies looking at integrating these systems and variable loads have been limited.

- The limited number of studies on mobility applications versus stationary applications, where hydrogenation and dehydrogenation were reviewed but not specified separately concerning efficiency or exergy.
- No studies for H2ICE coupling.

3.9.4 Overview

Table 1 overviews the gap assessment.

Table 1 – Gap overview

	PEMFC	**SOFC**	**H2ICE**
Comparative analysis on the systems level	**Partial gap**: Limited applicability of full cycle analysis as performed by Li et al. (2023) and a large variation in the setup between SOFC- and PEMFC-specific studies	**Partial gap:** Limited applicability of full cycle analysis as performed by Li et al. (2023) and a large variation in the setup between SOFC- and PEMFC-specific studies	**Gap**
Coupling with dehydrogenation reactor	Coupling was modelled and tested, with a good description in the literature (Baroutaji et al., 2021; Geiling et al., 2021; He et al., 2016)	Coupling modelled and tested with a good description in the Literature (Peters et al., 2019; Preuster et al., 2018).	**Gap**
WHR potential	A good description of possible methods in the literature, but WHR efficiency and exergy gain quantification were limited to the steady-state case for DBT dehydrogenation (Baroutaji et al., 2021; Geiling et al., 2021; He et al., 2016; Kandlikar & Lu, 2009; Li et al., 2023)	Excellent description of WHR strategies, including system design optimization (Peters et al., 2019; Preuster et al., 2018)	Clear quantification of available energy and exergy from H2ICE WHR but not applied on de application of dehydrogenation (Wang et al., 2019; Zhang et al., 2023)
System-level performance (exergy and energy)	A good description of performance and transient behaviour; energy efficiency was clearly stated, but exergy was less so (Geiling et al., 2021)	A good description of performance and transient behaviour; energy and exergy efficiency were clear (Li et al., 2023; Peters et al., 2019; Preuster et al., 2018).	**Gap**

3.9.5 Filling the gap – defining modelling objectives

The main GAP in literature is in the modelling of H2ICE and dehydrogenation systems and is thus chosen as the goal of the model developed this study. The characteristics of the H2ICE systems were derived by modelling the energy inflow and outflow using the empirical data available from the presented engine descriptions. These characteristics provided insights into how fuel energy is converted, transferred, utilized, and lost in terms of quantity. The objective was to calculate system efficiency and exergy based on thermodynamics' first and second laws to provide a system-level overview of the propulsion systems, which involved expressing mass balance, energy balance, and exergy balance for H2ICE power converters.

This research aims to develop a system-level model to determine the feasibility and characteristics of coupling a dehydrogenation reactor with WHR form an H2ICE. Modelling the coupling of H2ICE and dehydrogenation reactor will give insights into mass and energy balances and determine if the dehydrogenation reaction can be driven with WHR. This model will utilize the energy balance of H2ICE, empirical engine data and a 1D reactor model, which in combination with the essential balance of plant will give a conceptual description of this possible future propulsion system. As a result, it can be determined if LOHC and H2ICE systems can deliver fossil fuel-like bunkering properties and deliver efficient power delivery comparable to conventional ICE systems at zero emissions. A modelling strategy was to set the mass flow rate of hydrogen sources at a predetermined level for a given PLF, with all mass and energy balances for the components computed to determine energy efficiency and exergy as performed by Ye et al. (2022) for NH3 and LH2 based PEMFC systems.

4 Developed system model

The methodology of this study was a literature review to gain a comprehensive understanding of the components of the proposed future propulsion system. This understanding was necessary to identify the influential parameters and governing equations essential for the subsequent phase of the research, where a system model was then developed using the MATLAB and Simulink environment.

The MATLAB scripts described are integral components of a comprehensive analysis and modelling framework for evaluating engine performance, heat management, and energy efficiency in H2ICE and dehydrogenation systems based on the equations described in chapter 3. The scripts perform calculations related to power output, fuel flow, heat fluxes, and exergy values under various operating conditions, both with and without Waste Heat Recovery (WHR). The entire script is added for reference in paragraph 11. A broad overview of modelling approach shown in Figure 1 inspired by (Ye et al, 2022) describes the decisions that are being made in the steps of the model.

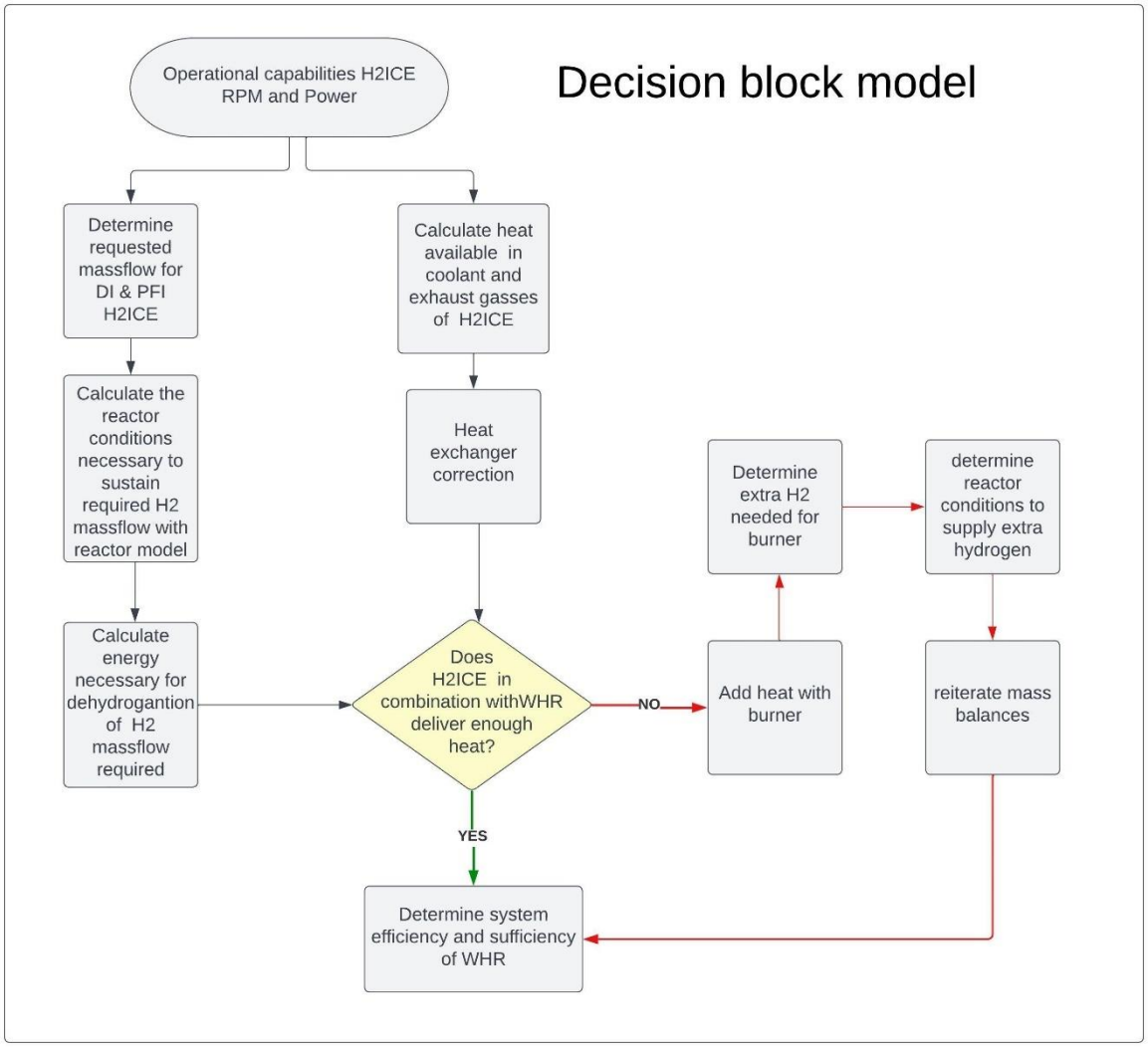

Figure 29 – Decision block model H2ICE

4.1 Sizing of components – scaling reactor to fit H2ICE model

Since max power of the DI H2ICE is 80kW and the study by Peters et al 2019, is at 5 kW scale, the reactor volume was multiplied with 16 for the DI model. The scaling of the reactor, to increase the hydrogen flow to fit the H2ICE empirical model size is supported by the relationship between LHSV and reactor volume. Since the hydrogen flow rate is directly proportional to the residence time. Specifically, the hydrogen flow rate be increased by extending the residence time, which is inversely proportional to LHSV. As LHSV is further inversely proportional to reactor volume, increasing the reactor volume decreases LHSV, thus increasing the residence time and, consequently, the hydrogen flow rate. Peters et al, 2019, specifies that scaling geometrically similar reactors using the same catalyst material can predict performance as a function of temperature and LHSV. This means that increasing the reactor volume should theoretically allow for an increased hydrogen flow rate, if the system's other parameters (e.g., temperature, catalyst efficiency, active reactor fraction, catalyst porosity, etc) are maintained appropriately.

4.2 H2ICE - Power and fuel flow calculations

The scripts calculate and display the power output for all operating points of BMEP and RPM for both DFI and PFI engines and computes fuel flow rates for these combinations. Visualization tools are included to surface plots that display fuel flows and for the DFI and PFI engines.

4.3 Reactor conditions - LOHC mass flow rates and dehydrogenation grade data processing

The script then calculates the reactor power output depending on LHSV and the reaction temperature. It determines the volume and mass flow rates for LOHC and H_2, comparing the mass flow of H_2 with required values for the H2ICE. The script identifies and stores conditions where the calculated mass flow is within a specified tolerance of the required value, presenting the filtered results in a readable table format. The script then processes dehydrogenation grade data from an Excel file based on the 1D reactor model of (Peters et al., 2019), combining it with previously calculated power-related results and filtering the data based on user-specified criteria. It reads the relevant data, extracts temperature and LHSV values along with the corresponding dehydrogenation grades and computes the dehydrogenation grades. The script integrates the dehydrogenation grades and corrects the mass flow rates for dehydrogenation grade and stores them into the results table. The user presets a threshold for dehydrogenation grades and the script filters the operating points from the results table that are within the power and dehydrogenation requirements accordingly

4.4 Heat Flux Calculations and Optimal Scenario Identification

The script then calculates the required heat fluxes for the reactor system, integrating temperature and dehydrogenation data to identify the scenario with the lowest absolute heat flux requirements. It defines temperature constants for coolant, ambient conditions, reactor input, and spent DBT cooling, sets specific heat capacity for hydrogen and its evaporation enthalpy, and defines efficiencies for four heat exchangers. The script iterates through the filtered dehydrogenation results, retrieving temperatures, calculating densities and mass flows for H18-DBT and H_2, using polynomial approximations to calculate specific heat capacities, and computing various heat fluxes (Q_coolant, Q1, Q2, Q3, Q4). It stores the calculated heat flux values, identifying and displaying the scenario with the lowest heat requirement.

4.5 Exergy values calculation and visualization

The scripts calculate and visualize the exergy values for exhaust and coolant systems at different RPMs, considering various engine parameters and operating conditions. The coolant mass flows and

exhaust temperatures values for various RPMs and BMEP values and contain the percentages of exergy allocated to exhaust and coolant systems at different RPMs. The scripts determine the closest BMEP index to the required value, prepares arrays to store exergy values for exhaust and coolant systems, and compute exergy values by iterating through RPM values and adjusting for engine displacement and number of cylinders in case the user changes the input parameters for the H2ICE

4.6 Heat Requirement Calculation with and without WHR

The scripts calculate the amount of hydrogen required to provide necessary heat for a reactor system both with and without WHR and evaluate the sufficiency of available exergy from exhaust and coolant systems at different RPM and determine the additional hydrogen needed for the burner. For the no WHR scenario, the scripts retrieve the row with the lowest total heat fluxes, compute the total heat required without WHR by summing relevant heat fluxes (Q_coolant, Q1, Q2), and calculate the mass flow of hydrogen needed to provide the required heat. For the WHR scenario, they extract specific exergy values for exhaust and coolant at the required BMEP across all RPMs and perform sufficiency calculations for various WHR strategies. Then determine the additional hydrogen needed after accounting for WHR and calculate the net required heat with WHR, displaying the required amount of hydrogen or indicating if no additional hydrogen is needed.

4.7 Simplified thermodynamical approach (Li 2023)

The MATLAB script validates the simplified thermodynamic model proposed by Li (2023) for determining heat fluxes and mass flow rates without using a complex reactor model. It begins by initializing necessary variables and an empty table to store results and calculates the dehydrogenation heat flux in kW. It computes the mass flows of H18DBT and H0DBT using stoichiometric relations and dehydrogenation efficiency and calculates the heat flux based on average specific heat capacities. The H2ICE is considered in same manner as in 1D model. Results are filtered based on specified tolerances and stored in the results table. The script then calculates the hydrogen burner mass flow rate required with and without WHR converting values to kg/h. It displays whether additional hydrogen is needed for the process, ensuring the model aligns with set point requirements.

4.8 Reiterated Heat Flux and mass flow Calculations

The script reiterates the calculation of heat fluxes by incorporating the mass flow of the hydrogen burner required to meet heat demands with that are not met with WHR (mass flow required = mass flow of hydrogen for H2ICE + mass flow required for H2 burner). It reiterates mass flows and heat fluxes for the reactor all operating points, identifying the scenario with the lowest total heat flux requirement and displaying the corresponding heat flux values and mass flows.

4.9 Post processing

Finally, the script processes the results to generate the figures, tables to display the results.

4.10 Graphical representation of the developed model

Figure 30 shows the system setup, giving an overview off the relation between the different components. A larger image is given in XX

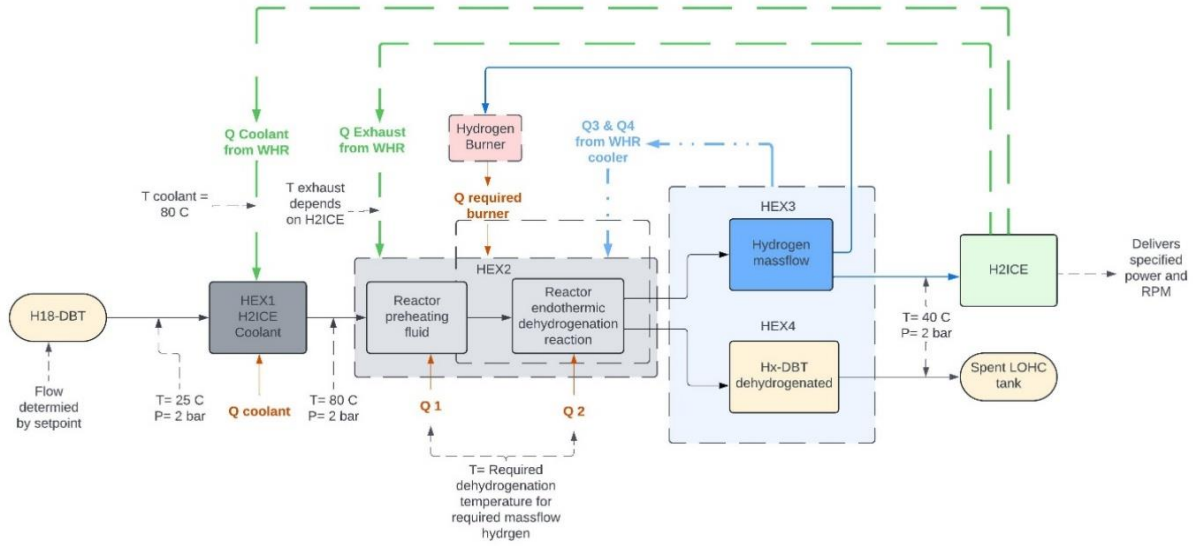

Figure 30 - H2ICE coupled with dehydrogenation reactor system design

4.11 Modelling assumptions

In the relevant chapters the assumptions and why they are valid are discussed, but for clarity sake the main assumptions are also listed below.

- Geometrical scaling of reactor to match H2ICE power, scaling factor used for results is 16 for the DI model
- Modeling assumptions of 1D heterogenous reactor model or simplified thermodynamical model
- Heat available from H2ICE is predominantly RPM dependent
- No LOHC recycling
- Reactor optimization for lowest heat requirement
- No evaporation of LOHC in reactor
- Limited BOP
- No hydrogen or heat buffer
- Minimum allowable dehydrogenation grade is 70%
- the difference between the available hydrogen mass flow from the reactor and the required H2ICE mass flow can be no greater than 15%
- heat exchanger efficiency is 80% and all heat is transferred
- The heat transfer from the wall to the liquid relied solely on the temperature at a specific position, represented through simple heat-transfer coefficients.
- These coefficients, measured in a system without chemical reaction, were a simplification.
- Axial dispersion in the reactor was not considered.
- A high degree of radial dispersion was assumed.

5 Modelling inputs

In the previous chapters the specific components have been reviewed. For clarity the main inputs and component characteristics for the model are described below. These inputs are then used to run the developed MATLAB script given in paragraph 11 in two different iterations, one for each engine type.

5.1 Engine characteristics

In the table below the engine specification from the Zhang (2023) and Wang (2018) papers are listed, italic data is calculated.

Tabel 2

CHARACTERISTIC	ZHANG 2023	WHANG 2018
ENGINE TYPE	Inline 4-cylinder	Inline 4-cylinder
INJECTION TYPE	Direct fuel injection	Port fuel injection
FUEL	H2	H2
BORE AND STROKE	88 mm and 82 mm	90 mm and 90 mm
CYLINDERS	4	4
COMPRESSION RATIO	10:1	9.3
EXHAUST VALVE OPEN	40° BBDC	Not given
EXHAUST VALVE CLOSE	4° ATDC	Not given
INLET VALVE OPEN	6° ATDC	Not given
INLET VALVE CLOSE	40° ABDC	Not given
ENGINE SPEED	1000 rpm – 3500 rpm	1500 rpm – 4000 rpm
INTAKE MODE	Turbocharger and intercooler	Turbocharger and intercooler
DISPLACEMENT	2.0 L	2.290 L
MAXIMUM TORQUE	*222 N·m @ 3000 rpm*	161 N·m @ 3000 rpm
MAXIMUM POWER	*81.45 kW @ 3500 rpm*	59.4 kW @ 4000 rpm

5.2 Heat exchangers

The heat exchangers er not dimensioned and the temperature distribution is not modelled. The heat exchanger efficiency assumed in the model is 80%. The temperature profile within the heat exchanger is not modelled.

Tabel 3

Temperature engine coolant	80 °C
T ambient	25 °C
T Reactor	250 - 320 °C, determined by operating point of system
T preheating (temperature at which DBT enters the reactor)	250 °C
T cooled (temperature to which spent DBT and H2 are cooled)	40 °C

5.3 Reactor

Below the main parameters of the reactor used for the literature are given, the given data is from Peters (2019) and is not scaled to the modelling size, but the geometrical scaling factor that the model uses is given.

Tabel 4

Reactor power	5 kW
Mass heat conductivity [W m^{-1} K^{-1}]	25
Mass heat capacity [J kg^{-1} K^{-1}]	500
Mass	30 kg
Reactor scaling factor	16
Reactor pressure	2 bar
Free reactor volume	6.825E-03 m3
Fraction of active reactor volume	0.8
porosity of the catalyst bed	0.4

6 Results

The results below represent the figures generated by the developed MATLAB script. These figures were used to answer the research questions. These generated results use the components and assumptions described in previous chapters.

6.1 H2ICE: Fuel flow and available heat fluxes

The figures shown in this paragraph are for the Zhang (2023), DFI hydrogen, and Wang (2018) PFI engine models with the same specifications as the studies that described the models. Below, in Figure 31, the required fuel flow was computed using the engine specifications and plotted for BMEP and RPM. A detailed representation of the fuel flow for both engine types as a function of power and RPM is given in paragraph 9.2.

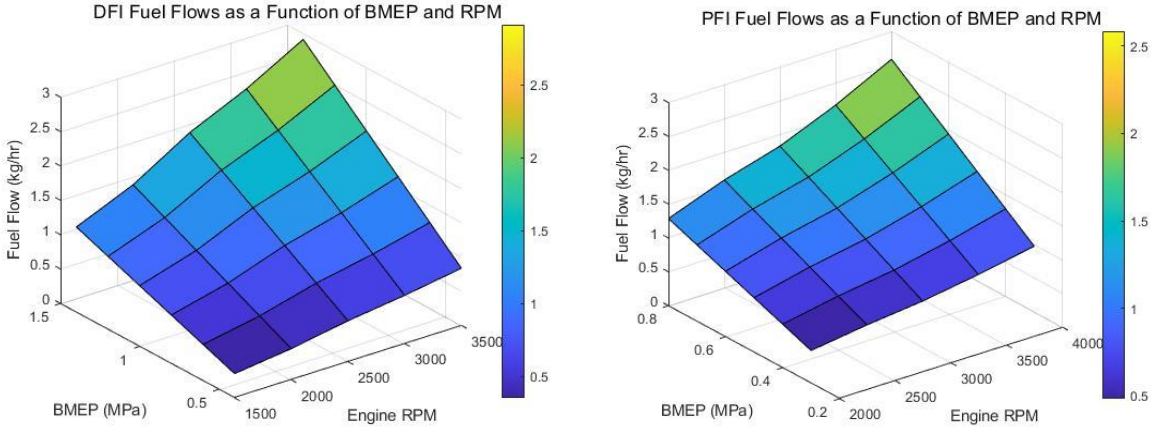

Figure 31. Fuel flows as a function of BMEP and RPM

For all the operating points of the H2ICE, the available coolant, exhaust exergy, exhaust temperature, and coolant mass flows were determined. Figure 32 shows the available energy in the exhaust gases and the coolant as a function of RPM.

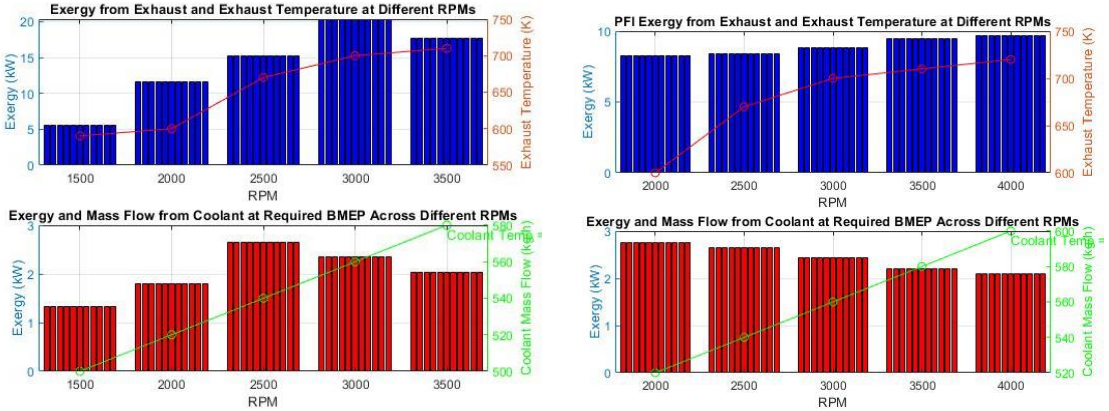

Figure 32. Exhaust exergy, DFI, and PFI for H2ICEs

The dehydrogenation temperature, the exhaust temperature, and the available exhaust energy were then used to calculate the heat flux available from the exhaust, where the heat exchanger efficiency (0.8) is also accounted for. The figure shows the available heat flux for the exhaust. The available

heat flux for the coolant at a cooling temperature of 80 °C is between 0.2 and 0.3 kW for DFI and 0.11 and 0.15 kW for PFI.

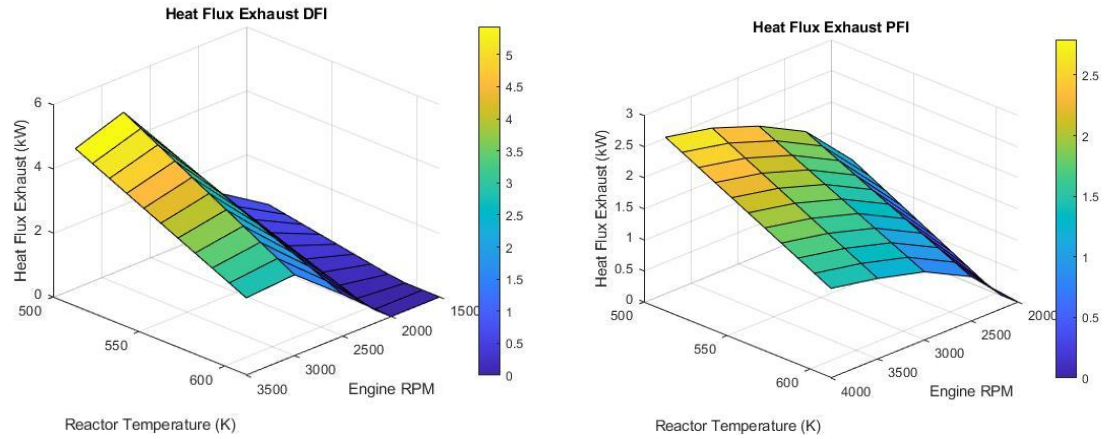

Figure 33. Heat fluxes as a function of the RPM and the required reactor temperature

For the Wang model, the stationary RPM of 1,500 RPM was excluded. This was done for modeling simplicity as the matrices would dimensionally be the same as the Zhang model. Given the lower temperature between exhaust temperatures, the heat flux at this point is near zero.

The difference between the exergy available for the DI and PFI models is due to the higher exhaust temperatures of the DI model, as the percentage of exergy available in the exhaust is lower for the DI model. For the rest of the results, reference will be made only to the DFI model figures for the sake of clarity. The PFI figures are attached in Appendix 9.3.

6.2 Results from the kinetic model

After reviewing the initial results, it was found that for some of the reactor conditions, the hydrogen mass flow seemed overly optimistic. A clear indication of this was the fact that the reactor would deliver more power than the entering LOHC could hold at full hydrogenation, for instance, at the operating points LHSV = 1 and T = 613. Since the script optimized for the lowest heat requirements at the power level required, these operating points with unrealistically low H18-DBT mass flows corrupted all the results.

```
Enter the minimum acceptable dehydrogenation grade (<=1): 0.7
```

Mass Flow H18DBT (kg/hr)	LHSV (1/hr)	Temperature (K)	DFI_BTE_BMEP index	m_dot_H2 (kg/hr)	P_reactor (kW)
30.853	1	513	1	0.84444	28.148
18.032	1	523	1	0.84444	28.148
10.754	1	533	1	0.84444	28.148
6.5363	1	543	1	0.84444	28.148
4.0451	1	553	1	0.84444	28.148
2.5464	1	563	1	0.84444	28.148
1.6291	1	573	1	0.84444	28.148
1.0583	1	583	1	0.84444	28.148
0.69759	1	593	1	0.84444	28.148
0.46622	1	603	1	0.84444	28.148
0.31571	1	613	1	0.84444	28.148
61.705	2	513	1	0.84444	28.148
36.064	2	523	1	0.84444	28.148
21.507	2	533	1	0.84444	28.148

Figure 34. Mass flows based on analytical solution of 1D heterogeneous model by Peters et al. (2019)

To eliminate the possibility of a programming error, a separate, simple validation script (see Appendix 9.4) was made to check the relationship described in Figure 24 (shown again below for convenience) . The results of the analytical solution were compared to the validated results in Figure 9B from the study of Peters et al. (2019) represented below in Figure 35. The expectation was that the results of the validation experiment would resemble the analytical result, but this was not the case.

$$\dot{n}_{H_2} = 9 \cdot \eta_{LOHC} \cdot \dot{n}_{LOHC} \cdot \rho_{Kat} \cdot \tau \cdot k_0 \cdot \exp\left(-\frac{E_A}{R \cdot T_s}\right) \cdot (3120 \cdot \eta_{LOHC})^{1.98}$$

Herein:

$$\tau = \frac{3600}{LHSV \cdot 500}$$

$$LHSV = \frac{\dot{V}_{LOHC}}{V_{reactor} \cdot \varepsilon \cdot F_{RV}}$$

Figure 24 – Mass flow relation for PBR as a function of LHSV and temperature (Preuster et al., 2018)

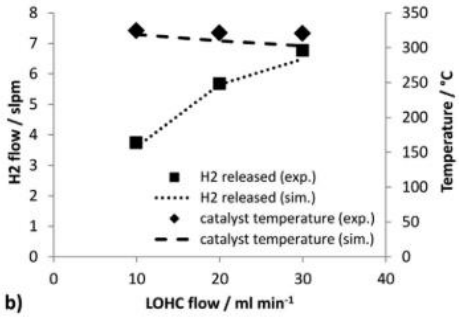

Figure 35. Experimental results compared to the model of Peters (Peters, 2019)

The discrepancy is not immediately evident due to a (inconvenient) change of units, but Figure 35 depicts the relationship between the LOHC flow rate and the resulting hydrogen flow rate, showing an expected hydrogen flow rate of approximately seven standard liters per minute (SLPM) at a catalyst temperature of around 300 °C, which is about 0.037 kg/hr H2 at 1.89 kg/h LOHC flow at LHSV of 0.8 and 590 K. However, the script's output using the analytical formula significantly deviated from this expected value, indicating a hydrogen flow rate of 0.84 kg/hr H2 under similar conditions from a 0.7 kg/hr LOHC flow.

The substantial deviation in results indicates a potential underlying issue: the hydrogen flow relationship might not be calculated correctly by the analytical solution as described in Figure 24. This discrepancy suggests that the empirical relationships and assumptions used to derive the analytical solution in Peters (2019) may not accurately reflect the experimental conditions or the actual behavior of the system. Upon finding this, an email (and later, a follow-up email) addressing the issue was sent to P. Preuster. In the 12 weeks before the submission of this paper, no response was received.

This posed a challenge in utilizing the 1D heterogeneous reactor model to address the research questions of the present study. Thus, the analytical approach was replaced by using the operating points from Figure 25 . Assuming this figure does give the correct relationships regarding dehydrogenation, LHSV, and power output in kW per liter.

To determine the operating point in kW per liter, the mass flow of the LOHC was determined based on the LHSV. From the reactor power output, the reactor's hydrogen mass flow was calculated considering the energy density of hydrogen (33.33 kWh per kg). In other words, lookup tables (Tabel 5 and Tabel 6) based on Figure 25 (shown again below for reference) replaced the analytical formula to establish a correct link between the operating point of the reactor based on power output and dehydrogenation grade as a function of temperature and LHSV..

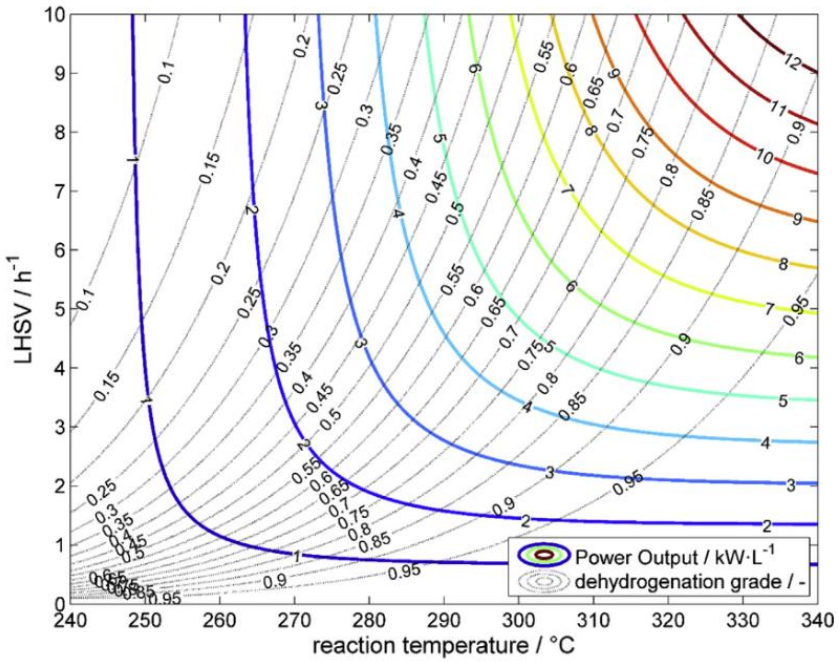

Figure 36 – Power output and dehydrogenation grade as a function of temp and LHSV for DBT (Peters et al., 2019)

Tabel 5 – Power output look up table analytical model

	513	523	533	543	553	563	573	583	593	603	613
10	0	1,1	3,28	5,46	7,64	9,82	12	12,2	12,4	12,6	12,8
9	0	1	3	5	7	9	11	11,2	11,4	11,6	11,8
8	0	0,9	2,72	4,54	6,36	8,18	10	10,2	10,4	10,6	10,8
7	0	0,8	2,44	4,08	5,72	7,36	9	9,2	9,4	9,6	9,8
6	0	0,7	2,16	3,62	5,08	6,54	8	8,2	8,4	8,6	8,8
5	0	0,6	1,88	3,16	4,44	5,72	7	7,2	7,4	7,6	7,8
4	0	0,5	1,6	2,7	3,8	4,9	6	6,2	6,4	6,6	6,8
3	0	0,4	1,32	2,24	3,16	4,08	5	5,2	5,4	5,6	5,8
2	0	0,3	1,04	1,78	2,52	3,26	4	4,2	4,4	4,6	4,8
1	0	0,2	0,76	1,32	1,88	2,44	3	3,2	3,4	3,6	3,8
0	0	0,1	0,48	0,86	1,24	1,62	2	2,2	2,4	2,6	2,8

Tabel 6 – dehydrogenation grade lookup table

	513	523	533	543	553	563	573	583	593	603	613
10	0	0,05	0,125	0,18	0,275	0,375	0,5	0,6	0,725	0,825	0,875
9	0	0,075	0,14	0,2	0,3	0,4	0,525	0,64	0,75	0,84	0,9
8	0	0,09	0,15	0,225	0,32	0,425	0,55	0,675	0,775	0,85	0,91
7	0	0,11	0,16	0,25	0,35	0,46	0,6	0,71	0,8	0,875	0,925
6	0	0,125	0,2	0,275	0,4	0,51	0,65	0,75	0,85	0,91	0,94
5	0,1	0,15	0,25	0,325	0,45	0,575	0,7	0,8	0,875	0,925	0,95
4	0,125	0,175	0,25	0,375	0,5	0,625	0,75	0,85	0,9	0,95	0,96
3	0,15	0,225	0,325	0,45	0,6	0,7	0,825	0,875	0,93	0,94	0,975
2	0,2	0,3	0,45	0,575	0,7	0,8	0,9	0,94	0,96	0,98	0,99
1	0,35	0,5	0,65	0,75	0,85	0,92	0,95	1	1	1	1
0	1	1	1	1	1	1	1	1	1	1	1

Using the method described above the resulting LOHC and hydrogen mass flow from the model are shown in the right figure in Figure 37 below. The figure on the left hand is the thermodynamical model for reference. The accompanying hydrogen flow for both models is shown in Figure 38.

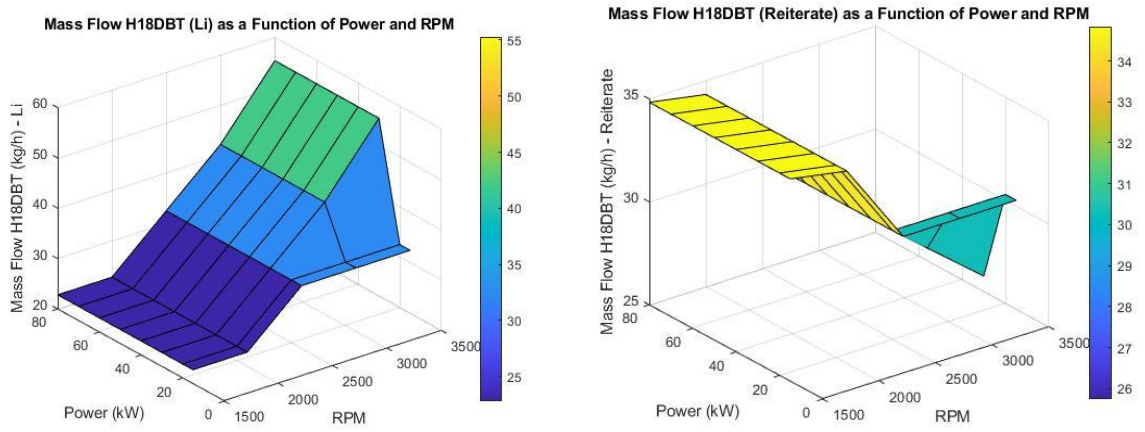

Figure 37. LOHC mass flow as a function of RPM and power

The left image in Figure 37 is the mass flow H18DBT (Li) as a function of power and RPM, showing a positive correlation where mass flow increases with both power and RPM. The color gradient from blue to green indicates an increase in mass flow from approximately 25 kg/h to 55 kg/h. The right image presents the mass flow H18DBT (Reiterate) based on the heterogeneous models as a function of power and RPM, demonstrating a different relationship. Here, the mass flow starts around 35 kg/h and decreases as power and RPM increase. The color gradient from yellow to blue signifies a decrease in mass flow from about 34 kg/h to 26 kg/h. These contrasting patterns highlight different dependencies of mass flow on power and RPM and are possibly explained by the optimistic heat requirement of heterogeneous reactor model. As for equal hydrogen mass flow outputs, as shown in Figure 38. The LOHC flow shown in Figure 37 is significantly less (nearly half) and shows different dependency on RPM.

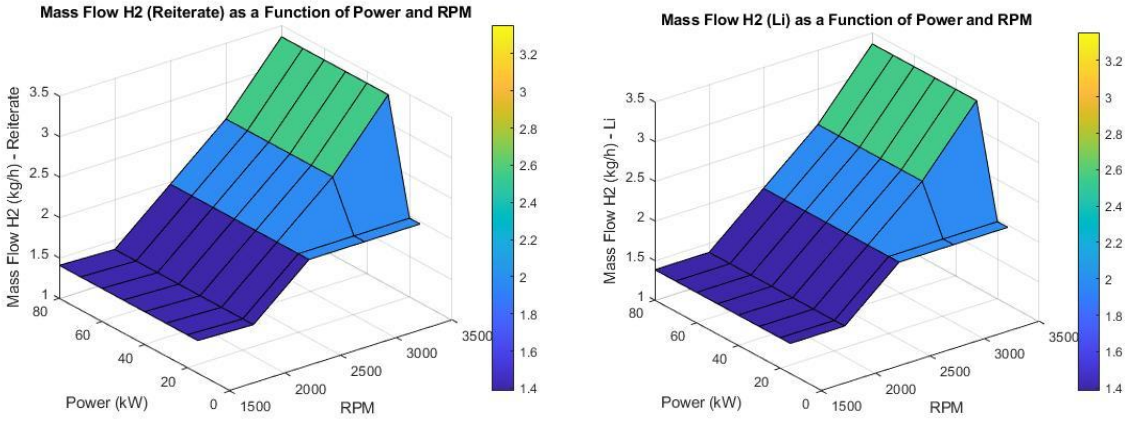

Figure 38. H2 mass flow as a function of RPM and power

Intuitively the results from Figure 37 based on Figure 36 display do display the main relations of the analytical model of Figure 24. In the analytical formula the term $\exp(-\frac{EA}{R*Ts})$ describes the fraction of molecules with sufficient energy to react. At lower temperatures, this fraction decreases because fewer molecules have the necessary energy to overcome Ea. Consequently, the reaction rate drops as Ts decreases. On the other hand, the residence time, τ, is a measure of how long a reactant spends inside a reactor, which influences how complete a reaction can be before the reactants exit. When τ is long, reactants have more time to react, potentially leading to higher conversion rates. The relationship between τ and LHSV shows that as LHSV increases (indicating higher liquid flow rate), the residence time τ decreases. This shorter residence time means the reactants pass through the reactor more quickly, reducing the time available for the reaction to occur. Thus, both temperature and residence time work together to determine the hydrogen production rate , higher temperatures increase the likelihood that molecules will react, while longer residence times give reactants more time to complete their reactions.

The model based on the lookup table shows that required hydrogen flow is met with decreasing H18-DBT mass flow for increasing RPM. Increasing RPM increases Ts that lowers required H18-DBT flow since the power output per liter of the reactor increases for higher temperatures. Higher RPM does also influence the other operating point determinants as the higher required hydrogen mass flow at available temperature determines the possible LHSV at the minimum required dehydrogenation grade. 1 setpoint is chosen for the set of possible solutions on the lowest neat heat requirement. One would expect a higher sensitivity to tau due to the scaling factor $\text{tau} = \left(\frac{3600}{500}\right) * \text{LHSV} = \text{scalingfactor} * \text{LHSV}$ and the negative exponential term (for Ts) will always be between 0 and 1, further the analytical relation is linearly dependent on the mass flow. These relations are also found in the results of the operating conditions of the reactor as function of power and RPM as shown in Figure 39.

6.3 Coupling

The objective was to analyze the system properties, requirements, and feasibility of integrating the H2ICE with the reactor for LOHC dehydrogenation. Ships must perform many tasks that have varying power and rpm demands, and the effect of varying propulsion power on mass and energy balances can give insight into the requirements for a reactor and the utilization of WHR in these operating points. The developed model selected operating points based on the following requirements:

- the required fuel flow of H2ICE being less than the delivered H2 flow of the reactor, including the hydrogen burner mass flow required, but not greater than a preset margin.
- the set minimal acceptable degree of dehydrogenation; and
- the operating point that requires the least heat for dehydrogenation as selected from the available operating points.

This strategy allows for maximal effectivity of the WHR, as the enthalpy used for dehydrogenation is detrimental to system efficiency. The resulting reactor set points as a function of H2ICE power and RPM are displayed in Figure 39 below.

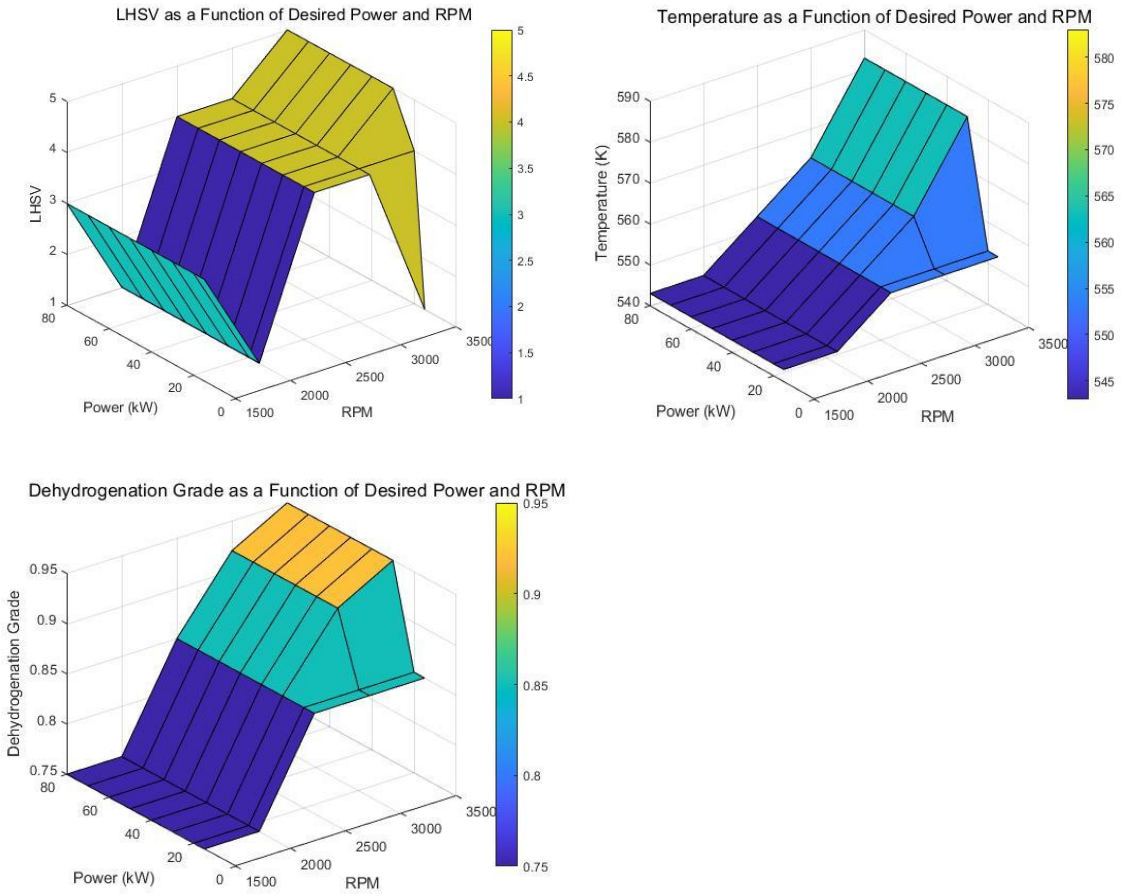

Figure 39. Reactor conditions in the DFI model

Using the developed model, we demonstrated that the reactor could provide the necessary hydrogen flow for the PFI and DFI H2ICE within 12.5% of the required operating point. The 12.5% variance between the required and delivered hydrogen flow is due more to the model setup than to the

reactor's actual capabilities. Recalculating with a finer mesh could reduce this difference, but this seems arbitrary given the restrictions described in the reactor control section, where the setpoint would likely be a time average or a predicted time average.

The model allowed for further examination of the coupling constraints by adjusting various input parameters in the script. At all operating points, the 1D reactor model generated sufficient hydrogen flow. Dehydrogenation grades did not exceed 70% at low RPMs, while higher RPMs in the H2ICE power band yielded dehydrogenation grades between 85% and 95%, which are acceptable. At lower RPMs, a lower dehydrogenation grade is explained by the lower heat flux available. Thus, the reactor model chose a lower dehydrogenation grade to fulfill hydrogen demand at the minimum total heat requirement. An advantage of these higher dehydrogenation grades is the elimination of the need for recycling flows. The calculations assumed no recycling of partially dehydrogenated DBT, but the mass flows were adjusted for the dehydrogenation grade through the relationship with temperature and LHSV.

6.4 Heat fluxes

The heat fluxes were determined according to the equations and approach described in paragraph 3.7.1, and the results of the heat fluxes are shown in Figure 40. The influence of the reactor models is also visible, as the shape of the heat flux requirement naturally is dependent on the mass flow of H18-DBT and the reactor operating conditions. The heat exchanger efficiencies were set at 80%. A topic of discussion in the literature is whether one must account for the evaporation of LOHC. For operating pressures above 2 bar in this reactor system, the pressure is above vapor pressure and the evaporation of the LOHC is not accounted for in this study.

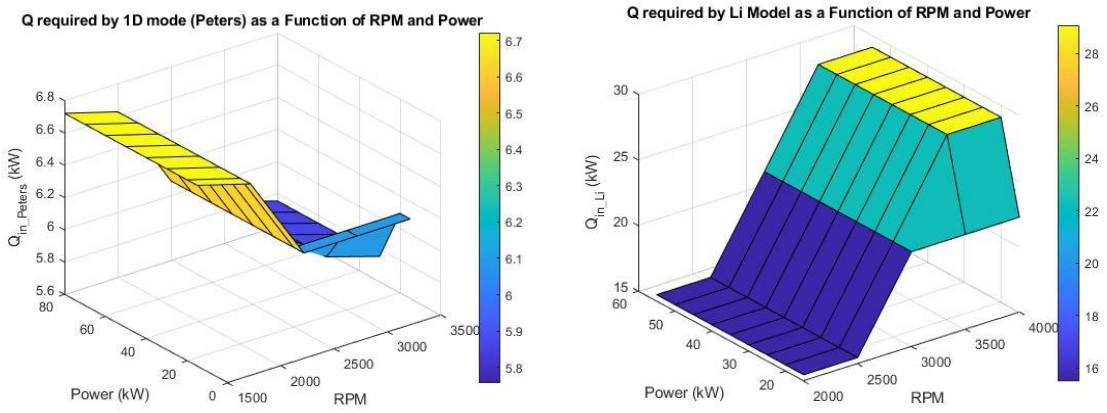

Figure 40. Heat fluxes required for dehydrogenation for both reactor models

6.5 WHR: Hydrogen burner mass flows

To address the research question of whether the dehydrogenation of H2ICE can be performed with the heat supplied by the H2ICE at multiple load factors, the calculated hydrogen burner mass flows are a useful determinant. This approach is effective because the required mass flow for the burner was calculated for each operating point of the system based on the available heat flux from exhaust, coolant, and WHR from spent LOHC and H2; the required heat fluxes for dehydrogenation and preheating; and heat exchange efficiencies. If there is a shortage of heat for dehydrogenation, it is supplemented by the burner. Thus, if there is no shortage or even a surplus of heat, the burner mass flow will be zero, indicating full WHR support.

Figure 41 illustrates the hydrogen burner mass flows for two different reactor models with equal H2ICE configurations: the Li (2023) model and the Peters (2019) 1D model, both coupled with the DI-H2ICE with and without WHR. These plots show the hydrogen burner mass flow and clearly indicate whether WHR can deliver sufficient heat to support the dehydrogenation of H18-DBT.

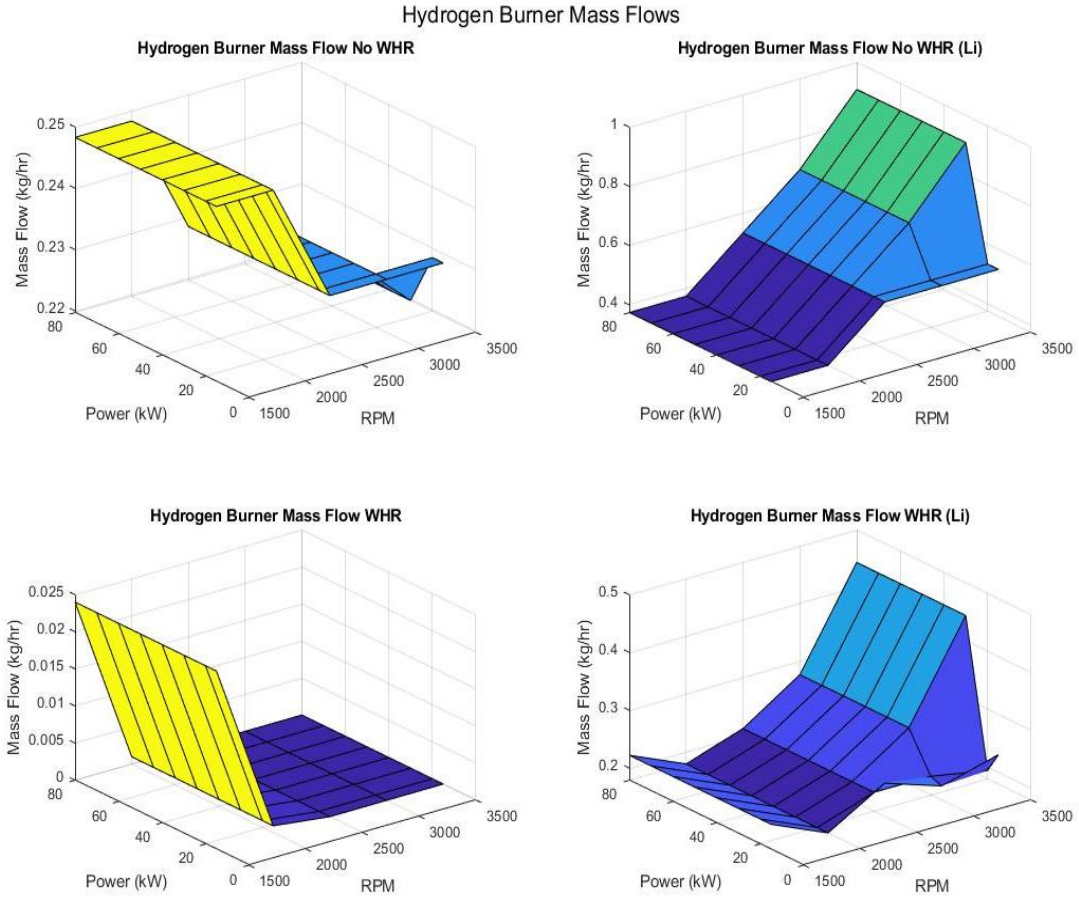

Figure 41. Hydrogen burner mass flows for Li (2023) and Peters (2019) reactor models

Figure 41 illustrates that for the simplified thermodynamic model, most operating points require some added heat from the burner. However, at 2,000 RPM across all power levels, the requirement is relatively low (0.15 kg/hr) – about 10% of the required fuel flow for the H2ICE at that operating point. The WHR for the Li reactor model results in 40% to 60% less hydrogen being combusted in the

hydrogen burner within the operating range, yielding savings in the 2,000 to 3,000 RPM area. Since 1 kg of H2 contains approximately 33.33 kWh of energy, this translates to a power savings of 15.5 kW at maximum power, increasing efficiency by 18.75%. Although WHR does not fully sustain dehydrogenation for the Li reactor model, its integration is beneficial.

For the 1D model from Peters with WHR, a more optimistic scenario is presented. At above 2,500 RPM, sufficient heat is available to sustain the dehydrogenation reaction. Interestingly, without WHR, the hydrogen burner mass flow does not decrease. This is due to the heat requirement of the 1D model, which necessitates higher LHSV, higher dehydrogenation percentages, and higher temperatures, as shown in Figure 38.

6.6 Efficiencies

The energy efficiency increase due to WHR for PEMFC was approximately 38% (Geiling et al. 2021, Li et al., 2023). WHR for the SOFC was performed with direct heat transfer, and the energy increase was approximately 27%. In a SOFC coupled with heat cycles, net electrical efficiencies may surpass 70% (Preuster et al., 2019). Without WHR, 50–65% electrical efficiencies derived from LHV can be expected (Mestemaker et al., 2019) – an up to 20% increase. One study showed that HICE had achieved a BTE of 45% and was expected to reach 51% through combustion chamber optimization and other WHR measures. The total hydrogen fuel thermal efficiency limit is theoretically about 59% (Wang et al., 2019. Zhang et al., 2023).

Currently, a significant amount of fuel energy is wasted in the exhaust gas and cooling system, leaving only a fraction utilized in the form of output work. The modeling results in this study show that the increase of H2ICE systems with coupling to dehydrogenation can (theoretically) be up to 18.75% for the simple thermodynamical model. These efficiency gains bring the H2ICE-coupled system to comparable efficiencies as the PEMFC and SOFC alternatives. For the 1D model, the results are more optimistic, and full dehydrogenation support can be achieved for most RPM and power levels. This would increase system efficiency by about 30%.

There are reservations regarding the certainty of the magnitude of the efficiency gains. The model was able to prove that coupling a reactor with an H2ICE including WHR is feasible, and it also was able to quantify the available heat fluxes from WHR on the efficiencies. This should allow a system-level efficiency gain of between 0 and 6% to be contributed to the coupling for the PFI-coupled system, where the main restriction is its relatively low exhaust temperatures relative to H18-DBT dehydrogenation temperatures. Other LOHCs with lower dehydrogenation temperatures could yield higher gains due to the relatively large amount of energy available. For the DI model, system-level efficiency gains contributed to the coupling of between 0% and 9% of power (kW based on LHV of H2) due to higher exhaust temperatures. In addition, for the DI case, the utilization of available energy was limited by the dehydrogenation temperature. When comparing the H2ICE systems including the gains from coupling and WHR efficiencies as shown in the left figure of Figure 42 can be expected. Concluding that coupled systems with WHR have comparable efficiencies to SOFC and PEMFC and that the DI H2ICE is in the higher end of the conventional ICE efficiency configuration.

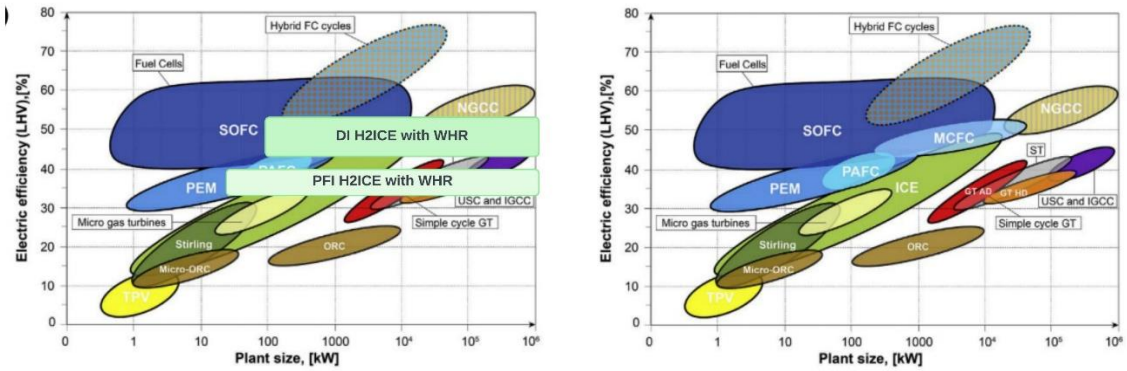

Figure 42. Comparison of the efficiency of propulsion systems (left image includes H2ICE). The image on the right is from (Kadar J. et al., 2024)

7 Conclusion

The objective of this research was to determine the system-level efficiency and exergy, coupling feasibility with dehydrogenation reactors, and WHR effectivity of PEMFC, SOFC, and H2ICE systems with coupled dehydrogenation of H18-DBT for different load factors. To develop this understanding of H18-DBT, insights into the heat balance and mass and energy/exergy balances were developed.

The literature review findings strongly supported DBT as a candidate for maritime fuels due to its ability to meet hydrogen storage requirements and effective densities, accounting for factors like packing and dehydrogenation losses. Minimizing dehydrogenation losses through WHR enhances storage density and efficiency, increasing DBT's competitiveness with other hydrogen carriers. DBT offers advantages such as a high TRL, low flammability, low toxicity, and ease of handling. However, challenges related to viscosity and buffer tank requirements must be considered. Despite environmental hazards, DBT's suitability for fossil fuel infrastructure at ambient conditions makes it a viable choice for maritime applications. The literature study evaluated the efficiency of PEMFC, SOFC, and H2ICE systems for coupled dehydrogenation operation with WHR. A literature study was performed to assess the PEMFC and SOFC systems. A gap exists in the literature regarding DI and PFI H2ICE coupling with dehydrogenation reactors and the effectiveness of integrating WHR from H2ICE exhaust and coolant to support a dehydrogenation reactor.

The literature study reviewed several WHR strategies and identified feasible combinations for PEMFCs and SOFCs. In the case of SOFCs, using high-temperature flux gases was feasible and able to supply the required heat. For the PEMFCs, due to the low temperature, only the integration of the PEMFC cooling circuit was feasible. For H2ICEs, the developed model confirmed the feasibility of using engine coolant to preheat the H18-DBT and using exhaust exergy depending on the operating point of the system and the selected reactor and engine model. To address the insufficient heat available, hydrogen combustion was considered a viable option and integrated into the system model, considering the effect on the mass and energy balances.

PEMFC and SOFC systems are well addressed in the literature, and a literature review is presented. The literature has found that PEMFC energy and energy efficiencies are overstated in simplified thermal models, as the efficiency of fuel cell systems, particularly PEMFCs, highly depends on factors like the operating temperature, current density, and system design. These factors significantly impact the overall efficiency of systems, and the conclusions in the WHR literature seem too optimistic. WHR is insufficient to drive dehydrogenation reactions for PEMFCs, but using WHR for preheating increases system efficiency. While PEMFC coupling feasibility is confirmed and dynamic, it faces challenges related to carbon purification.

The literature provided a comprehensive understanding of the mass and energy balances in the case of SOFCs and the behavior of these systems under load changes. The dynamic behavior of coupled SOFCs and dehydrogenation is promising, demonstrating stability under load changes. With comprehensive WHR integration, SOFCs provide sufficient heat to sustain dehydrogenation while avoiding critical component conditions.

A review of reactor types and modeling methods was created to select the reactor model and design for this study. Subsequently, the 1D heterogeneous model was selected as it suits the modeling purpose best. However, this study found that this model was too optimistic with regard to the heat requirement for the resulting hydrogen flow. Therefore, a reference model based on thermodynamic principles was integrated for comparison. A multiphase CFD model would be a powerful problem-solver for reactor conditions but is unavailable in the literature for H18-DBT.

H2ICEs are praised for their ability to significantly reduce CO2 emissions, as hydrogen combustion produces no direct CO2. However, small amounts can result from burning lubricating oil. Unlike fossil fuels, hydrogen combustion avoids SOx and particulate matter, though NOx remains a concern due to its high combustion temperatures. Researchers aim to optimize combustion and develop aftertreatment systems to minimize NOx, making H2ICEs a near-zero-emission technology. Key strategies include running slightly leaner than the stoichiometric ratio and employing delayed injection timing to lower combustion temperatures. These techniques reduce thermal NOx formation while maintaining engine efficiency and power. However, if scrubber systems need to be installed, these systems could take up usable heat from the exhaust and possibly make WHR and dehydrogenation from exhaust gasses more problematic.

To fill the gap in the literature on H2ICE and dehydrogenation reactors with and without WHR, a system model was developed in the MATLAB environment for two engine types (DI and PFI) and two reactor models (heterogenous and thermodynamical). The scripts analyze reactor performance, engine performance, WHR strategies, mass balances, and energy balances in H2ICEs and dehydrogenation systems. These scripts calculate power output, fuel flows, and heat fluxes across all operating conditions of an H2ICE. The script also determines reactor conditions by scaling the reactor to fit the H2ICE model and adjusting parameters such as temperature and residence time (LHSV). Heat fluxes were computed to identify the optimal conditions for minimizing heat requirements. The sufficiency of available WHR energy was determined, and if insufficient heat was available, the amount of hydrogen required by the hydrogen burner was quantified. If added heat was required, the operating point of the reactor was altered, and the model iteratively refined the system to identify the optimal heat flux scenario and, thus, the operating point. Finally, the system's performance was quantified.

Assumptions were made of a minimum allowable dehydrogenation grade of 70%, an 80% HEX efficiency, geometric scaling of the reactor, heat available for H2ICE being predominantly RPM-dependent, and perfect heat transfer. The results of the heterogenous model show that coupling H2ICE and dehydrogenation is feasible and that most of the operating points of the reactor conditions allow for dehydrogenation above 85% under the acceptable LHSV and temperatures, even if the required hydrogen mass flow for the hydrogen burner supplies insufficient heat from WHR. For the thermodynamical model, realistic reactor conditions could supply the required hydrogen mass flow for the H2ICE. The results, thus, show that the reactor design can support a 5 kW SOFC and a 5 kW H2ICE with varying levels of heat integration.

Comparing the results of the different injection types on the H2ICE, the DI-H2ICE, as expected, offers higher power density and efficiency than PFI, but the results show that both technologies benefit from WHR integration in the reactor coupling. The available heat fluxes through the WHR of exhaust exergy and coolant exergy depend on available exergy and EGT at the operating point of the H2ICE and at the required reactor temperature at the set point to sustain the hydrogen mass flow required by the H2ICE. The relatively lower EGT temperatures in the PFI limit the utilization of exhaust exergy. The results indicate that WHR integration can supply part of the heat required for dehydrogenation, especially at higher RPMs.

For the DI engine, the detailed heat balance showed that for the thermodynamic model, most operating points required some additional heat from the burner. At 2,000 RPM, the burner requirement was low (0.15 kg/hr) – about 10% to 25% of the required fuel flow by the H2ICE, depending on the load. WHR integration in the reactor coupling for the Li reactor model resulted in 40% to 60% less hydrogen being combusted in the burner – an increase in efficiency of 18.75%. WHR integration, although beneficial, was insufficient to fully sustain dehydrogenation. For the 1D model by Peters, the results were more promising. Above 2,500 RPM, sufficient heat was available to

sustain the dehydrogenation reaction. Without WHR, the hydrogen burner mass flow change was less than expected due to the optimistic heat requirements of the 1D model at higher LHSV, dehydrogenation percentages, and temperatures. However, reservations remain regarding the 1D model's analytical model. The available heat flux for the exhaust was, at a maximum, 5 kW at 3,000 RPM and a reactor temperature of 530 K. This is around 6% of the maximum power delivered at that RPM.

For the PFI injection model and the thermodynamic model, most operating points required some additional heat from the burner. WHR integration, although beneficial, was insufficient to fully sustain dehydrogenation. For the 1D model by Peters above 2,500 RPM, sufficient heat was available to sustain the dehydrogenation reaction. However, the same reservations with the 1D model apply to this case. Due to the lower EGT in the PFI, despite higher available energy, the maximum heat flux exhaust was lower. A heat flux of 2.7 kW at 4,000 RPM and a reactor temperature of 530 K was around 5% of the maximum power at that RPM.

The results are reported as a function of RPM, as the heat available in the exhaust is assumed to be predominantly RPM-dependent, convenient for modeling, sufficiently accurate for the goal of this research, and accepted in the literature. Considering the load variation of the EGT would create more fluctuation in the results but would be expected to increase the effectiveness of the WHR. The mass flows from the reactor required by the H2ICE were determined using the load and RPM. Thus, the required heat was estimated correctly, but the available heat was underestimated. This means that for higher loads, there is more energy and a higher EGT, and thus, a higher available heat flux.

The study investigated the energy efficiency improvements due to WHR in various hydrogen-powered systems. For PEMFC, WHR led to a 38% increase in energy efficiency (Geiling et al., 2021; Li et al., 2023). For SOFC, direct heat transfer through WHR increased exergy by 27%, and coupling with heat cycles could push electrical efficiencies beyond 70%, compared to 50–65% without WHR (Preuster et al., 2019; Mestemaker et al., 2019).

For H2ICEs, a base BTE of 45% has been achieved, which could potentially increase to 51% through combustion chamber optimization and WHR measures. The theoretical hydrogen fuel thermal efficiency limit is around 59% (Wang et al., 2019; Zhang et al., 2023). Current losses through exhaust and cooling systems leave much of the fuel energy unutilized. MATLAB modeling suggests that H2ICE systems coupled with dehydrogenation could increase efficiency by up to 18.75%. More optimistic 1D models indicate a 30% efficiency boost with full dehydrogenation support. Models show that WHR coupling of exhaust and coolant with H2ICEs is feasible, contributing to 0–6% system-level efficiency gains for DI systems and 0–9% for PFI systems. Gains are limited by the low exhaust temperatures compared to dehydrogenation temperatures, but using LOHCs with lower dehydrogenation temperatures could yield higher efficiency improvements. These results compare H2ICE systems favorably with PEMFC and SOFC technologies. In conclusion, while WHR integration for H2ICEs is beneficial, it is not sufficient to sustain dehydrogenation at all operating points for H18-DBT. The efficiency gain of integrating the system with WHR is proven in the system model.

Regarding reactor control, existing literature has concluded that a combination of pressure and temperature control is advised to control the supplied hydrogen for a certain LOHC mass for 10 to 30 minutes. LOHC mass flow control is necessary to ensure that power levels can be sustained over longer periods. This study did not implement a control strategy as it focused on the mass and energy balances of the possible operating point, but integrating a control strategy would aid in the understanding of transient system behavior and operational profile limitations.

To allow proper reactor control despite varying EGT and to prevent degradation of H18-DBT due to hot spots and because of adequate but imperfect temporal matching of the heat requirement, a TES is advised. A TES was not integrated into the model as it does not aid in reviewing the mass and energy balances of the different operating points, but it is expected to aid in determining transient behavior and operational profiles, which were outside the scope of this study.

8 Suggestions for future research

8.1 Combined configurations

This study was limited to simple power configurations. However, using combinations of power converters could lead to more dynamic capability and influence the heat balance of a system. The combinations are endless, according to the literature.

The obvious integration of a battery pack in the electrical system would allow for load balancing while requiring less flow from the SOFC and reactor. For instance, parametric and exergy analyses of a PEMFC and SOFC hybrid system (Wu et al., 2018) showed that the proposed hybrid system could achieve a high energy conversion efficiency of approximately 64% and an exergy efficiency of 61%. The higher energy efficiency should benefit dehydrogenation coupling.

SOFC and ICE hybrid systems have efficiency gains in verified 0-D SOFC models. Engine experiments and a validated AOG-NG mean engine model have shown an up to 8% efficiency improvement for these systems (Sapra et al., 2021). The advantage for maritime systems is that the ICE could take up significant and sudden load changes. It would be interesting to couple the SOFC part to the reactor and allow the ICE to step in for load changes from a buffer or also be coupled to the reactor.

8.2 More detailed combined reactor HEX and ICE modeling with a control strategy

Aspen or another suitable software package could be used to analyze heat exchanger dimensions and properties to obtain more accurate efficiency and simulate heat distribution. Test data from an engine manufacturer or a detailed engine model could be incorporated to generate a refined 3D map of the exhaust gas temperature and mass flows and capture more variations in available heat across different BMEP levels. This approach would help identify potential issues, such as hot spots, that could lead to LOHC degradation. Integrating the proposed control strategies would provide deeper insights into the required buffer sizes and the transient response of the reactor system with WHR.

8.3 Comparing engine experiments to models

This study specifically chose to use experimental data for two engine types. However, for future design purposes, using a combustion of H2ICE modeling method would be convenient, as it would allow for an exploration of more power configurations considering the scaling of the H2ICE. The design parameters of an engine designed for maritime use could also be considered.

8.4 Completeness of the system design

The process design is crucial due to additional requirements like hydrogen purification that impact the limited space and weight of mobile systems. While this study focused on examining the process design requirements, it did not address the weight and space constraints of the proposed systems. Critical components were analyzed for system comparison; however, more detailed and precise modeling of the BOP is needed. This study primarily addressed efficiency without considering economic aspects. Therefore, a techno-economic evaluation of LOHC chains with WHR strategies is recommended for future research.

9 Appendices

9.1 Block scheme of model

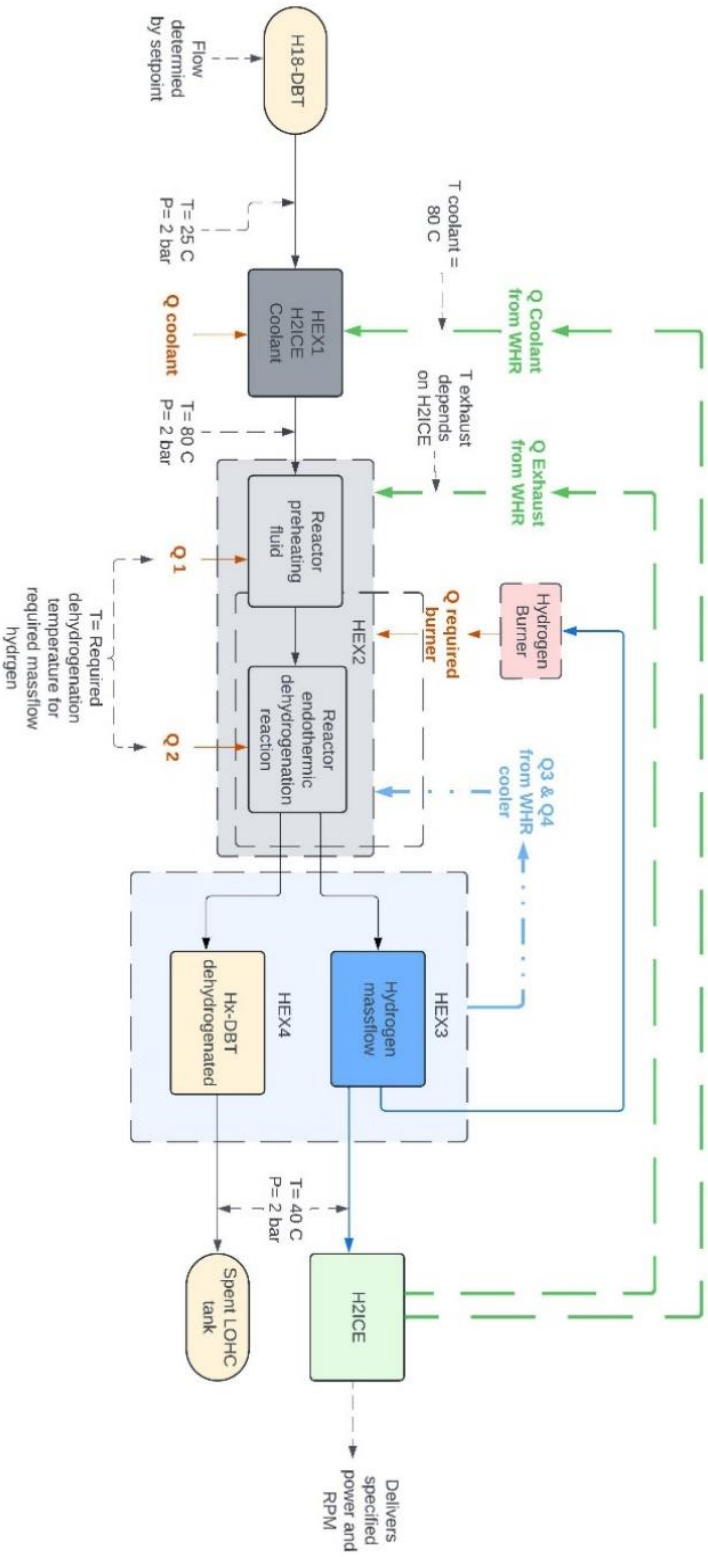

9.2 Fuel flows detailed

RPM	BMEP (MPa)	DFI P (kW)	DFI H2(kg/hr)	PFI P (kW)	PFI H2(kg/hr)
1500	0.40	9.97	0.35	9.97	0.42
1500	0.60	14.96	0.53	14.96	0.63
1500	0.80	19.95	0.71	19.95	0.84
1500	1.00	24.94	0.88	24.94	1.05
1500	1.20	29.92	1.06	29.92	1.26
1500	1.40	34.91	1.24	34.91	1.47
2000	0.40	13.30	0.45	13.30	0.55
2000	0.60	19.95	0.68	19.95	0.83
2000	0.80	26.60	0.91	26.60	1.11
2000	1.00	33.25	1.13	33.25	1.39
2000	1.20	39.90	1.36	39.90	1.66
2000	1.40	46.55	1.59	46.55	1.94
2500	0.40	16.62	0.60	16.62	0.66
2500	0.60	24.94	0.89	24.94	1.00
2500	0.80	33.25	1.19	33.25	1.33
2500	1.00	41.56	1.49	41.56	1.66
2500	1.20	49.87	1.79	49.87	1.99
2500	1.40	58.19	2.08	58.19	2.32
3000	0.40	19.95	0.70	19.95	0.81
3000	0.60	29.92	1.05	29.92	1.22
3000	0.80	39.90	1.40	39.90	1.62
3000	1.00	49.87	1.75	49.87	2.03
3000	1.20	59.85	2.11	59.85	2.43
3000	1.40	69.82	2.46	69.82	2.84
3500	0.40	23.27	0.83	23.27	0.99
3500	0.60	34.91	1.25	34.91	1.48
3500	0.80	46.55	1.66	46.55	1.97
3500	1.00	58.19	2.08	58.19	2.46
3500	1.20	69.82	2.50	69.82	2.96
3500	1.40	81.46	2.91	81.46	3.45

9.3 Results Wang PFI model

9.3.1 Reactor conditions

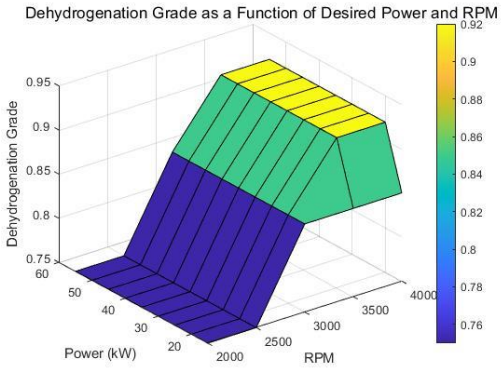

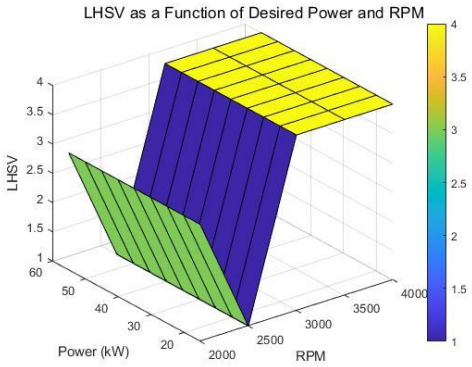

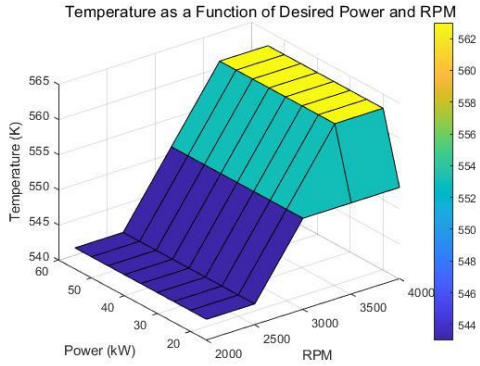

9.3.2 Hydrogen burner mass flows

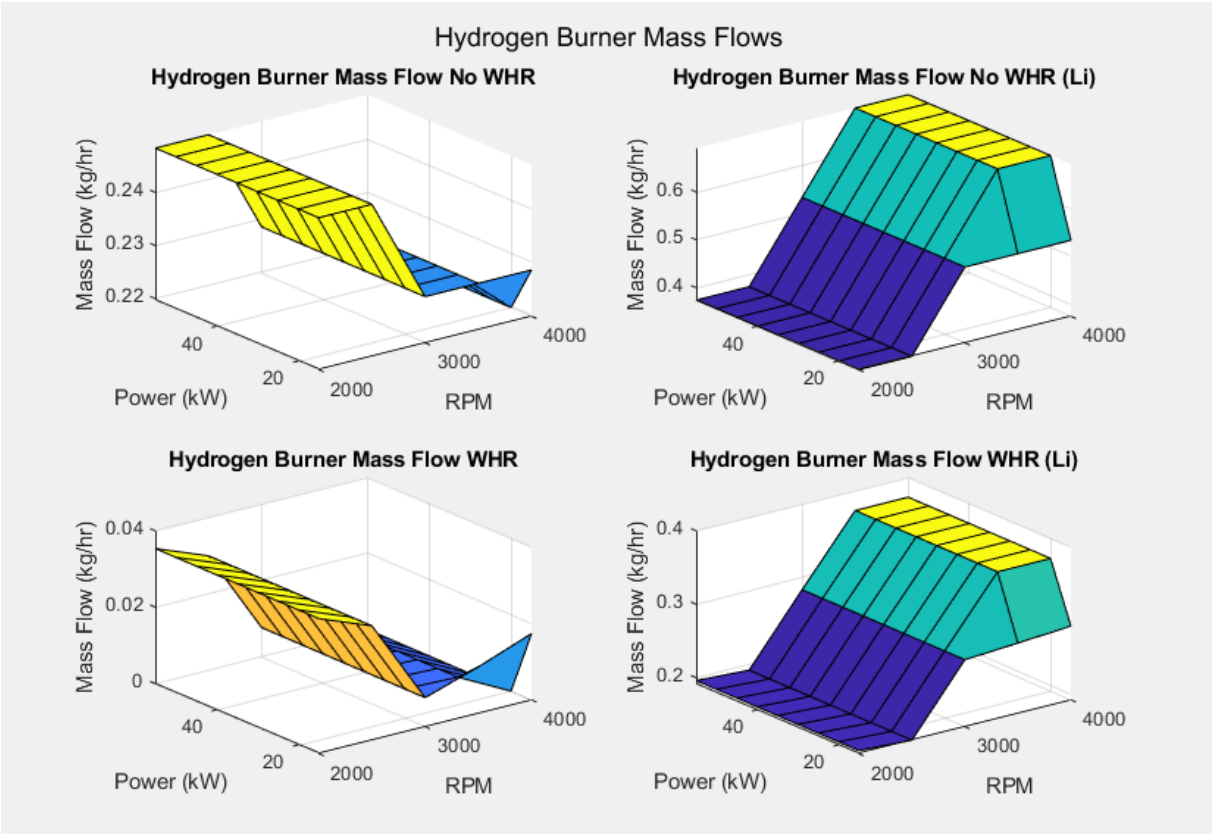

9.3.3 H2 and LOHC mass flows

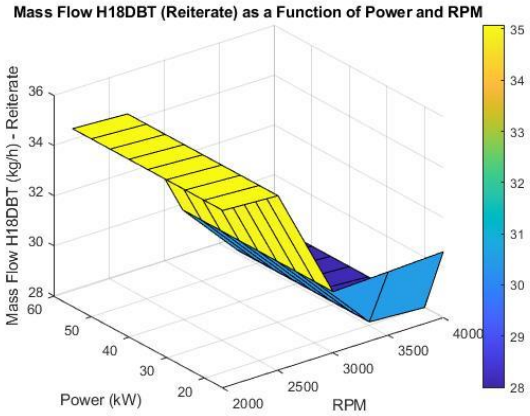

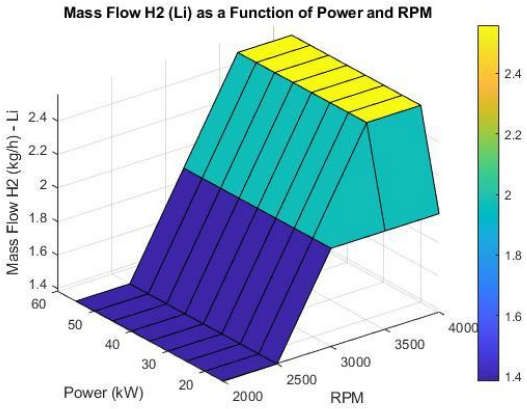

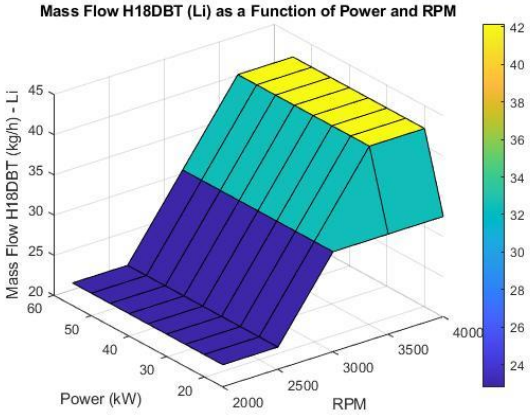

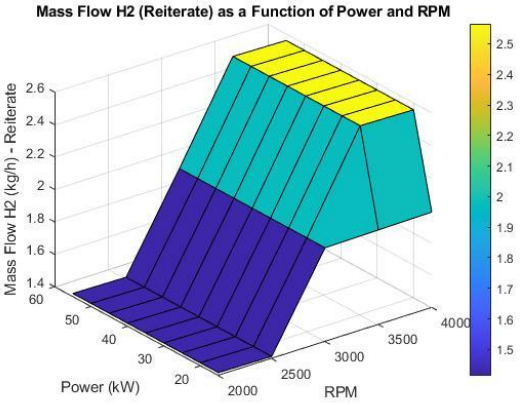

9.4 Validation script Preuster

The script meticulously incorporates key parameters such as the density of H18-DBT, molecular weights of H18-DBT and H2, porosity of the catalyst bed, fraction of active reactor volume, efficiency, density of the catalyst, rate constant, activation energy, gas constant, and both the higher and lower heating values of hydrogen. Additionally, it follows the detailed empirical relationships provided in the article to calculate the hydrogen molar flow rate and subsequently convert this to the hydrogen mass flow rate in standard liters per minute.

```
density_H18DBT = 900;    % Density LOVH in kg/m3
M_H18DBT = 290/1000;     % Molecular weight of H18DBT [kg/mol]
M_H2 = 2.016/1000;       % Molecular weight of H2 [kg/mol]
epsilon = 0.4;           % Porosity of catalyst bed
Frv = 0.8;               % Fraction of active reactor volume
eta_lohc = 0.95;         % Efficiency
rho_kat = 970;           % Density of catalyst [kg/m^3]
k0 = 125.24;             % Rate constant [1/s]
Ea = 119.8 * 10^3;       % Activation energy [J/mol]
R = 8.314;               % Gas constant [J/mol*K]
HHVH2_mol = 286000;      % Higher Heating Value of H2 [J/mol]
LHVH2_mol = 241920;      % Lower Heating Value of H2  [J/mol]
V_reactor = 6.825 *10^-3;% reactor volume in m3

% H2 mass flow of slpm = 7 at LOHC flow in ml/min at 300Ccatalyst temp
% VALIDATION from figure 9B
T = 570     % Temperature vector [K]
slpm = 7
LOHC_peters_ml_min = 30  %ml/min

LOHC_peters_m3_h = LOHC_peters_ml_min *(1/1000)*(1/1000) * (60)
%m3/hour
LOHC_peters_kg_s = LOHC_peters_ml_min *(1/1000)*(1/1000) * (1/60) * density_H18DBT
% kg/s
n_LOHC_peters_mol_s =  LOHC_peters_ml_min * (1*10^-6) * density_H18DBT *
(1/M_H18DBT)  %mol/s

LHSV_peters = LOHC_peters_m3_h / (V_reactor*epsilon*Frv)
tau = 3600/(LHSV_peters*500)

n_dot_h2_peters_mol_s =  9 *eta_lohc * n_LOHC_peters_mol_s * rho_kat * tau * k0 *
(exp(-Ea / (R * T))) * (3120 * eta_lohc)^1.98 %mol/s
m_dot_h2_peters_kg_h = n_dot_h2_peters_mol_s *M_H2 *3600
m_dot_h2_peters_slpm = m_dot_h2_peters_kg_h / 0.0053928

P_reactor = n_dot_h2_peters_mol_s * LHVH2_mol
P_reactor_kW = P_reactor/1000
```

9.5 Appendix A

	Reference	**Method**	**Heat sources**	**Results by** (Li et al., 2023)	**Relevant additions from examination underlying literature for this study**
1.	(Müller et al., 2019)	Thermo-dynamic modeling	SOFC, PEMFC, heat recycling	- High efficiency with SOFCs - Partial combustion attractive - Limited efficiency on electric heating	- Study aim was the evaluation of different configurations of this sequence. The results allowed for decisions on efficient process options. - Detailed overview and derivation of dissipation of energy for different heating options for dehydrogenation
2.	(Preuster et al., 2018)	Experiment	SOFC	- SOFC operational stability not affected by coupling - 45% chain efficiency	- Provided system design for optimal utilization of SOFC heat - Sufficient heat available for dehydrogenation - Dehydrogenation reactor control strategy proposed
3.	(Krieger C et al., 2016)	Thermo-dynamic modeling	PEMFC, heat recycling	- Hydrogen burner increased efficiency of the chain - Used thermals storage system to overcome temperature fluctuation in waste heat	- Storage buffer used heat form cement factory; undetermined if sufficient heat is available for ship applications
4.	(Lee et al., 2021)	Net energy analysis	SOFC, heat recycling		- Model developed with ASPEN plus software - Comparative analysis with other hydrogen carriers - Condenser after reactor mandatory
5.	(Haupt & Müller, 2017)	Thermo-dynamic modeling	PEMFC, natural gas burner	Most conclusions out of scope	- The first study to combine PEMFCs with natural gas burner for dehydrogenation - Showed use of PEMFC waste heat for LOHC dehydrogenation

9.6 Appendix B - reactors

Reference	Reactor Type	Heating	Temp/pressure/flow rate	Catalyst	Research method	System setup
(Geiling et al., 2021)	Vertically installed tube bundle reactor	Thermal oi and electrically heated circuit	330°C/typically below 5 bar	Pt/Al2O3	Experiment	Dynamic combined operation of LOHC dehydrogenation and PEMFCs
(Peters et al., 2019)	Catalyst bed reactor PFR modeled with cascade CSTR approach by Engelbrecht.	Air to reactor heat exchanger	260°C–310°C/1–5 bar	Pt/Al2O3	Model	Model-based approach analyzing transient operation behavior
(Lee et al., 2020)	Stirred batch reactor/pressure swing adsorption	Temperature controlled heating mantle	240°C–300°C/rapid pressure fluctuations in flow rate due to purging	Pt/Al2O3	Experiment	Determine feasibility of connected operation
(Preuster et al., 2018)	Catalyst bed reactor PFR	Temperature controlled	260°C–320°C/1–5 bar	Pt/Al2O3	Experiment	Experiment to test the operability of a SOFC stack with LOHC-saturated hydrogen
(N. Rao et al., 2022; P. C. Rao & Yoon, 2020)	Adiabatic packed bed reactor, isothermal packed bed, isothermal plug flow	Temperature controlled	250°C–340°C/1.2 bar/17 to 36 Nm^3/hr		Literature study of several models and DWSim-Python model	Model dehydrogenation reactor to perform cost optimization

10 Bibliography

A Onorati, R Payri, BM Vaglieco, AK Agarwal, C Bae, G Bruneaux, M Canakci, M Gavaises, M Günthner, C Hasse, S Kokjohn, S-C Kong, Y Moriyoshi, R Novella, A Pesyridis, R Reitz, T Ryan, R Wagner, and H Zhao (2022) - The role of hydrogen for future internal combustion engines. *International Journal of Engine Research 23:4, 529-540*

Asif, F., Hamayun, M. H., Hussain, M., Hussain, A., Maafa, I. M., & Park, Y. K. (2021). Performance analysis of the perhydro-dibenzyl-toluene dehydrogenation system—a simulation study. *Sustainability (Switzerland)*, *13*(11). https://doi.org/10.3390/su13116490

Bach, H., Bergek, A., Bjørgum, Ø., Hansen, T., Kenzhegaliyeva, A., & Steen, M. (2020). Implementing maritime battery-electric and hydrogen solutions: A technological innovation systems analysis. *Transportation Research Part D: Transport and Environment*, *87*. https://doi.org/10.1016/j.trd.2020.102492

Baldi, F., & Gabrielii, C. (2015). A feasibility analysis of waste heat recovery systems for marine applications. *Energy*, *80*, 654–665. https://doi.org/10.1016/j.energy.2014.12.020

Baldi, F., Johnson, H., Gabrielii, C., & Andersson, K. (2014). Energy analysis of ship energy systems - The case of a chemical tanker. *Energy Procedia*, *61*, 1732–1735. https://doi.org/10.1016/j.egypro.2014.12.200

Baroutaji, A., Arjunan, A., Ramadan, M., Robinson, J., Alaswad, A., Abdelkareem, M. A., & Olabi, A. G. (2021). Advancements and prospects of thermal management and waste heat recovery of PEMFC. *International Journal of Thermofluids*, *9*. https://doi.org/10.1016/j.ijft.2021.100064

Bollmann, J., Mitländer, K., Beck, D., Schühle, P., Bauer, F., Zigan, L., Wasserscheid, P., & Will, S. (2023). Burner-heated dehydrogenation of a liquid organic hydrogen carrier (LOHC) system. *International Journal of Hydrogen Energy*. https://doi.org/10.1016/j.ijhydene.2023.04.062

Boretti, A. (2020). Hydrogen internal combustion engines to 2030. *International Journal of Hydrogen Energy*, *45*(43), 23692–23703. https://doi.org/10.1016/j.ijhydene.2020.06.022

Carvalho, M. C. S. (2018). *Liquid Organic Hydrogen Carriers (LOHCs): A review and techno-economic analysis*.

Diaz, D. (2024). Development of an Eulerian multiphase CFD model for simulating a liquid organic hydrogen carrier dehydrogenation reactor. https://repository.tudelft.nl/

Fikrt, A., Brehmer, R., Milella, V. O., Müller, K., Bösmann, A., Preuster, P., Alt, N., Schlücker, E., Wasserscheid, P., & Arlt, W. (2017). Dynamic power supply by hydrogen bound to a liquid organic hydrogen carrier. *Applied Energy*, *194*, 1–8. https://doi.org/10.1016/J.APENERGY.2017.02.070

Gambini, M., Guarnaccia, F., Manno, M., & Vellini, M. (2024). Hydrogen flow rate control in a liquid organic hydrogen carrier batch reactor for hydrogen storage. *International Journal of Hydrogen Energy*, *51*, 329–339. https://doi.org/10.1016/j.ijhydene.2023.05.153

Geiling, J., Steinberger, M., Ortner, F., Seyfried, R., Nuß, A., Uhrig, F., Lange, C., Öchsner, R., Wasserscheid, P., März, M., & Preuster, P. (2021). Combined dynamic operation of PEM fuel cell and continuous dehydrogenation of perhydro-dibenzyltoluene. *International Journal of Hydrogen Energy*, *46*(72), 35662–35677. https://doi.org/10.1016/j.ijhydene.2021.08.034

Geißelbrecht, M., Benker, M., Seidel, A., Preuster. P., (2024) Modeling of the Continuous Dehydrogenation of Perhydro-Dibenzyltoluene in a Cuboid Reactor. *Energy Technol. 2024.* https://doi.org/10.1002/ente.202300813

Gurbuz, H. (2020). The Effect Of H2 Purity On The Combustion,Perfomance, Emissions, And Energy Costs In An Spark Ignition Engine. *Thermal Science*, *24*(1 Part A), 37–49. https://doi.org/10.2298/TSCI180705315G

Haupt, A., & Müller, K. (2017). Integration of a LOHC storage into a heat-controlled CHP system. *Energy*, *118*, 1123–1130. https://doi.org/10.1016/J.ENERGY.2016.10.129

He, T., Shi, R., Peng, J., Zhuge, W., & Zhang, Y. (2016). Waste heat recovery of a PEMFC system by using organic Rankine cycle. *Energies*, *9*(4). https://doi.org/10.3390/en9040267

Hoecke, L. Van, Laffineur, L., Campe, R., Perreault, P., Verbruggen, S. W., & Lenaerts, S. (2021). *Challenges in the use of hydrogen for maritime applications*. https://doi.org/10.1039/d0ee01545h

Hoesung Lee. (2023). *SYNTHESIS REPORT OF THE IPCC SIXTH ASSESSMENT REPORT*. https://www.ipcc.ch/report/ar6/syr/

IEA. (2022). *Global Hydrogen Review 2022*.

Jorschick, H., Geißelbrecht, M., Eßl, M., Preuster, P., Bösmann, A., & Wasserscheid, P. (2020). Benzyltoluene/dibenzyltoluene-based mixtures as suitable liquid organic hydrogen carrier systems for low temperature applications. *International Journal of Hydrogen Energy*, *45*(29), 14897–14906. https://doi.org/10.1016/j.ijhydene.2020.03.210

Jouhara H, Khordehgah N, Almahmoud S, Delpech B, Chauhan A, Tassou SA. Waste heat recovery technologies and applications. Therm Sci Eng Progr 2018: 268–89.

Kadar, J., Gackstatter, F., Ortner, F., Wagner, L., Willer, M., Preuster P., Wasserscheid, P., Geiselbrecht, M. (2024). Boosting power density of hydrogen release from LOHC systems by an inverted fixed-bed reactor design. *International Journal of Hydrogen Energy, Volume 59, 15 March 2024, Pages 1376-*1387. https://doi.org/10.1016/j.ijhydene.2024.02.096

Kandlikar, S. G., & Lu, Z. (2009). Thermal management issues in a PEMFC stack - A brief review of current status. *Applied Thermal Engineering*, *29*(7), 1276–1280. https://doi.org/10.1016/j.applthermaleng.2008.05.009

Korn, T., & Volpert, G. (2019). *The hybrid model of the new hydrogen combustion engine as the most efficient powertrain of tomorrow* (pp. 87–101). https://doi.org/10.1007/978-3-658-26056-9_6

Krieger C, Müller K, & Arlt W. (2016). Coupling of a liquid organic hydrogen carrier system with industrial heat. . *Chem Eng Technol*, *39*, 1570–1574.

Kwak, Y., Kirk, J., Moon, S., Ohm, T., Lee, Y. J., Jang, M., Park, L. H., Ahn, C. il, Jeong, H., Sohn, H., Nam, S. W., Yoon, C. W., Jo, Y. S., & Kim, Y. (2021). Hydrogen production from homocyclic liquid organic hydrogen carriers (LOHCs): Benchmarking studies and energy-economic analyses. *Energy Conversion and Management*, *239*. https://doi.org/10.1016/j.enconman.2021.114124

Lee, S., Han, G., Kim, T., Yoo, Y. S., Jeon, S. Y., & Bae, J. (2020). Connected evaluation of polymer electrolyte membrane fuel cell with dehydrogenation reactor of liquid organic hydrogen carrier. *International Journal of Hydrogen Energy*, *45*(24), 13398–13405. https://doi.org/10.1016/j.ijhydene.2020.02.129

Lee, S., Kim, T., Han, G., Kang, S., Yoo, Y. S., Jeon, S. Y., & Bae, J. (2021). Comparative energetic studies on liquid organic hydrogen carrier: A net energy analysis. *Renewable and Sustainable Energy Reviews*, *150*. https://doi.org/10.1016/j.rser.2021.111447

Li, L., Vellayani Aravind, P., Woudstra, T., & van den Broek, M. (2023). Assessing the waste heat recovery potential of liquid organic hydrogen carrier chains. *Energy Conversion and Management*, *276*. https://doi.org/10.1016/j.enconman.2022.116555

Li, M.; Wang, J., Chen, Z., Qian, X., Sun, C., Gan, D., Xiong, K., Rao, M., Chen, C., Li, X. A Comprehensive Review of Thermal Management in Solid Oxide FuelCells: Focus on Burners, Heat Exchangers, and Strategies. *Energies2024, 17, 1005. https://doi.org/10.3390/en17051005*

Luo, Q. he, & Sun, B. gang. (2018). Experiments on the effect of engine speed, load, equivalence ratio, spark timing and coolant temperature on the energy balance of a turbocharged hydrogen engine. *Energy Conversion and Management*, *162*, 1–12. https://doi.org/10.1016/j.enconman.2017.12.051

Mestemaker, B. T. W., Castro, M. B. G., Van Der Blom, E. C., Cornege, H. J., Ihc, R., & Visser, N. K. (2019). *ZERO EMISSION VESSELS FROM A SHIPBUILDERS PERSPECTIVE*.

Müller, K., Thiele, S., & Wasserscheid, P. (2019). Evaluations of Concepts for the Integration of Fuel Cells in Liquid Organic Hydrogen Carrier Systems. *Energy and Fuels*, *33*(10), 10324–10330. https://doi.org/10.1021/acs.energyfuels.9b01939

Niermann, M., Beckendorff, A., Kaltschmitt, M., & Bonhoff, K. (2019). Liquid Organic Hydrogen Carrier (LOHC) – Assessment based on chemical and economic properties. In *International Journal of Hydrogen Energy* (Vol. 44, Issue 13, pp. 6631–6654). Elsevier Ltd. https://doi.org/10.1016/j.ijhydene.2019.01.199

Niermann, M., Drünert, S., Kaltschmitt, M., & Bonhoff, K. (2019). Liquid organic hydrogen carriers (LOHCs)-techno-economic analysis of LOHCs in a defined process chain. *Energy and Environmental Science*, *12*(1), 290–307. https://doi.org/10.1039/c8ee02700e

Niermann, M., Timmerberg, S., Drünert, S., & Kaltschmitt, M. (2021). Liquid Organic Hydrogen Carriers and alternatives for international transport of renewable hydrogen. *Renewable and Sustainable Energy Reviews*, *13*5. https://doi.org/10.1016/j.rser.2020.110171

Nieminen, J., Dincer, I. (2009). Comparative exergy analyses of gasoline and hydrogen fuelled ICE. *International Journal of Hydrogen Energy. (Vol. 35, Issue 10, pp. 5124-5132) h*ttps://doi.org/10.1016/j.ijhydene.2009.09.003.

Obara, S. (2019). Energy and exergy flows of a hydrogen supply chain with truck transportation of ammonia or methyl cyclohexane. *Energy*, *174*, 848–860. https://doi.org/10.1016/J.ENERGY.2019.01.103

Onorati, A., Payri, R., Vaglieco, B. M., Agarwal, A. K., Bae, C., Bruneaux, G., Canakci, M., Gavaises, M., Günthner, M., Hasse, C., Kokjohn, S., Kong, S. C., Moriyoshi, Y., Novella, R., Pesyridis, A., Reitz, R., Ryan, T., Wagner, R., & Zhao, H. (2022). The role of hydrogen for future internal combustion engines. In *International Journal of Engine Research* (Vol. 23, Issue 4, pp. 529–540). SAGE Publications Ltd. https://doi.org/10.1177/14680874221081947

Peters, R., Deja, R., Fang, Q., Nguyen, V. N., Preuster, P., Blum, L., Wasserscheid, P., & Stolten, D. (2019). A solid oxide fuel cell operating on liquid organic hydrogen carrier-based hydrogen – A kinetic model of the hydrogen release unit and system performance. *International Journal of Hydrogen Energy*, *44*(26), 13794–13806. https://doi.org/10.1016/j.ijhydene.2019.03.220

Preuster, P., Fang, Q., Peters, R., Deja, R., Nguyen, V. N., Blum, L., Stolten, D., & Wasserscheid, P. (2018). Solid oxide fuel cell operating on liquid organic hydrogen carrier-based hydrogen – making full use of heat integration potentials. *International Journal of Hydrogen Energy*, *43*(3), 1758–1768. https://doi.org/10.1016/j.ijhydene.2017.11.054

Rao, N., Lele, A. K., & Patwardhan, A. W. (2022). Optimization of Liquid Organic Hydrogen Carrier (LOHC) dehydrogenation system. *International Journal of Hydrogen Energy*, *47*(66), 28530–28547. https://doi.org/10.1016/j.ijhydene.2022.06.197

Rao, P. C., & Yoon, M. (2020). Potential liquid-organic hydrogen carrier (Lohc) systems: A review on recent progress. *Energies*, *13*(22). https://doi.org/10.3390/en13226040

Rüde, T., Dürr, S., Preuster, P., Wolf, M., & Wasserscheid, P. (2022). Benzyltoluene/perhydro benzyltoluene - pushing the performance limits of pure hydrocarbon liquid organic hydrogen carrier (LOHC) systems†. *Sustainable Energy and Fuels*, *6*(6), 1541–1553. https://doi.org/10.1039/d1se01767e

Sapra, H., Stam, J., Reurings, J., van Biert, L., van Sluijs, W., de Vos, P., Visser, K., Vellayani, A. P., & Hopman, H. (2021). Integration of solid oxide fuel cell and internal combustion engine for maritime applications. *Applied Energy*, *281*. https://doi.org/10.1016/j.apenergy.2020.115854

Seidel, A. (2019). *Refuelling of fuel cell vehicles by hydrogen from the LOHC process-Gas for Energy*. https://12ft.io/proxy?q=https%3A%2F%2Fwww.readkong.com%2Fpage%2Frefuelling-of-fuel-cell-vehicles-by-hydrogen-from-the-lohc-89644471/16Science

Shakeri, N., Zadeh, M., & Bremnes Nielsen, J. (2020). Hydrogen Fuel Cells for Ship Electric Propulsion: Moving Toward Greener Ships. *IEEE Electrification Magazine*, *8*(2), 27–43. https://doi.org/10.1109/MELE.2020.2985484

Stępień Z. Analysis of the prospects for hydrogen-fuelled internal combustion engines. Combustion Engines. 2024;197(2):32-41. https://doi.org/10.19206/CE-174794

Van Rheenen, E. S., Padding, J. T., Slootweg, J. C., & Visser, K. (2022). *A review of the potential of hydrogen carriers for zero emission, low signature ship propulsion systems*.

Verhelst, S. (2014). Recent progress in the use of hydrogen as a fuel for internal combustion engines. In *International Journal of Hydrogen Energy* (Vol. 39, Issue 2, pp. 1071–1085). https://doi.org/10.1016/j.ijhydene.2013.10.102

Verhelst, S., Wallner T. (2009) Hydrogen-fueled internal combustion engines. Pro*gress in Energy and Combustion Science* (Vol. 35, Issue 6, pp 490-527). https://doi.org/10.1016/j.pecs.2009.08.001.

Wan, Z., el Makhloufi, A., Chen, Y., & Tang, J. (2018). Decarbonizing the international shipping industry: Solutions and policy recommendations. *Marine Pollution Bulletin*, *126*, 428–435. https://doi.org/10.1016/j.marpolbul.2017.11.064

Wang, X., Sun, B. gang, & Luo, Q. he. (2019). Energy and exergy analysis of a turbocharged hydrogen internal combustion engine. *International Journal of Hydrogen Energy*, 5551–5563. https://doi.org/10.1016/j.ijhydene.2018.10.047

Wang, Y., & Wright, L. A. (2021). A Comparative Review of Alternative Fuels for the Maritime Sector: Economic, Technology, and Policy Challenges for Clean Energy Implementation. *World*, *2*(4), 456–481. https://doi.org/10.3390/world2040029

Wu, Z., Zhang, Z., & Ni, M. (2018). Modeling of a novel SOFC-PEMFC hybrid system coupled with thermal swing adsorption for H2 purification: Parametric and exergy analyses. *Energy Conversion and Management*, *174*, 802–813. https://doi.org/10.1016/j.enconman.2018.08.073

Ye, M., Sharp, P., Brandon, N., & Kucernak, A. (2022). System-level comparison of ammonia, compressed and liquid hydrogen as fuels for polymer electrolyte fuel cell powered shipping. *International Journal of Hydrogen Energy*, *47*(13), 8565–8584. https://doi.org/10.1016/j.ijhydene.2021.12.164

Yew Heng Teoh, Heoy Geok How, Thanh Danh Le, Huu Tho Nguyen, Dong Lin Loo, Tazien Rashid, Farooq Sher. (2023). A review on production and implementation of hydrogen as a green fuel in internal combustion engines. Fuel, Volume 333, Part 2, ISSN 0016-361.https://doi.org/10.1016/j.fuel.2022.126525.

Zhang, S. W., Sun, B. G., Lin, S. L., Li, Q., Wu, X., Hu, T., Bao, L. Z., Wang, X., & Luo, Q. he. (2023). Energy and exergy analysis for a turbocharged direct-injection hydrogen engine to achieve efficient and high-economy performances. *International Journal of Hydrogen Energy*. https://doi.org/10.1016/j.ijhydene.2023.04.038

Zhao, F. cheng, Sun, B. gang, Yuan, S., Bao, L. zhi, Wei, H., & Luo, Q. he. (2024). Experimental and modeling investigations to improve the performance of the near-zero NOx emissions direct-injection hydrogen engine by injection optimization. *International Journal of Hydrogen Energy*, *49*, 713–724. https://doi.org/10.1016/j.ijhydene.2023.09.039

Zhu, Q. L., & Xu, Q. (2015). Liquid organic and inorganic chemical hydrides for high-capacity hydrogen storage. In *Energy and Environmental Science* (Vol. 8, Issue 2, pp. 478–512). Royal Society of Chemistry. https://doi.org/10.1039/c4ee03690e

11 MATLAB Script

In the below chapter the MATLAB script is divided into the relevant parts as discussed in this thesis.

```
%%%%%%%%%%%%%%%%%%%%%%%%%%%%%%%%%%%%%%%%%%%%%%%%%%%%%%%%%%%%%%%%%%%%%%%%%%%%%%%%%%%
```

11.1 Opening statements

```
clc
clear
close all

%% user notes

% ADD EFFICIENCIES!!!!!!
% dehydro grades toevoegen

%WHEN YOU GET THIS ERROR THERE ARE NO RESULTS THAT SATISFY THE DEHYDRGENATION
GRADE
% Result with the lowest heat requirement (absolute sum of heat fluxes) and valid
m_dot_H2_reactor_kgh_Peters:
% Index exceeds the number of array elements. Index must not exceed 0.
%
% Error in all_scripts_20240710_1530 (line 555)
% fprintf('Q_coolant: %.2f kW, Q1: %.2f kW, Q2: %.2f kW, Q3: %.2f kW, Q4: %.2f
kW\n', min_Q_values_kW_reiterated(1), min_Q_values_kW_reiterated(2),
min_Q_values_kW_reiterated(3), min_Q_values_kW_reiterated(4),
min_Q_values_kW_reiterated(5));


%% Loops
% for a = 1:length(rpm_values)
% for b = 1:length(Ts)
% p = loop desired power
% r= loop desired rpm
% for m = 1:length(rpm)
% for n = 1:length(bmep)
```

11.2 Defining reactor, H2ICE and modelling requirements

```
%% Inputs
desired_power_values =  [15, 20, 30, 40, 50, 60, 70, 80]; % power values in kW
desired_rpm_values = [1500, 2000, 2500, 3000, 3500]; % RPM values

% H2ICE constants Zhang
bmep = [0.4, 0.6, 0.8, 1.0, 1.2, 1.4]*10^6; % BMEP values in Pascals
rpm = [1500, 2000, 2500, 3000, 3500]; % RPM values

DFI_BTE_BMEP = [27.46, 31.65, 33.57, 34.39, 34.82]/100; % DFI Brake Thermal
Efficiency function of bmep
DFI_BTE_RPM =  [32.25, 33.52, 31.91, 32.49, 31.97]/100; % DFI Brake Thermal
Efficiency function of RPM

PFI_BTE_BMEP = [27.1, 27.4, 28.6, 28.1, 27.0]/100; % PFI Brake Thermal Efficiency
function of bmep
PFI_BTE_RPM =  [27.1, 27.4, 28.6, 28.1, 27.0]/100; % PFI Brake Thermal Efficiency
function of RPM
```

```
LHV_fuel = 120*10^6; % Lower Heating Value of fuel in Joules/kg
density_hydrogen = 0.0899; % [kg/m3]
H2_kWh =33.33;

bore = 0.088; % Bore in meters
stroke = 0.082; % Stroke in meters
cylinders = 4; % Number of cylinders
four_stroke = 2; % Four stroke engine factor (= 2 for four stroke , 1 for 2
stroke)
A_cylinder = pi * (bore/2)^2; % Area of a cylinder
Displacement = cylinders * A_cylinder * stroke; % in cubic meters
stochiometry = 23.6; %stociometric AFR

% heat fluxes reactor inputs
T_coolant = 80 + 273;
T_ambient = 25 + 273;      % Ambient temperature in Kelvin
T_reactor_in = 250 + 273;  % Temp to which H18DBT is heated before entering the
reactor
T_cooled = 40 + 273;       % Temperature to which spent DBT and Hydrogen are
cooled

Cp_H2 = 14304;  % Specific heat capacity of hydrogen [J/kg*K]
evaporation_enthalpy_hydrogen_J_Kg = 448413;    %    [J/kg H2]

% Scaling factor of Peters reactor
scaling_factor = 16;

% Heat exchanger efficiencies
HEX1 = 0.8; % heat excanger foir coolant H2ICE
HEX2 = 0.8;  % heat exchanger to from exhaust to dehydro generator
HEX3 = 0.8;  % heat exchanger hydrogen gas to incoming LOHC
HEX4 = 0.8;  % spent LOHC to incoming LOHC

% Define the tolerance for massflows (so how close do reactor outputs need to be
to H2ICE required) 0.2 = 20%
tolerance = 0.125; % 15% is the lowest tolerance that allows all functions to run

% min dehydrogentaion grade
required_dehydrogenation_grade = 0.7; % to run all operating point a min of 70%
dehydrogenation is highest possible
```

11.3 Loop over the operating points of the H2ICE

```
%% Data processing


% Initialize table to store the results
results_table = table();

for p = 1:length(desired_power_values)
    for r = 1:length(desired_rpm_values)



        %% Inputs
        desired_power_kW = desired_power_values(p);
        desired_rpm = desired_rpm_values(r);
```

```
        fprintf('Desired power value : %.2f kW\n', desired_power_values(p));
        fprintf('Desired RPM: %.2f RPM \n', desired_rpm_values(r));

        % Convert kW to Watts
        desired_power_W = desired_power_kW * 1000;
```

11.4 H2ICE calculation of mass flows

```
  %% H2ICE

        % Calculate power for each BMEP and RPM combination in Watts and convert
to kW
        power_DFI_kW = zeros(length(bmep), length(rpm));
        power_PFI_kW = zeros(length(bmep), length(rpm));
        for m = 1:length(rpm)
            for n = 1:length(bmep)
                power_DFI_kW(n,m) = bmep(n) * Displacement * (rpm(m)/60) /
four_stroke / 1000;
                power_PFI_kW(n,m) = bmep(n) * Displacement * (rpm(m)/60) /
four_stroke / 1000;
            end
        end

        % Indices for maximum RPM and BMEP
        idx_rpm_max = length(rpm);  % Index of the maximum RPM
        idx_bmep_max = length(bmep); % Index of the maximum BMEP

        % Calculate max power for DFI and PFI in Watts and convert to kW
        max_power_DFI_kW = bmep(idx_bmep_max) * Displacement *
(rpm(idx_rpm_max)/60) / four_stroke / 1000;
        max_power_PFI_kW = bmep(idx_bmep_max) * Displacement *
(rpm(idx_rpm_max)/60) / four_stroke / 1000;

        % Indices for minimum RPM and BMEP
        idx_rpm_min = 1;  % Index of the minimum RPM (assuming rpm array is sorted
in ascending order)
        idx_bmep_min = 1; % Index of the minimum BMEP (assuming bmep array is
sorted in ascending order)

        % Calculate min power for DFI and PFI in Watts and convert to kW
        min_power_DFI_kW = bmep(idx_bmep_min) * Displacement *
(rpm(idx_rpm_min)/60) / four_stroke  / 1000;
        min_power_PFI_kW = bmep(idx_bmep_min) * Displacement *
(rpm(idx_rpm_min)/60) / four_stroke  / 1000;

        % Calculate fuel flows
        % Preallocate arrays for fuel flows
        DFI_fuel_flow_H2 = zeros(length(bmep), length(rpm));
        PFI_fuel_flow_H2 = zeros(length(bmep), length(rpm));

        % Calculate fuel flows [kg/hr]
        for m = 1:length(rpm)
            for n = 1:length(bmep)
                DFI_fuel_flow_H2(n,m) = 3600 * density_hydrogen * 1/stochiometry
*(bmep(n) * Displacement * ((rpm(m)/60)/four_stroke) *  100) / (DFI_BTE_RPM(m) *
LHV_fuel);
```

```
                PFI_fuel_flow_H2(n,m) = 3600 * density_hydrogen * 1/stochiometry *
(bmep(n) * Displacement * ((rpm(m)/60)/four_stroke) * 100) / (PFI_BTE_RPM(m) *
LHV_fuel);
            end
        end

% Validate the input RPM
if ~ismember(desired_rpm, rpm)
    error('The entered RPM is not valid. Please enter one of the following RPM
values: %s', num2str(rpm));
end

% Initialize calculated_bmep as an array of zeros with the same length as rpm
calculated_bmep = zeros(1, length(rpm));

% Calculate BMEP for the desired RPM and find closest match
closest_bmep = inf;
closest_index = 0;

% Find the index for the desired RPM
desired_rpm_index = find(rpm == desired_rpm);

calculated_bmep(desired_rpm_index) = (desired_power_W * 2 * pi) / (Displacement *
desired_rpm/60);
[min_difference, idx] = min(abs(bmep - calculated_bmep(desired_rpm_index)));
if min_difference < closest_bmep
    closest_bmep = min_difference;
    closest_index = idx;
end

required_bmep_Pascals = bmep(closest_index);
required_bmep_MPascals = required_bmep_Pascals / (1*10^6);  % Get the BMEP at the
closest index
 fprintf('Required BMEP: %.2f MPa at %d RPM\n', required_bmep_MPascals,
desired_rpm);

% Calculate the fuel flow at the required BMEP and RPM
DFI_fuel_flow_at_required = DFI_fuel_flow_H2(closest_index, desired_rpm_index);
PFI_fuel_flow_at_required = PFI_fuel_flow_H2(closest_index, desired_rpm_index);

fprintf('Fuel Flow at %.2f MPa BMEP and %d RPM:\n', required_bmep_MPascals,
desired_rpm);
fprintf('DFI Fuel Flow: %.2f kg/hr\n', DFI_fuel_flow_at_required);
fprintf('PFI Fuel Flow: %.2f kg/hr\n', PFI_fuel_flow_at_required);

% Extract the fuel flows for the specified BMEP across all RPMs
DFI_flows_at_bmep = DFI_fuel_flow_H2(closest_index, :);
PFI_flows_at_bmep = PFI_fuel_flow_H2(closest_index, :);
```

11.5 Peters 2019, 1D heterogenous reactor model

```
%% Power filter
% Define the file path
filePath = 'LHSV_reaction_temperature_data.xlsx';

% Read the data from the first sheet of the Excel file
data = readmatrix(filePath);
```

```
H2_mass_fraction = 0.062;   % Hydrogen weight percentage in H18DBT
Ts = (513:10:613)';     % Temperature vector [K]
h = 1:1:10;             % Space velocity vector [h^-1]

% Load the Excel data
raw_data = xlsread('LHSV_reaction_temperature_data.xlsx');
temp_list_power = raw_data(1, 2:end); % Temperatures from the first row, excluding
the first cell
LHSV_list_power = raw_data(2:end, 1); % LHSVs from the first column, excluding the
first cell
grade_matrix_power = raw_data(2:end, 2:end); % power grade matrix

% Initialize results array
results = zeros(length(h) * length(Ts), 6);

% Loop through the temperature and space velocity vectors to populate the results
matrix
for i = 1:length(h)
    for j = 1:length(Ts)
        idx = (i-1) * length(Ts) + j;
        LHSV = h(i);
        T = Ts(j);

        % Find the indices for the current LHSV and temperature
        [~, LHSV_idx] = ismember(LHSV, LHSV_list_power);
        [~, T_idx] = ismember(T, temp_list_power);

        % Get the power grade from the matrix
        Power_grade = NaN;
        if LHSV_idx > 0 && T_idx > 0
            Power_grade = grade_matrix_power(LHSV_idx, T_idx);
        end

        % Calculate the volume flow of LOHC
        epsilon = 0.4;          % Porosity of catalyst bed
        Frv = 0.8;              % Fraction of active reactor volume
%         scaling_factor = 16;
        V_reactor = scaling_factor * 6.825 * 10^-3; % m^3 reactor volume
        V_dot_lohc_m3_h_Peters = LHSV  * V_reactor * epsilon * Frv; % Determines
the volume flow of LOHC m3/h
        V_dot_lohc_L = V_dot_lohc_m3_h_Peters * 1000; % Change volume flow of LOHC
in L /hour

        % Calculate the mass flow of H2
        density_H18DBT = 1000 * (1.1005251 + (-0.0006384 * 570));      % Density
of H18-DBT [kg/m³]
        massflow_H18DBT_kg_h_Peters = V_dot_lohc_m3_h_Peters * density_H18DBT;
        P_reactor = Power_grade * V_dot_lohc_L; % Gives  power for a given power
grade and volume flow
        m_dot_H2_reactor_Peters = P_reactor / H2_kWh; % 1kg of H2 gives 33.33 kWh
%assuming 100% dehydrogenation

        % Check if m_dot_H2_reactor_Peters is close to either PFI or DFI required
values
        if abs(m_dot_H2_reactor_Peters - DFI_fuel_flow_at_required) /
DFI_fuel_flow_at_required <= tolerance
            % Store the values in the results matrix
            results(idx, :) = [LHSV, T, V_dot_lohc_m3_h_Peters,
massflow_H18DBT_kg_h_Peters, m_dot_H2_reactor_Peters, Power_grade];
```

```
        end
    end
end

% Filter out rows with all zeros (i.e., those that did not meet the condition)
filtered_results = results(any(results, 2), :);

% Convert the filtered results to a table for better readability
power_results_table = array2table(filtered_results, 'VariableNames', {'LHSV',
'Temperature_K', 'V_dot_lohc_m3_per_h_Peters', 'massflow_H18DBT_kg_h_Peters',
'm_dot_H2_reactor_kgh_Peters', 'PowerGrade'});

% % Display the filtered results table
% disp('Filtered power results table:')
% disp(power_results_table)

%% Dehydrogantion grade selector

% Load the dehydrogenation grade data
raw_data_dehydro = xlsread('dehydrogenation_grade.xlsx');
temp_list_dehydro = raw_data_dehydro(1, 2:end); % Temperatures from the first row,
excluding the first cell
LHSV_list_dehydro = raw_data_dehydro(2:end, 1); % LHSVs from the first column,
excluding the first cell
grade_matrix_dehydro = raw_data_dehydro(2:end, 2:end); % Dehydrogenation grade
matrix

% Loop through the results to compute the dehydrogenation grade
dehydro_grades = NaN(size(power_results_table, 1), 1); % Initialize dehydro_grades
array
V_dot_lohc_reactor_dehydro_m3_h = NaN(size(power_results_table, 1), 1); %
Initialize V_dot_lohc_reactor_dehydro array

for i = 1:size(power_results_table, 1)
    LHSV = power_results_table.LHSV(i);
    T = power_results_table.Temperature_K(i);

    % Find the indices for the current LHSV and temperature
    [~, LHSV_idx] = ismember(LHSV, LHSV_list_dehydro);
    [~, T_idx] = ismember(T, temp_list_dehydro);

    % Get the dehydrogenation grade from the matrix
    dehydro_grade = NaN;
    if LHSV_idx > 0 && T_idx > 0
        dehydro_grade = grade_matrix_dehydro(LHSV_idx, T_idx);
    end

    % Store the dehydrogenation grade in the results table
    dehydro_grades(i) = dehydro_grade;

    % Calculate V_dot_lohc_reactor_dehydro based on the dehydrogenation grade
    if ~isnan(dehydro_grade) && dehydro_grade > 0
        V_dot_lohc_reactor_dehydro_m3_h(i) =
(power_results_table.V_dot_lohc_m3_per_h_Peters(i) / dehydro_grade); %TAKES
V_dot_LOHC FROM POWER FILTER in m3/h
    else
        V_dot_lohc_reactor_dehydro_m3_h(i) = NaN; % Assign NaN if dehydro_grade is
not valid
    end
```

```
end

% Add the dehydrogenation grade and V_dot_lohc_reactor_dehydro to the table
power_results_table.Dehydrogenation_Grade = dehydro_grades;
power_results_table.V_dot_lohc_reactor_dehydro_kgh =
V_dot_lohc_reactor_dehydro_m3_h * density_H18DBT;

% Filter the results to only include rows with dehydrogenation grade above the
threshold
filtered_dehydro_results =
power_results_table(power_results_table.Dehydrogenation_Grade >
required_dehydrogenation_grade, :);

% % Display the modified matrix
% disp('Modified Matrix:')
% disp(filtered_dehydro_results)


%% Calculate heat fluxes PETERS 2019

% Prepare the matrix to store Q values for acceptable grades
Q_values_kW = zeros(height(filtered_dehydro_results), 5); % For storing Q values
in kW
absolute_sums = zeros(height(filtered_dehydro_results), 1); % For storing the
absolute sums of heat fluxes

% Counter for acceptable grades
k = 1;

for i = 1:height(filtered_dehydro_results)
    Temperature = filtered_dehydro_results.Temperature_K(i); % Use the temperature
from the results as T3

    density_H18DBT = 1000 * (1.1005251 + (-0.0006384 * Temperature));      %
Density of H18-DBT [kg/m³]
    density_H0DBT = 1000 * (1.2537113 + (-0.0007150 * T_cooled));          %
Density of H0-DBT [kg/m³]

    % Extract necessary data from filtered_dehydro_results using correct column
names
    massflow_H18DBT_kg_s =
filtered_dehydro_results.V_dot_lohc_reactor_dehydro_kgh(i)  * 1/3600; % Convert
volumetric flow rate to mass flow rate in kg/s
    m_dot_H2_reactor_kg_s =
filtered_dehydro_results.m_dot_H2_reactor_kgh_Peters(i) / 3600; % Convert from
kg/h to kg/s

    check_H2_mass_fraction =  (m_dot_H2_reactor_kg_s/ massflow_H18DBT_kg_s) ;

    % Compute temperatures array
    Temperature_vector  = [T_coolant, T_ambient, T_reactor_in, Temperature,
T_cooled];

    % Compute Cp values using polynomial approximation for H18DBT and H0DBT
(Muller 2015)
    Cp_H18DBT = (1.9160 - 0.0075 .* Temperature_vector + 2.979e-5 .*
Temperature_vector.^2 - 2.905e-8 .* Temperature_vector.^3) * 1000; % in J/K*kg
    CP_H0DBT = (1.5069 - 0.0043 .* Temperature_vector+ 1.996e-5 .*
Temperature_vector.^2 - 1.680e-8 .* Temperature_vector.^3)  * 1000; % in J/K*kg
```

```
    % Mass flows
    molar_mass_hydrogen = 2.016 / 1000;           % Molar mass of hydrogen
[kg/mol]
    molar_mass_H18DBT = 290 / 1000;               % Molar mass of H18DBT [kg/mol]
Muller 2015
    molar_mass_H0DBT = molar_mass_H18DBT - molar_mass_hydrogen; % Molar mass of
H0DBT [kg/mol]

    M_H2 = 9 * molar_mass_hydrogen;  % in kg/mol
    M_H18DBT = molar_mass_H18DBT;    % in kg/mol
    M_H0DBT = M_H18DBT - M_H2;       % in kg/mol

    m2 = massflow_H18DBT_kg_s;
    m3 = m_dot_H2_reactor_kg_s; % already in kg/s
    m4 = m2 - m3; % kg/s

    % Compute Q values (as LHV is used nor evap and condesn component and Muller
2015 says not necessary)
    Q_coolant = m2 * Cp_H18DBT(1) * (T_coolant - T_ambient);
    Q1 = m2 * (Cp_H18DBT(2)+Cp_H18DBT(3))/2 * ( T_coolant - Temperature_vector(2)
) + (m2 * (Cp_H18DBT(3)+Cp_H18DBT(4))/2  * (Temperature - Temperature_vector(2)));
% Preheating oil to Temperature reactor
    Q2 = m3 * evaporation_enthalpy_hydrogen_J_Kg; % endothermic reaction energy
    Q3 = m3 * Cp_H2 * (T_cooled - Temperature); % cooling the Hydrogen gas
    Q4 = (m4 * (CP_H0DBT(5)+CP_H0DBT(4))/2 * (T_cooled - Temperature)); % WHR H0-
DBT, cooling down spent DBT

    % Store calculated Q values in kW
    Q_values_kW(k, :) = [Q_coolant, Q1, Q2, Q3, Q4]/1000  ;
    absolute_sums(k) = sum(abs([Q_coolant, Q1, Q2, Q3, Q4])); % Calculate and
store the absolute sum of heat fluxes
    k = k + 1;
end

% Find the result with the lowest absolute sum of heat fluxes
[~, min_index] = min(absolute_sums);
min_Q_values_kW = Q_values_kW(min_index, :);

% % % Display the result with the lowest heat requirement
%  fprintf('\nResult with the lowest heat requirement (absolute sum of heat
fluxes):\n');
%  fprintf('Q_coolant: %.2f kW, Q1: %.2f kW, Q2: %.2f kW, Q3: %.2f kW, Q4: %.2f
kW\n', min_Q_values_kW(1), min_Q_values_kW(2), min_Q_values_kW(3),
min_Q_values_kW(4), min_Q_values_kW(5));

% Adding Q values in kW to the filtered_dehydro_results table
filtered_dehydro_results.Q_coolant_kW = Q_values_kW(:, 1);
filtered_dehydro_results.Q1_kW = Q_values_kW(:, 2);
filtered_dehydro_results.Q2_kW = Q_values_kW(:, 3);
filtered_dehydro_results.Q3_kW = Q_values_kW(:, 4);
filtered_dehydro_results.Q4_kW = Q_values_kW(:, 5);

% % Display the updated table
 disp(filtered_dehydro_results);

% Display the row with the lowest absolute sum of heat fluxes
row_with_lowest_heat_fluxes = filtered_dehydro_results(min_index, :);
```

```
%  fprintf('\nRow with the lowest absolute sum of heat fluxes:\n');
%  disp(row_with_lowest_heat_fluxes);
```

11.6 Available exergy at operating point of H2ICE

```
%% Exergy available

% Define RPM values for labels
rpm_values = [1500, 2000, 2500, 3000, 3500];

% Define coolant mass flows (kg/h)
coolant_mass_flows = [500, 520, 540, 560, 580];

% Corresponding exhaust temperatures in Kelvin for RPMs
T_exhaust_zhang = [590, 600, 670, 700, 710];

% Reference temperature range in Kelvin
Ts = (513:10:613)';

% Define total exergy available at different RPMs [kW]
Exergy_available = {
    [14.5, 22.4, 30.4, 36.3, 42.5, 50.31],  % 1500 RPM
    [16, 30.4, 40.3, 48, 60, 70],           % 2000 RPM
    [26, 38, 52.3, 64, 78, 90],             % 2500 RPM
    [34, 48, 64, 84, 92, 108],              % 3000 RPM
    [42.5, 57.5, 76, 95, 95, 95]            % 3500 RPM
};

% Define Exergy percentages for exhaust and coolant at different RPMs and bmep
Exhaust_percentages = {
    [10.4, 10.5, 11.5, 12.6, 10.3, 11.0], % 1500 RPM
    [12.3, 12.4, 14.2, 15.6, 15.3, 16.6], % 2000 RPM
    [14.5, 14.5, 14.9, 15.6, 17, 17],     % 2500 RPM
    [19.1, 17.5, 18.3, 19.2, 18.2, 18.9], % 3000 RPM
    [23.4, 23.4, 18.2, 18.3, 18.7, 18.7]  % 3500 RPM
};

Coolant_percentages = {
    [3.13, 3.01, 3.1, 3.6, 2.7, 2.65],    % 1500 RPM
    [3.45, 2.61, 2.79, 2.61, 2.43, 2.59], % 2000 RPM
    [3.09, 2.7, 2.93, 2.95, 2.95, 2.95],  % 2500 RPM
    [3.15, 2.71, 2.58, 2.62, 1.94, 2.18], % 3000 RPM
    [3.47, 2.48, 2.37, 2.15, 2.15, 2.15]  % 3500 RPM
}; % Coolant percentages per RPM and BMEP

% Find the closest BMEP index
[~, required_index] = min(abs(bmep - required_bmep_Pascals));

% Initialize matrices to store the exergy and heat flux values
exergy_exhaust = zeros(length(rpm_values), length(Ts));
exergy_coolant = zeros(length(rpm_values), length(Ts));
heat_flux_exhaust_kW = zeros(length(rpm_values), length(Ts));

% Calculate exergy for exhaust and coolant at required BMEP across all RPMs and
temperatures
for a = 1:length(rpm_values)
    for b = 1:length(Ts)
```

```
        % Extract the specific exergy values for the required BMEP index
        exergy_exhaust(a, b) = Exergy_available{a}(required_index) *
(Exhaust_percentages{a}(required_index) / 100) * (cylinders / 4) * (Displacement /
0.002);
        exergy_coolant(a, b) = Exergy_available{a}(required_index) *
(Coolant_percentages{a}(required_index) / 100) * (cylinders / 4) * (Displacement /
0.002);

        % Calculate heat flux for exhaust
        heat_flux_exhaust_kW (a, b) = exergy_exhaust(a, b) * (T_exhaust_zhang(a) -
Ts(b)) / T_exhaust_zhang(a);
            if heat_flux_exhaust_kW(a,b)< 0
             heat_flux_exhaust_kW(a,b)  = 0;

         %Heat flux coolant
         heat_flux_coolant_kW(a) = exergy_coolant(a, b) * ((T_coolant -
T_ambient)/ T_coolant);
            if heat_flux_coolant_kW < 0
             heat_flux_coolant_kW   = 0;
         end
    end
end
end
```

11.7 Heat balances of WHR strategies

```
%% WHR strategies

%NO WHR
% Extract the row with the lowest heat fluxes
min_row = row_with_lowest_heat_fluxes;

% Determine Q_required
% fprintf('\n No WHR, determine added heat necessary :\n');
Q_required_kW_No_WHR = (min_row.Q_coolant_kW + min_row.Q1_kW + min_row.Q2_kW) /
HEX2;

% Calculate the amount of hydrogen in kg/hr needed to provide the heat for Q_WHR
hydrogen_burner_mass_flow_required_No_WHR_kg_s = ((Q_required_kW_No_WHR * 1000) /
LHV_fuel); % [kg/s]

% Convert to kg/hr
hydrogen_burner_mass_flow_kg_hr_No_WHR =
hydrogen_burner_mass_flow_required_No_WHR_kg_s * 3600; % [kg/hr]

% Display the amount of hydrogen needed or a message if not required
if hydrogen_burner_mass_flow_kg_hr_No_WHR < 0
    disp('No hydrogen burner required for 1D model');
    hydrogen_burner_mass_flow_kg_hr_No_WHR = 0; % Set to zero if no hydrogen
burner is required
else
    disp('Amount of hydrogen needed to be combusted with NO WHR for 1D model
(kg/hr):');
    disp(hydrogen_burner_mass_flow_kg_hr_No_WHR);
end
```

```
% WITH WHR

% Calculate sufficiency = Available/required NO WHR
fprintf('\nDetermine sufficiency of available exergy at operating point WITH WHR
for 1D model  :\n');

% Coolant
sufficiency_preheating_with_coolant_WHR = exergy_coolant(desired_rpm_index) /
min_row.Q_coolant_kW;
fprintf('Sufficiency of Preheating with Coolant to T Coolant with strategy 2 and 3
for 1D model  =  %.2f\n', sufficiency_preheating_with_coolant_WHR);

% Exhaust heat
sufficiency_exhaust_heat_WHR = heat_flux_exhaust_kW(desired_rpm_index) /
(min_row.Q1_kW + min_row.Q2_kW);
fprintf('Sufficiency of Preheating with exhaust to reactor temperature with
strategy 2 and 3 for 1D model  =  %.2f\n', sufficiency_exhaust_heat_WHR);

% Preheating to dehydrogenation temp "WHR strategy 1"
sufficiency_WHR1 = abs(min_row.Q1_kW / (min_row.Q4_kW + min_row.Q3_kW));
fprintf('Preheating to dehydrogenation temp  "WHR strategy 1 and 4 for 1D model =
%.2f\n', sufficiency_WHR1);

% Full integrated WHR
sufficiency_exhaust_heat_all_WHR =  abs((heat_flux_exhaust_kW(desired_rpm_index) +
(min_row.Q1_kW + min_row.Q2_kW + min_row.Q3_kW + min_row.Q4_kW)) / (min_row.Q1_kW
+ min_row.Q2_kW + min_row.Q3_kW + min_row.Q4_kW));
fprintf('Sufficiency of Exhaust Heat fully integrated  WHR utilizing WHR strategy
1 ,2,3 and 4 for 1D model= %.2f\n', sufficiency_exhaust_heat_all_WHR);

fprintf('\nWITH WHR, determine amount of hydrogen needed to be combusted for 1D
model :\n');

% determine required heat and include heat exchangers

% Calculate Q_required_kW_WHR
% coolant step
Q_required_1 = - exergy_coolant(desired_rpm_index) * HEX1 + min_row.Q_coolant_kW;

if Q_required_1 < 0
    Q_required_1 = 0;
end

% exhaust part
Q_required_2 =  - heat_flux_exhaust_kW(desired_rpm_index) * HEX2 + min_row.Q1_kW +
min_row.Q2_kW + min_row.Q3_kW* HEX3 + min_row.Q4_kW * HEX4 ;

Q_required_kW_WHR = Q_required_1 + Q_required_2;

% Set Q_required_kW_WHR to 0 if it is below zero
if Q_required_kW_WHR < 0
    Q_required_kW_WHR = 0;
end

% Calculate the amount of hydrogen in kg/hr needed to provide the heat for Q_WHR
hydrogen_burner_mass_flow_required_WHR_kg_s = (Q_required_kW_WHR * 1000) /
LHV_fuel; % [kg/s]

% Convert to kg/hr
```

```
hydrogen_burner_mass_flow_kg_hr_WHR = hydrogen_burner_mass_flow_required_WHR_kg_s
* 3600; % [kg/hr]

% Display the amount of hydrogen needed or a message if not required
if hydrogen_burner_mass_flow_kg_hr_WHR < 0
    disp('No hydrogen burner required for 1D model');
    hydrogen_burner_mass_flow_kg_hr_WHR = 0; % Set to zero if no hydrogen burner
is required
else
    disp('Amount of hydrogen needed to be burned with  WHR for 1D model
(kg/hr):');
    disp(hydrogen_burner_mass_flow_kg_hr_WHR);
end
```

11.8 Reiteration of mass flows and heat fluxes

```
%% Reiterate heat fluxes PETERS 2019 - adds
hydrogen_burner_mass_flow_required_WHR_kg_s and reiterates massflows and heat
fluxes

fprintf('\n reiteration adding H2 required for dehydrogenation  :\n');

% Heat fluxes
% Prepare the matrix to store Q values for acceptable grades
Q_values_kW_reiterated = zeros(height(filtered_dehydro_results), 5); % For storing
Q values in kW
absolute_sums_reiterated = zeros(height(filtered_dehydro_results), 1); % For
storing the absolute sums of heat fluxes

% Counter for acceptable grades
k = 1;

for i = 1:height(filtered_dehydro_results)
    Temperature = filtered_dehydro_results.Temperature_K(i); % Use the temperature
from the results as T3

    % Compute temperatures array
    Temperature_vector  = [T_coolant, T_ambient, T_reactor_in, Temperature,
T_cooled];

    % Compute Cp values using polynomial approximation for H18DBT and H0DBT
(Muller 2015)
    Cp_H18DBT = (1.9160 - 0.0075 .* Temperature_vector + 2.979e-5 .*
Temperature_vector.^2 - 2.905e-8 .* Temperature_vector.^3) * 1000; % in J/K*kg
    CP_H0DBT = (1.5069 - 0.0043 .* Temperature_vector + 1.996e-5 .*
Temperature_vector.^2 - 1.680e-8 .* Temperature_vector.^3) * 1000; % in J/K*kg

        % Set Q_required_kW_WHR to 0 if it is below zero
    if hydrogen_burner_mass_flow_required_WHR_kg_s < 0
        hydrogen_burner_mass_flow_required_WHR_kg_s = 0;
    end

    m2_reiterate = massflow_H18DBT_kg_s
+(hydrogen_burner_mass_flow_required_WHR_kg_s *1/H2_mass_fraction
*1/dehydro_grades(i));
    m3_reiterate = m_dot_H2_reactor_kg_s +
hydrogen_burner_mass_flow_required_WHR_kg_s; % already in kg/s
    m4_reiterate = m2_reiterate - m3_reiterate; % kg/s
```

```
    % Add m2_reiterate to column 3
    filtered_dehydro_results.massflow_H18DBT_kg_h_reiterate(i) = m2_reiterate
*3600;
    filtered_dehydro_results.m_dot_H2_reactor_kg_h_reiterate(i) = m3_reiterate
*3600;

    % Compute Q values [J/s = W]
    Q_coolant_reiterated = m2_reiterate * Cp_H18DBT(1) * (T_coolant - T_ambient);
    Q1_reiterated = m2_reiterate * (Cp_H18DBT(2)+Cp_H18DBT(3))/2 * ( T_coolant -
Temperature_vector(2) ) + (m2_reiterate * (Cp_H18DBT(3)+Cp_H18DBT(4))/2  *
(Temperature - Temperature_vector(2))); % Preheating oil to Temperature reactor
    Q2_reiterated = m3_reiterate * evaporation_enthalpy_hydrogen_J_Kg; %
endothermic reaction energy
    Q3_reiterated = m3_reiterate * Cp_H2 * (T_cooled - Temperature); % cooling the
Hydrogen gas
    Q4_reiterated = (m4_reiterate * (CP_H0DBT(5)+CP_H0DBT(4))/2 * (T_cooled -
Temperature)); % WHR H0-DBT, cooling down spent DBT

    % Store calculated Q values in kW
    Q_values_kW_reiterated(k, :) = [Q_coolant_reiterated, Q1_reiterated,
Q2_reiterated, Q3_reiterated, Q4_reiterated]/1000;
    absolute_sums_reiterated(k) = sum(abs([Q_coolant_reiterated, Q1_reiterated,
Q2_reiterated, Q3_reiterated, Q4_reiterated])); % Calculate and store the absolute
sum of heat fluxes
    k = k + 1;
end

% Find the result with the lowest absolute sum of heat fluxes and ensure
m_dot_H2_reactor_kgh_Peters is larger than DFI_fuel_flow_at_required
valid_row_found = false;
sorted_absolute_sums = sort(absolute_sums_reiterated);
min_index = 0;

for idx = 1:length(sorted_absolute_sums)
    [~, current_min_index] = ismember(sorted_absolute_sums(idx),
absolute_sums_reiterated);
    if filtered_dehydro_results.m_dot_H2_reactor_kgh_Peters(current_min_index) >
DFI_fuel_flow_at_required
        min_index = current_min_index;
        valid_row_found = true;
        break;
    end
end

if ~valid_row_found
    disp('No valid row found where m_dot_H2_reactor_kgh_Peters is larger than
DFI_fuel_flow_at_required. Continuing with the closest available result.');
    [~, min_index] = min(absolute_sums_reiterated);
end

min_Q_values_kW_reiterated = Q_values_kW_reiterated(min_index, :);

% Display the result with the lowest heat requirement
fprintf('\nResult with the lowest heat requirement (absolute sum of heat fluxes)
and valid m_dot_H2_reactor_kgh_Peters:\n');
fprintf('Q_coolant: %.2f kW, Q1: %.2f kW, Q2: %.2f kW, Q3: %.2f kW, Q4: %.2f
kW\n', min_Q_values_kW_reiterated(1), min_Q_values_kW_reiterated(2),
```

```
min_Q_values_kW_reiterated(3), min_Q_values_kW_reiterated(4),
min_Q_values_kW_reiterated(5));

% Display the updated table
filtered_dehydro_results.Q_coolant_kW_reiterated = Q_values_kW_reiterated(:, 1);
filtered_dehydro_results.Q1_kW_reiterated = Q_values_kW_reiterated(:, 2);
filtered_dehydro_results.Q2_kW_reiterated = Q_values_kW_reiterated(:, 3);
filtered_dehydro_results.Q3_kW_reiterated = Q_values_kW_reiterated(:, 4);
filtered_dehydro_results.Q4_kW_reiterated = Q_values_kW_reiterated(:, 5);

% Display the row with the lowest absolute sum of heat fluxes and valid
m_dot_H2_reactor_kgh_Peters
row_with_lowest_heat_fluxes = filtered_dehydro_results(min_index, :);
fprintf('\nRow with the lowest absolute sum of heat fluxes and valid
m_dot_H2_reactor_kgh_Peters:\n');
disp(row_with_lowest_heat_fluxes);
```

11.9 Li 2023, simplified thermodynamical reactor model

```
%% Li validations
fprintf('\n')
fprintf('\nLi 2023, determines heat fluxes and mass flow not wtih reactor model
but on simplified thermodynamical explanation:\n');
fprintf('\n')

% Initialize an empty table to store results
results_Li = table();

% Define the acceptable tolerance for "around"
tolerance = 0.2; % Example tolerance value, you can adjust as needed

for i = 1:height(filtered_dehydro_results)

    Cp_T0_Li = 449.5;  % J/mol*K
    Cp_Tde_Li = 678.6; % J/mol*K
    Tde_Li = filtered_dehydro_results.Temperature_K(i);
    T0_Li = T_ambient;
    m_dot_H2_reactor_kg_h_Li =
filtered_dehydro_results.m_dot_H2_reactor_kgh_Peters(i);
    m_dot_H2_reactor_kg_s_Li = m_dot_H2_reactor_kg_h_Li / 3600; % Convert from
kg/h to kg/s
    q_dehydrogenation_Li = 65400; % J/mol

    Q_dehydrogenation_Li_kW = (m_dot_H2_reactor_kg_s_Li / molar_mass_hydrogen) *
q_dehydrogenation_Li * 1/1000; % [kW]

    efficiency_dehydrogenation = 0.97;
    stochiometry_Li = 9;

    massflow_H18DBT_kg_s_Li = (m_dot_H2_reactor_kg_s_Li * molar_mass_H18DBT) /
(molar_mass_hydrogen * efficiency_dehydrogenation * stochiometry_Li);
    massflow_H0DBT_kg_s_Li = massflow_H18DBT_kg_s_Li - m_dot_H2_reactor_kg_s_Li;
    massflow_H18DBT_kg_h_Li = massflow_H18DBT_kg_s_Li * 3600;

    Q3_Li_kW = ((Cp_T0_Li + Cp_Tde_Li) / 2) * (massflow_H18DBT_kg_s_Li /
molar_mass_H18DBT) * (Tde_Li - T0_Li) * (1/1000);

    eff_HICE = 0.35;
```

```
    P_HICE_Li_kW = m_dot_H2_reactor_kg_h_Li * H2_kWh * eff_HICE;

    % Check if m_dot_H2_reactor_kg_h_Li is within the tolerance range of
DFI_fuel_flow_at_required and PFI_fuel_flow_at_required
    if abs(m_dot_H2_reactor_kg_h_Li - DFI_fuel_flow_at_required) <= tolerance ||
abs(m_dot_H2_reactor_kg_h_Li - PFI_fuel_flow_at_required) <= tolerance

        % Store results in the table if within the range
        results_Li = [results_Li; table(m_dot_H2_reactor_kg_h_Li,
Q_dehydrogenation_Li_kW, massflow_H18DBT_kg_h_Li, Q3_Li_kW, eff_HICE,
P_HICE_Li_kW)];
    end
end

% Display the table
disp(results_Li)

hydrogen_burner_mass_flow_required_WHR_kg_s_Li = ((Q_dehydrogenation_Li_kW-
Q3_Li_kW) - heat_flux_exhaust_kW(desired_rpm_index) -
exergy_coolant(desired_rpm_index))*1000 / LHV_fuel;
% Convert to kg/hr

hydrogen_burner_mass_flow_kg_hr_WHR_Li =
hydrogen_burner_mass_flow_required_WHR_kg_s_Li * 3600; % [kg/hr]

% Display the amount of hydrogen needed or a message if not required
if hydrogen_burner_mass_flow_kg_hr_WHR_Li < 0
    disp('With WHR, No hydrogen burner required for Li');
    hydrogen_burner_mass_flow_kg_hr_WHR_Li = 0; % Set to zero if no hydrogen
burner is required
else
    disp('Amount of hydrogen needed to be burned with WHR for Li (kg/hr):');
    disp(hydrogen_burner_mass_flow_kg_hr_WHR_Li);
end

hydrogen_burner_mass_flow_required_no_WHR_kg_s_Li =  Q_dehydrogenation_Li_kW*1000
/ LHV_fuel;
% Convert to kg/hr
hydrogen_burner_mass_flow_kg_hr_no_WHR_Li =
hydrogen_burner_mass_flow_required_no_WHR_kg_s_Li * 3600; % [kg/hr]

% Display the amount of hydrogen needed or a message if not required
if hydrogen_burner_mass_flow_kg_hr_no_WHR_Li < 0
    disp('No WHR No hydrogen burner required for Li');
    hydrogen_burner_mass_flow_kg_hr_no_WHR_Li = 0; % Set to zero if no hydrogen
burner is required
else
    disp('Amount of hydrogen needed to be burned without WHR for Li (kg/hr):');
    disp(hydrogen_burner_mass_flow_kg_hr_no_WHR_Li);
end



%% Efficiencies

%  Peters' Model Efficiency Calculation
efficiency_peters_no_whr  = desired_power_W / (m3 * LHV_fuel +
Q_required_kW_No_WHR*1000);
```

```
efficiency_peters_whr     = desired_power_W  / (m3_reiterate * LHV_fuel +
Q_required_kW_WHR*1000);

% % Li's Model Efficiency Calculation
efficiency_li_no_whr = desired_power_W / (m_dot_H2_reactor_kg_s_Li * LHV_fuel +
Q_dehydrogenation_Li_kW*1000  + Q3_Li_kW*1000 );
efficiency_li_whr    = desired_power_W / (m_dot_H2_reactor_kg_s_Li * LHV_fuel +
hydrogen_burner_mass_flow_kg_hr_WHR_Li );
```

11.10 End loop over H2ICE operating conditions and final results table

```
%% Store Results in Table
results_table = [results_table; table( ...
    desired_power_kW, desired_rpm, LHSV, Temperature , ...
    hydrogen_burner_mass_flow_kg_hr_No_WHR,
hydrogen_burner_mass_flow_kg_hr_no_WHR_Li, hydrogen_burner_mass_flow_kg_hr_WHR,
hydrogen_burner_mass_flow_kg_hr_WHR_Li, ...
    Q_required_kW_No_WHR, min_Q_values_kW_reiterated, ...
    efficiency_peters_no_whr, efficiency_peters_whr, efficiency_li_no_whr,
efficiency_li_whr )];


    end
end % end big loop
```

11.11 Post processing for figures and plots

```
%% Post processing (figures etc.)

% Save results_table to file
writetable(results_table, 'results_table.xlsx');
disp(results_table)

%Write results_table to workspace
assignin('base', 'results_table', results_table);

% Print the results to the command window
fprintf("\n'")

fprintf('Minimum Power for DFI: %.2f kW at %d RPM and %.2f MPa BMEP\n',
min_power_DFI_kW, rpm(idx_rpm_min), bmep(idx_bmep_min)/1e6);
fprintf('Maximum Power for DFI: %.2f kW at %d RPM and %.2f MPa BMEP\n',
max_power_DFI_kW, rpm(idx_rpm_max), bmep(idx_bmep_max)/1e6);

fprintf('Minimum Power for PFI: %.2f kW at %d RPM and %.2f MPa BMEP\n',
min_power_PFI_kW, rpm(idx_rpm_min), bmep(idx_bmep_min)/1e6);
fprintf('Maximum Power for PFI: %.2f kW at %d RPM and %.2f MPa BMEP\n',
max_power_PFI_kW, rpm(idx_rpm_max), bmep(idx_bmep_max)/1e6);

% Display the results in a tabular format
fprintf("\n")
fprintf('RPM\tBMEP (MPa)\tDFI P (kW)\tDFI H2(kg/hr)\tPFI P (kW)\tPFI
H2(kg/hr)\n');
fprintf('----\t----------\t----------\t----------\t----------\t----------\n');

for i = 1:length(rpm)
```

```
    for j = 1:length(bmep)
        fprintf('%d\t%.2f\t\t%.2f\t\t%.2f\t\t%.2f\t\t%.2f\n', rpm(i), bmep(j)/1e6,
power_DFI_kW(j,i), DFI_fuel_flow_H2(j,i), power_PFI_kW(j,i),
PFI_fuel_flow_H2(j,i));
    end
end

% Create a figure for plotting fuel flows
figure;

% Plot DFI fuel flow
subplot(1, 2, 1);
surf(rpm, bmep/10^6, DFI_fuel_flow_H2); % Plot BMEP in MPa
title('DFI Fuel Flow');
xlabel('Engine RPM');
ylabel('BMEP (MPa)');
zlabel('Fuel Flow (kg/hr)');
colorbar;
grid on;

% Plot PFI fuel flow
subplot(1, 2, 2);
surf(rpm, bmep/10^6, PFI_fuel_flow_H2); % Plot BMEP in MPa
title('PFI Fuel Flow');
xlabel('Engine RPM');
ylabel('BMEP (MPa)');
zlabel('Fuel Flow (kg/hr)');
colorbar;
grid on;

sgtitle('Fuel Flows as a Function of BMEP and RPM');

% Heat exchangers
fprintf("\n")
fprintf('HEX1 = %.1f\n', HEX1);
fprintf('HEX2 = %.1f\n', HEX2);
fprintf('HEX3 = %.1f\n', HEX3);
fprintf('HEX4 = %.1f\n', HEX4);
fprintf("\n")

% Initialize plot for exergy
figure;

% Plotting exergy from exhaust and exhaust temperature
subplot(2, 1, 1);
yyaxis left
bar(rpm_values, exergy_exhaust, 'b'); % Plot using RPM values as x-coordinates
ylabel('Exergy (kW)');
yyaxis right
plot(rpm_values, T_exhaust_zhang, 'r-o'); % Plot exhaust temperatures
ylabel('Exhaust Temperature (K)');
title('Exergy from Exhaust and Exhaust Temperature at Different RPMs');
xlabel('RPM');
grid on;

% Plotting exergy from coolant and coolant mass flow
subplot(2, 1, 2);
yyaxis left
bar(rpm_values, exergy_coolant, 'r'); % Plot using RPM values as x-coordinates
```

```
ylabel('Exergy (kW)');
yyaxis right
plot(rpm_values, coolant_mass_flows, 'g-o'); % Plot coolant mass flow
ylabel('Coolant Mass Flow (kg/h)', 'Color', 'g');  % Set the label color to green
title('Exergy and Mass Flow from Coolant at Required BMEP Across Different RPMs');
xlabel('RPM');
set(gca, 'YColor', 'g');  % Set the tick labels and axis color to green
grid on;
% Add note about coolant temperature
text(rpm_values(end), coolant_mass_flows(end), 'Coolant Temp = 353K',
'VerticalAlignment', 'top', 'Color', 'g');

hold off;

% Plot Hydrogen Burner Mass Flows as a Function of Desired Power and RPM
figure;

% Extract the relevant variables from the results table
desired_power = results_table.desired_power_kW;
desired_rpm = results_table.desired_rpm;
hydrogen_burner_mass_flow_No_WHR =
results_table.hydrogen_burner_mass_flow_kg_hr_No_WHR;
hydrogen_burner_mass_flow_no_WHR_Li =
results_table.hydrogen_burner_mass_flow_kg_hr_no_WHR_Li;
hydrogen_burner_mass_flow_WHR = results_table.hydrogen_burner_mass_flow_kg_hr_WHR;
hydrogen_burner_mass_flow_WHR_Li =
results_table.hydrogen_burner_mass_flow_kg_hr_WHR_Li;

% Create a unique list of desired powers and RPMs
unique_power = unique(desired_power);
unique_rpm = unique(desired_rpm);

% Initialize the hydrogen burner mass flows matrices
Z1 = NaN(length(unique_power), length(unique_rpm));
Z2 = NaN(length(unique_power), length(unique_rpm));
Z3 = NaN(length(unique_power), length(unique_rpm));
Z4 = NaN(length(unique_power), length(unique_rpm));

% Fill the matrices with the corresponding data
for idx = 1:height(results_table)
    power_idx = find(unique_power == desired_power(idx));
    rpm_idx = find(unique_rpm == desired_rpm(idx));
    Z1(power_idx, rpm_idx) = hydrogen_burner_mass_flow_No_WHR(idx);
    Z2(power_idx, rpm_idx) = hydrogen_burner_mass_flow_no_WHR_Li(idx);
    Z3(power_idx, rpm_idx) = hydrogen_burner_mass_flow_WHR(idx);
    Z4(power_idx, rpm_idx) = hydrogen_burner_mass_flow_WHR_Li(idx);
end

% Plot each hydrogen burner mass flow
subplot(2, 2, 1);
surf(unique_rpm, unique_power, Z1);
title('Hydrogen Burner Mass Flow No WHR');
xlabel('RPM');
ylabel('Power (kW)');
zlabel('Mass Flow (kg/hr)');

subplot(2, 2, 2);
surf(unique_rpm, unique_power, Z2);
title('Hydrogen Burner Mass Flow No WHR (Li)');
```

```
xlabel('RPM');
ylabel('Power (kW)');
zlabel('Mass Flow (kg/hr)');

subplot(2, 2, 3);
surf(unique_rpm, unique_power, Z3);
title('Hydrogen Burner Mass Flow WHR');
xlabel('RPM');
ylabel('Power (kW)');
zlabel('Mass Flow (kg/hr)');

subplot(2, 2, 4);
surf(unique_rpm, unique_power, Z4);
title('Hydrogen Burner Mass Flow WHR (Li)');
xlabel('RPM');
ylabel('Power (kW)');
zlabel('Mass Flow (kg/hr)');

sgtitle('Hydrogen Burner Mass Flows');

% Plot 2: Minimum Q Values Kw Reiterated as a Function of Desired Power and RPM
figure;

% Extract the relevant variables from the results table
min_Q_values_kW_reiterated = results_table.min_Q_values_kW_reiterated;

% Initialize the Q values matrix
Z = NaN(length(unique_power), length(unique_rpm));

% Fill the matrix with the corresponding data
for idx = 1:height(results_table)
    power_idx = find(unique_power == desired_power(idx));
    rpm_idx = find(unique_rpm == desired_rpm(idx));
    Z(power_idx, rpm_idx) = min_Q_values_kW_reiterated(idx);
end

% Plot the minimum Q values reiterated
surf(unique_rpm, unique_power, Z);
title('Minimum Q Values Kw Reiterated');
xlabel('RPM');
ylabel('Power (kW)');
zlabel('Q Values (kW)');
colorbar;
grid on;

sgtitle('Minimum Q Values Kw Reiterated as a Function of Desired Power and RPM');



% Plot 3: LHSV and Temperature as a Function of Desired Power and RPM
figure;

% Extract the relevant variables from the results table
LHSV = results_table.LHSV;
Temperature = results_table.Temperature;

% Create a unique list of desired powers and RPMs
unique_power = unique(desired_power);
unique_rpm = unique(desired_rpm);
```

```
% Initialize the LHSV and Temperature matrices
Z1 = NaN(length(unique_power), length(unique_rpm));
Z2 = NaN(length(unique_power), length(unique_rpm));

% Fill the matrices with the corresponding data
for idx = 1:height(results_table)
    power_idx = find(unique_power == desired_power(idx));
    rpm_idx = find(unique_rpm == desired_rpm(idx));
    Z1(power_idx, rpm_idx) = LHSV(idx);
    Z2(power_idx, rpm_idx) = Temperature(idx);
end

% Plot LHSV
subplot(1, 2, 1);
surf(unique_rpm, unique_power, Z1);
title('LHSV');
xlabel('RPM');
ylabel('Power (kW)');
zlabel('LHSV');
colorbar;
grid on;

% Plot Temperature
subplot(1, 2, 2);
surf(unique_rpm, unique_power, Z2);
title('Temperature');
xlabel('RPM');
ylabel('Power (kW)');
zlabel('Temperature (K)');
colorbar;
grid on;

sgtitle('LHSV and Temperature as a Function of Desired Power and RPM');
```